UNIVERSITY OF CALIFORNIA
RIVERSIDE

Spin Transport Study in Ferromagnetic and Antiferromagnetic Insulator Based Heterostructures

A Dissertation submitted in partial satisfaction
of the requirements for the degree of

Doctor of Philosophy

in

Physics

by

Yawen Liu

December 2019

Dissertation Committee:

Dr. Jing Shi, Chairperson
Dr. Peng Wei
Dr. Yongtao Cui

The Dissertation of Yawen Liu is approved:

Committee Chairperson

University of California, Riverside

Acknowledgments

Finishing writing this dissertation, the past five years is like a movie flashing before my eyes. All these happy, sad, exciting, frustrating, glorious and regretful moments consolidate, bringing me to this point of time and making me who I am today. Pursuing Ph.D is never an easy journey. Five years of time witnessed a young bachelor who just graduated from university becoming a responsible researcher, getting trained with professional knowledge and skills. It has also been a luxury period of time being able to focus on what I like to do with sufficient resources while without much pressure and noise from the outside world. Thank everybody and everything that give me this precious opportunity. At this moment, with my best sincerity, I wish I have been able to return something meaningful.

First and foremost, I want to give my deepest acknowledgment to my supervisor Prof. Jing Shi. Thank you for your encouragement, guidance and gracious support throughout the five years in my Ph.D study. Thank you for your valuable advices and mentorship. And thank you for all your positive influence on my attitude towards research and understanding on professional career as yourself being a passionate, insightful, determined and serious scientist. You have been teaching me how to be a responsible researcher in the most powerful voice with your dedication and devotion to physics.

I want to deeply thank my committee members Prof. Peng Wei and Prof. Yongtao Cui, for their insightful comments and suggestions on my research projects. I would like to express my appreciation to Prof. Vivek Aji and Prof. Jianlin Liu for being my oral exam committee members. I also want to thank Prof. Ran Cheng for the helpful discussions with him on spin transport in antiferromagnetic materials. I would like to express my

acknowledgment to Prof. Krassimir Bozhilov and Matthew Dickson for their help with the TEM imaging. I also want to thank the NanoFab Cleanroom Staffs Dong Yan, Mark Heiden and Frank Lee for their help with my experiments, and to thank Glenda Barraza and Derek Beving for their help with all the purchases, reimbursements and documents.

I would like to acknowledge my colleagues in the lab for their assistance, discussion and collaboration on research projects, and to thank my friends here for making life such fun in the past five years at UCR. They are Zilong Jiang, Chi Tang, Junxue Li, Zhisheng Lin, Yadong Xu, Weimin Zhou, Supeng Ge, Yanmeng Shi, Bowen Yang, Hua Wei, Mohammed Aldosary, Victor Ortiz, Siyu Li, Jin Zhang, Rui Lv, Kuan Zhou, Nan Zhang, Shi Che, Wei Yuan, Mark Lohmann, Benjamin Madon, Johnathan Turner, Haoshan Zhu, Jiawei Yang, Chenkun Wang, Yuanqian Liu, Yulu Liu, Tao Ren, Long Wang, Weinan Si, Paul Lou, Howard Chiang, Mohammed Alghamdi, Weilei Zeng, Xian Wang, Yinan Dong, Yi Zhang, Yuan Chen, Yunxiao Li, Yawei Qin and Zhenchen Hong.

I also want to thank my collaborators from different universities who made a lot of contributions to my academic work and had inspired with their brilliant ideas. They are Qiming Shao, Peng Zhang, Pan Lei and Prof. Kang L. Wang from UCLA, Zhe Wang and Prof. Ruqian Wu from UC Irvine, Prof. Cuizu Chang from Penn State.

Last but not least, I want to express my sincere thanks to my parents and grandparents. It is your love, support and everything that make me here.

To my parents and grandparents for their deepest love.

ABSTRACT OF THE DISSERTATION

Spin Transport Study in Ferromagnetic and Antiferromagnetic Insulator Based Heterostructures

by

Yawen Liu

Doctor of Philosophy, Graduate Program in Physics
University of California, Riverside, December 2019
Dr. Jing Shi, Chairperson

Spintronics has been an active research area for decades, as pure spin current which is free of Joule heating offers a promising possibility to build next-generation electronic devices with revolutionarily high energy efficiency. Spin-related transport phenomena such as anomalous Hall effect (AHE), spin Seebeck effect (SSE) and spin Hall magnetoresistance (SMR), serving as reliable probes, help researchers understand the generation, propagation and conversion of spin current as well as the mechanisms behind in ferromagnetic-material-based and antiferromagnetic-material-based spintronic systems. In Chapter 1, I will go through a brief introduction to those spin-related transport phenomena especially in ferromagnetic insulators (FMI) and antiferromagnetic insulators (AFMI) related systems.

FMI-based heterostructures with normal metals (NM) that have strong spin-orbit coupling, such as yttrium iron garnet YIG/Pt bilayers, have attracted a great deal of attention. In such systems, electric signal can only be generated in the metal layers adjacent to the FMI layer, which allows for more valid investigations into the pure spin current related phenomena. To better study various spin-related transport phenomena in FMI/NM bilay-

ers, good control over the magnetic anisotropy of FMI is essential. In Chapter 2, I will go through the techniques we use to engineer and manipulate magnetic anisotropy in FMI by choosing proper substrates that provide desired strain, tuning thickness of FMI and varying temperature. These tuning capabilities enable us to discover topological Hall effect (THE) in TmIG/Pt bilayers at room temperature and conduct systematically study to explore its physical origin.

In FMI/NM bilayers where NM has strong spin-orbit coupling, there have been some debates on whether those spin-related transport phenomena originate from the magnetic proximity effect (MPE) that NMs get magnetized by adjacent FMI layer or come from pure spin current contribution via spin Hall and inverse spin Hall effects in the NM layer. In Chapter 3, I will discuss my work on temperature dependence study of AHE in TmIG/Pt and TmIG/Cu/Pt heterostructures. The distinct behaviors in AHE temperature dependence w/o Cu spacer indicate that MPE dominates the AHE signal.

In recent years, great efforts have been devoted to the study of spintronics in antiferromagnetic insulator(AFMI) related heterostructures thanks to its unique properties of ultrafast spin dynamics and robustness against external field. AFMI working either as sources generating terahertz spin current or as a spacer in between FMI and NM that manipulates magnon propagation offer numerous interesting questions to be fully explored. Cr_2O_3 which is an uniaxial AFMI, has been a popular candidate for these study purposes. In Chapter 4, I will review the progress of recent AFMI related spin transport study. Then discuss in details of my research on the study of YIG/Cr_2O_3/Pt heterostructures, which begins from the growth and characterization of Cr_2O_3 thin films on FMI YIG and then the

observed unique behaviors in SSE measurements. The results are to be associated with the characteristic properties of Cr_2O_3 which reveal the existence of AFM magnon contribution in SSE.

Contents

List of Figures **xii**

List of Tables **xiv**

1 Introduction to Spintronics in Ferromagnetic Insulator and Antiferromagnetic Insulator Related Heterostructures **1**
1.1 Overview of Spintronics 1
1.2 Magnetic Proximity Effect in Heterostructures 4
1.3 Anomalous Hall Effect 6
1.4 Spin Hall Effects 8
1.5 Spin Seebeck Effect 10

2 Manipulation of Magnetic Anisotropy in Rare Earth Iron Garnet Thin Films and Observation of Topological Hall Effect in TmIG/Pt **13**
2.1 Brief Introduction to Rare Earth Iron Garnet 14
2.2 Engineering of Magnetic Anisotropy in ReIG 17
2.2.1 Pulsed Laser Deposition 17
2.2.2 Magnetic Anisotropy 18
2.2.3 Control of Magnetic Anisotropy in REIGs via Interfacial Strain and Magnetoelastic Effect 20
2.2.4 Characterization of Magnetic Anisotropy in REIG Thin Films 21
2.2.5 High-quality TmIG Thin Films with Perpendicular Magnetic Anisotropy 24
2.3 Observation of THE in TmIG/Pt via Controlling over Magnetic Anisotropy 25
2.3.1 Magnetic Skyrmions in Magnetic Insulators 25
2.3.2 Observation of the Topological Hall Effect 27
2.3.3 Field and Temperature Dependence 30
2.3.4 Thickness Dependence of Magnetic Insulator TmIG 32

3 Study of Anomalous Hall Effect and Spin Seebeck Effect in Ferromagnetic Insulator Based Heterostrucutures **37**
3.1 Overview of Anomalous Hall Effect in in Ferromagnetic Insulator Based Heterostrucutures 37

3.2 Temperature Dependence of Anomalous Hall Effect in TmIG/Pt heterostructures . . . 39
3.2.1 Observation of Low-field and High-field Anomalous Hall Effect in TmIG/Pt and their Sign Changes . . . 39
3.2.2 Anomalous Hall Effect in TmIG/Cu/Pt and Absence of High-field Feature and Sign Change . . . 44
3.2.3 Temperature Dependence of Anomalous Hall Effect in TmIG/Pt and TmIG/Cu/Pt with Different Layer Thicknesses . . . 46
3.2.4 First-principles Calculation of Anomalous Hall Effect Temperature Dependence in TmIG/Pt . . . 48
3.2.5 Magnetic Compensation in TmIG Measured by Anomalous Hall Effect 50

4 Study of Spin Transport in Ferromagnetic/Antiferromagnetic Insulator Based Heterostructures 53

4.1 Introduction to Spin Transport in Antiferromagnetic Insulator Related Heterostructures . . . 53
4.1.1 Overview of Antiferromagnetic Materials in Spintroncis . . . 53
4.1.2 Magnetic Resonance in Uniaxial Antiferromagnetic Materials . . . 55
4.1.3 Spin Seebeck Effect in Antiferromagnetic Insulators . . . 60
4.1.4 Overview of Spin Transport in Ferromagnetic/Antiferromagnetic Insulator Based Heterostrucures . . . 60
4.2 Growth of Cr_2O_3 Thin Films on YIG(110) . . . 64
4.2.1 Crystal and Magnetic Structure of Cr_2O_3 . . . 64
4.2.2 Lattice Matching between Cr_2O_3 and YIG . . . 65
4.2.3 Growth of Monolayer Single Crystalline Cr_2O_3 and Polycrystalline Cr_2O_3 on YIG (110) . . . 66
4.3 Spin Seebeck Effect in YIG/Cr_2O_3/Pt . . . 75
4.3.1 Spin Seebeck Device and Measurement . . . 75
4.3.2 Spin Seebeck in Monolayer Single Crystalline Cr_2O_3 . . . 79
4.3.3 Spin Seebeck in Thick Polycrystalline Cr_2O_3 . . . 84

5 Summary 88

Bibliography 90

List of Figures

1.1 Schematic diagram and TEM image of TI-based heterostructures 6
1.2 Illustration of three main mechanisms of AHE 7
1.3 Illustration of AHE, SHE and ISHE 9
1.4 Illustration of Seebeck effect and spin Seebeck effect 11
1.5 Transverse and longitudinal spin Seebeck measurement schematic diagrams 12

2.1 Crystal structure of rare earth iron garnets 14
2.2 Temperature dependence of saturation magnetic moment of various rare earth iron garnets 16
2.3 Schematic Illustration and real picture of pulsed laser deposition system . . 18
2.4 RHEED Oscillations of YIG growth and RHEED pattern of as-grown YIG Film 19
2.5 Schematic illustrations of the coordinate system used in the analysis of FMR and H_R vs. θ_H for with different $4\pi M_{eff}$ and g 24
2.6 Characterization data of TmIG film grown on NGG(111) substrate 26
2.7 Illustration of the THE and transport properties in TmIG/Pt 29
2.8 Observation of THE 35
2.9 Magnetic insulator thickness dependence of the THE 36

3.1 Illustration of AHE sign change and temperature dependence in TmIG/Pt (3nm) 40
3.2 Fitting of σ_{xy} vs. B at 5 K and 300 K of AHE in TmIG/Pt(2 nm) based on the two-band model 43
3.3 AHE in control samples 45
3.4 Temperature dependence of AHE in TmIG/Cu(t_{Cu})/Pt(2 nm) 46
3.5 Temperature dependence of low-field and high-field AHE in TmIG/Pt with different Pt thickness 47
3.6 DFT calculation results of AHE conductivity of Pt on TmIG 49
3.7 Temperature dependence of AHE conductivity of Pt calculated from DFT with different magnitudes of magnetic moment 50
3.8 Magnetic compensation in TmIG measured by AHE 52

4.1 Illustration of the two eigenmodes in AFMR 56
4.2 Illustration of canted spin moment and spin flop in AFM 58
4.3 Illustration of FMR mode in FMs and QFMR mode in AFMs 59
4.4 Frequency versus external magnetic field relations of the AFMR signals in MnF_2 59
4.5 Temperature dependence of V_{SSE} in FeF_2/Pt heterostructuref V_{SSE} 61
4.6 SSE measurement and result in YIG(111)/Cr_2O_3/Pt heterostructure 63
4.7 Crystal structure and spin structure of Cr_2O_3 64
4.8 Illustration of lattice planes of YIG and Cr_2O_3 66
4.9 Characterization of YIG grown on GGG (110) 67
4.10 Summary of identified key factors that influence Cr_2O_3 growth on YIG (110) 68
4.11 RHEED pattern and AFM image of as-grown Cr_2O_3 films from different growth temperature 70
4.12 Influence of post annealing on Cr_2O_3 captured by RHEED and AFM 71
4.13 TEM and EDS image of monolayer Cr_2O_3 grown on YIG (110) 73
4.14 RHEED, AFM, TEM and EDS image of thick polycrystalline Cr_2O_3 grown on YIG (110) 75
4.15 EDS and TEM images of Cr_2O_3 with mixed thickness 76
4.16 Pictures of SSE devices 77
4.17 Temperature difference calibration in SSE measurement 79
4.18 SSE signal in standard YIG/Pt device 80
4.19 Illustration of sign reversal and shut off of SSE in monolayer single crystalline YIG(110)/Cr_2O_3/Pt 82
4.20 Temperature dependence of SSE in monolayer single crystalline YIG(110)/Cr_2O_3/Pt with magnetic field from two perpendicular orientations 83
4.21 Illustration of observed SSE sign reversal in YIG(110)/Cr_2O_3/Pt heterostructure 84
4.22 Temperature dependence of SSE and illustration of observed exchange bias in thick YIG(110)/Cr_2O_3/Pt 85
4.23 Temperature dependence of SSE in YIG(110)/Cr_2O_3/Pt samples with mixed-Cr_2O_3-thickness regions 87

List of Tables

2.1 Perpendicular anisotropy field of an epitaxial magnetic film for different film plane 21
2.2 Magnetostriction constant of TmIG, TbIG and YIG 21

3.1 Fitting results of high-field AHE in TmIG/Pt(2 nm) with two-band model . 43

Chapter 1

Introduction to Spintronics in Ferromagnetic Insulator and Antiferromagnetic Insulator Related Heterostructures

1.1 Overview of Spintronics

Spin of electrons, another degree of freedom in addition to the degree of charge freedom, is an important research topic in modern physics. Spintronics is thus a multi-disciplinary field whose focus is on the manipulation of such spin degrees of freedom in various solid-state systems[143]. Typical or central problems being studied in spintronics field are: (a) effective generation of spin current which is to create nonequilibrium spin

states and manipulation of equilibrium spin states. (b) Characteristic propagation behaviors of spin current under different circumstances, spin dynamics in various material systems and interaction of neighboring static spin states. (c) Effective detection and probe of those equilibrium or nonequilibrium spin states.

Traditionally people use optical methods to inject spins which angular momenta of polarized photons are transferred to electrons. In the past two decades, theoretical predictions and experimental demonstrations of spin Hall effect (SHE), spin Seebeck effect (SSE), and spin pumping offered alternative ways of generating pure spin current more efficiently and conveniently. For the purpose of device applications, electrical spin injection as well as electrical detection are more desirable. In certain solid-state systems, strong correlation between electrons' charge freedom and spin freedom has enabled the observation of their interaction and significant manipulation of one via the other. These effects include but are not limited to anisotropic magnetoresistance (AMR), giant magnetoresistance (GMR) and tunnel magnetoresistance (TMR) which have triggered the blossom of enormous research and application projects. Exploring into these mechanisms not only help people build a more comprehensive understanding and gain knowledge on related fundamental physics, but also make huge contribution to the development of modern digital technology that has revolutionized the way of information storage and communication.

Motivated by technological applications, in spintronics studies, people have been focusing on metallic ferromagnetic systems in the past few decades. Researchers and engineers are able to create low-resistance and high-resistance states by altering relative orientations of magnetic moments in metallic devices which are used to represent 0 and 1 in

binary digital world. Significant efforts were committed on searching for novel material systems and device structures to push up the ceiling performance. Meanwhile in the last decade, rapid progress has been witnessed in the study of spin-transfer torque (STT) and spin-orbit torque (SOT). Electrical switching of spin states in nanoscale magnets via STT and SOT were demonstrated. More comprehensive research into those effects and better understanding of their physical origin, as well as more and more mature technologies, have enabled memory writing with lower power consumption thus allowed fabricating memory arrays with higher density.

Recently, ferro- or ferri- magnetic insulators (FMI) represented by yttrium iron garnet (YIG) and thulium iron garnet (TmIG) have attracted a great deal of attention. Compared to those magnetic metal based systems frequently used in previous studies, FMI based heterostructures allow for systematic research of pure spin current generation, magnetic polarization as well as spin-dependent scattering and reflection free of current shunting in the ferromagnetic metal layer. Most often studied structures are FMI/normal metal (NM) bilayers in which the NMs have large spin-orbit coupling. In such systems, all the spin-related electrical signals have to come from the adjacent NM layer via magnetic proximity effect (MPE), inverse spin Hall effect (ISHE) or spin-dependent scattering, which give people more clear insight into the fundamental physical origin of those spin transport phenomena.

Regardless of metallic or insulating magnetic material based systems, spin-related transport phenomena always serve as powerful probes of the spin states. Systematic and comprehensive studies on those effects are also the foundation to utilize them for any appli-

cation purpose. In the rest of this chapter, I will go through some spin-related effects that my Ph.D. research has focused on.

1.2 Magnetic Proximity Effect in Heterostructures

In multilayer heterostructures, adjacent layers may affect each other and acquire unique properties from their neighbors even in the absence of any physical interdiffusion of atoms. This mechanism is called proximity effect which origins from the overlap of electrons' wave functions at the interface. Proximity effect imparts the desired property into the target layer by building heterestructures with certain stacking. Meanwhile, any doping, which is commonly used but may potentially degrade the sample quality, is excluded. With these advantages and the developing material growth technologies, utilizing proximity effect for a variety of purposes has been actively explored throughout time. For example, people have attempted to increase the SOC strength in graphene so that some extraordinary quantum phenomena such as quantum spin Hall effect [39] and quantum anomalous Hall effect (QAHE)[92, 58, 96, 130] can occur. When graphene is placed on target substrates featuring heavy atoms, it has been demonstrated that the SOC strength in graphene can be well manipulated [128, 135, 134, 133].

One of the most commonly used way of proximity effect is to introduce magnetism into non-magnetic materials, which is called magnetic proximity effect (MPE). This approach is widely adopted in recent years especially for those non-magnetic heavy metal thin films with strong spin-orbit coupling (SOC) and two-dimensional topological materials represented by graphene and topological insulator (TI). With the combination of strong

SOC, the interfacial part of heavy metal layer like Pt, Ta and W in such heterostructures will behave effectively as ferromagnetic metal with the signature of pronounced anomalous Hall effect (AHE)[121, 142, 1, 109]. For graphene-based systems, Qiao et al. predicted that ferromagnetic graphene with Rashba SOC can exhibit QAHE. And this approach was demonstrated by Wang et al. in 2015 by observing large but not quantized AHE signal in graphene/YIG bilayer [128]. Regarding TI-based material systems, QAHE in TI was predicted by Shou-Cheng Zhang et al. in 2010 [139] and experimentally observed by Cui-Zu Chang et al. in 2013 [9]. Such QAHE state exists when the time reversal symmetry in TI is broken by the combination of ferromagnetism and intrinsic large SOC of TI which opens a nontrivial topological band gap in the TI surface states, and when the chemical potential is tuned to be located within the band gap. The remarkable features of QAHE state are the quantized anomalous Hall conductance($\pm e^2/h$), dissipationless chiral edge current transport in the absence of any external magnetic field and an ideally vanishing longitudinal resistance. Till nowadays, realization of QAHE has been in magnetic TI by means of doping magnetic metals such as Cr, V and Mn [10, 25]. For application purpose, it is crucial to lift the QAHE state temperature limit which much higher Curie temperature (T_c) of the ferromagnet is essential. However, lifting T_c via increasing doping level will inevitably lower sample quality with presence of disorder. To address this conflict of interest, introducing ferromagnetism via MPE has been actively explored [120, 129, 73, 40]. A great deal of attention has been drawn to this approach as it not only offers the possibility of realizing QAHE in non-magnetic TI but also can potentially increase the QAHE state temperature limit dramatically by choosing proper high T_c ferromagnetic layer, which promises considerable

application opportunity.

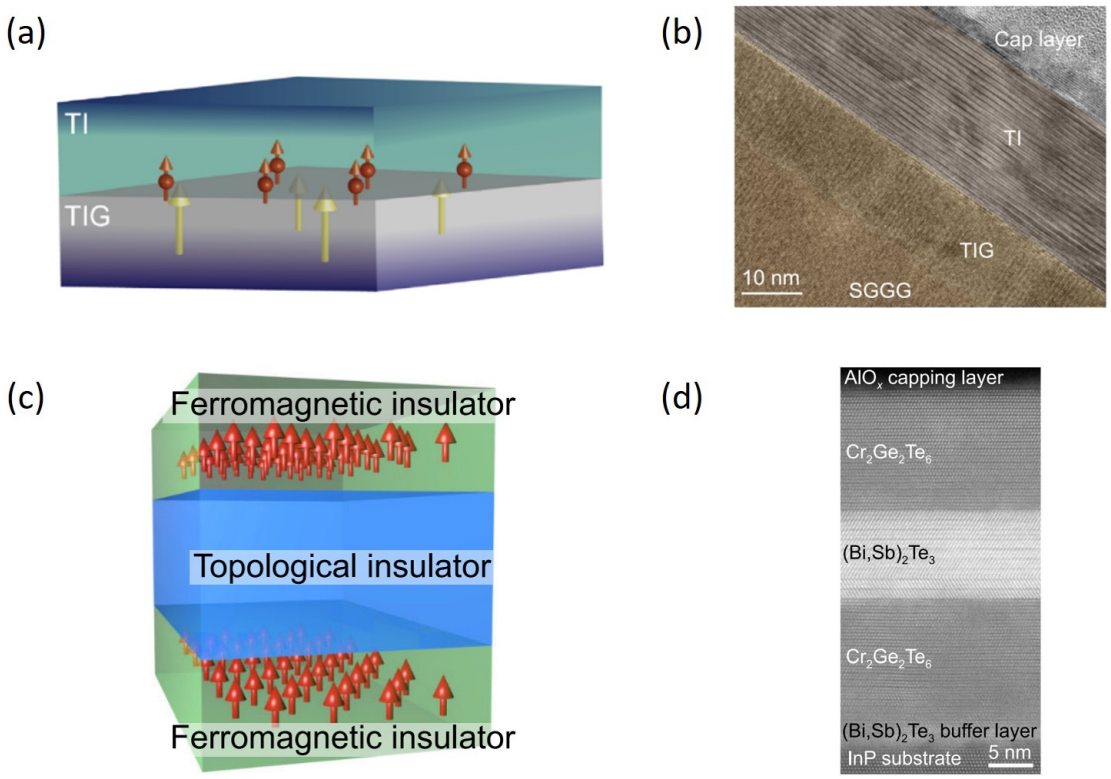

Figure 1.1: (a) and (b) Schematic diagram and transmission electron microscopy(TEM) image of FMI/TI bilayer heterostructure [120]. (c) and (d) Schematic diagram and transmission electron microscopy(TEM) image of FMI/TI/FMI sandwich structure [73]

.

1.3 Anomalous Hall Effect

Typically in ferromagnets, a Hall voltage response that is not directly linked to the external magnetic field but related to the magnetization orientation of the device is called anomalous Hall effect (AHE). It can be described using the simple expression:

$$\rho_{xy} = R_0 H_z + R_s M_z \tag{1.1}$$

where the first term represents the ordinary Hall effect proportional to the external magnetic field over a broad field range and the second term corresponds to Hall contribution due to the spontaneous magnetization.

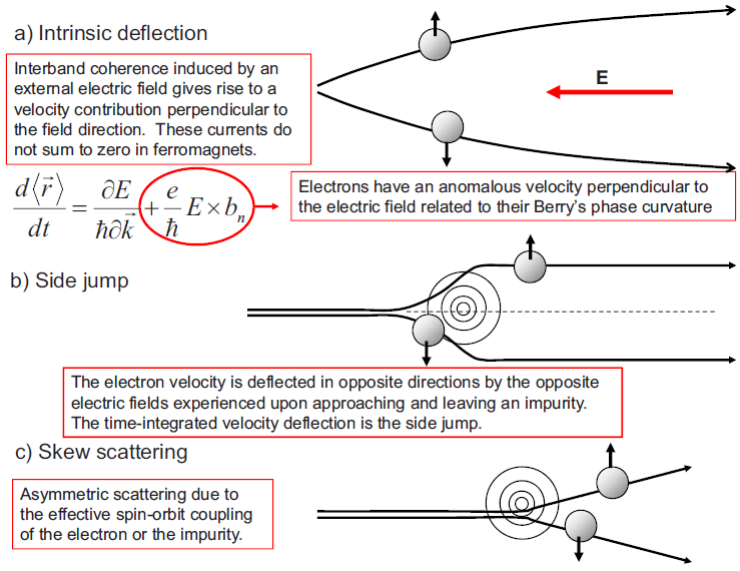

Figure 1.2: Illustration of three main mechanisms of AHE [76].

The three main mechanisms of AHE illustrated in FIG. 3. are:

- Intrinsic deflection: An intrinsic mechanism. Electrons gain an anomalous velocity originated from Berry phase and Berry curvature that are solely related to the band structure of perfect crystal.

- Skew scattering: An extrinsic mechanism. This contribution origins from the chiral features in the disorder scattering of spin-orbit coupled ferromagnets. It also has a

sharp definition that it iss a contribution proportional to the Bloch state transport lifetime, thus it tends to dominate in nearly perfect crystals.[76]

- Side jump: An extrinsic mechanism. It is defined as the rest part of anomalous Hall contribution besides the intrinsic and skew scattering ones. Electrons get deflected towards opposite direction as they approach and leave an impurity.

1.4 Spin Hall Effects

Spin Hall effects (SHE) are a collection of relativistic spin-orbit coupling phenomena in which electrical currents can generate transverse spin currents and vice versa. In the direct SHE, a transverse pure spin current with polarization direction perpendicular to the plane defined by the charge and spin current is generated when an electrical current flows through the material. And inverse SHE (ISHE) refers to its reciprocal effect where a pure spin current passing through the material will generate a transverse charge current.[111] The generalization of this effect was first proposed by Dyakonov and Perel over four decades ago [17] and finalized by similar prediction in more recent years [24, 141]. The physical concept of SHE borrows directly from anomalous Hall effect(AHE) where an asymmetric deflection of the charge carriers is generated due to relativistic spin-orbit coupling depending on their spin direction. An illustration of AHE, SHE and ISHE is shown in Figure 1.2.

The first observation of SHE was conducted via measuring Kerr rotation in GaAs and InGaAs semiconductor thin films [41]. Shortly after that, observation of voltage generated by ISHE was reported independently by Valenzuela et al. [126] and Saitoh et al.

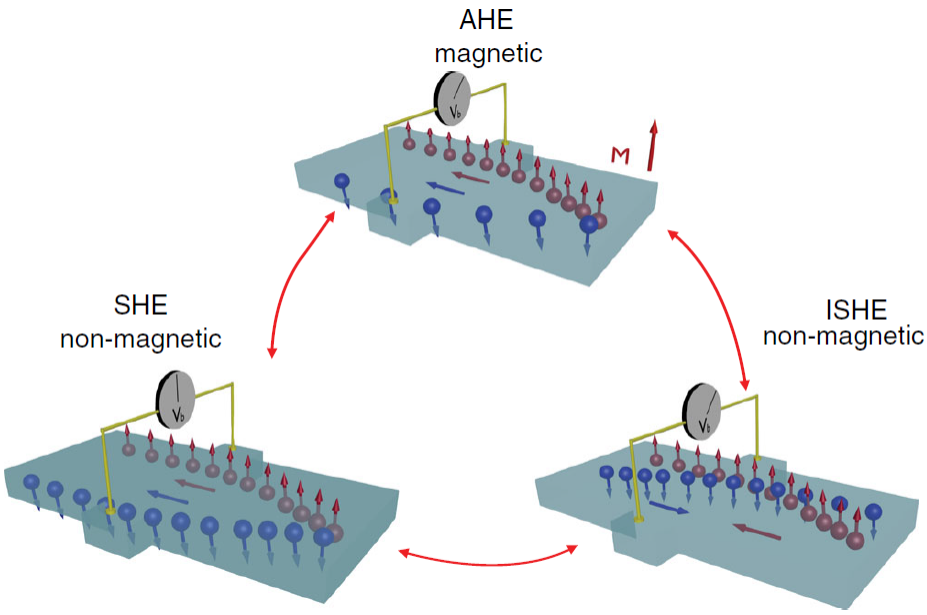

Figure 1.3: An illustration of the connected family of the spin-dependent Hall effects. In the AHE, a charge current generates a polarized transverse charge current. In the SHE, an unpolarized charge current generates a transverse pure spin current. In the ISHE, a pure spin current generates a transverse charge current [24]. Adopted from [111].

[102], which the former group used ferromagnet for the spin current injection and detection, and the latter group applied spin pumping method to populate spin current and detected it using normal metal Pt. The first successful demonstration of simultaneous detection of SHE and ISHE on the same device was achieved by Brüne et al. in 2010 [8]. Later it was found that spin currrent generated by SHE is large enough to significantly manipulate the magnetization state in the FM, including inducing magnetization dynamics, driving domain walls and switching static magnetization orientation [70, 69, 60, 18, 101, 59].

It is worth to note that FMIs represented by YIG and TmIG have been widely used in spin Hall effect studies and have offered people unique insights into relative physical mechanisms. Spin Hall magnetoresistance (SMR) was reported in YIG/Pt bilayers in 2013 where a difference in longitudinal resistance could be observed as a direct result

of ISHE when the magnetization orientation of YIG is parallel and perpendicular to the nonequilibrium spin polarization direction generated by SHE [79]. Nonlocal measurements in both lateral and vertical geometry were performed in YIG/Pt [15] and NM/YIG/NM heterostructures [52] which demonstrated the long spin-diffusion length of YIG and the concept of magnon-mediated current drag phenomenon respectively. Current switching of FMI via SHE induced spin-orbit torque (SOT) was also demonstrated in TmIG/Pt [1] and TmIG/W [110] heterostructures .

1.5 Spin Seebeck Effect

Spin Seebeck effect (SSE) is a spin analog of the Seebeck effect. In the conventional Seebeck effect, an electric field or a charge current is generated in conductors due to the electron-hole asymmetry at the Fermi energy when there is a heat current $\mathbf{Q}$ [3]. Spin Seebeck then refers to the generation of spin voltage upon applying temperature gradient on a ferromagnet.

SSE was first observed by K. Uchida et al. in NiFe/Pt bilayers in 2008 [122]. Then it was found in semiconductor GaMnAs [32] and in magnetic insulator $LaY_2Fe_5O_{12}$ [123] in 2010. The transverse geometry as shown in Fig. 1-5(a) was commonly used in these early experiments. A thermal gradient along the stripe drives different amount of spin-up and spin-down flow due their unequal Seebeck coefficients. As a result, a spin accumulation with opposite spin polarization is created at the two sides of the FM. The spin accumulation then gives rise to a spin current flowing from the FM to the NM that has strong spin-orbit coupling, which converts into a charge current or electrical voltage via

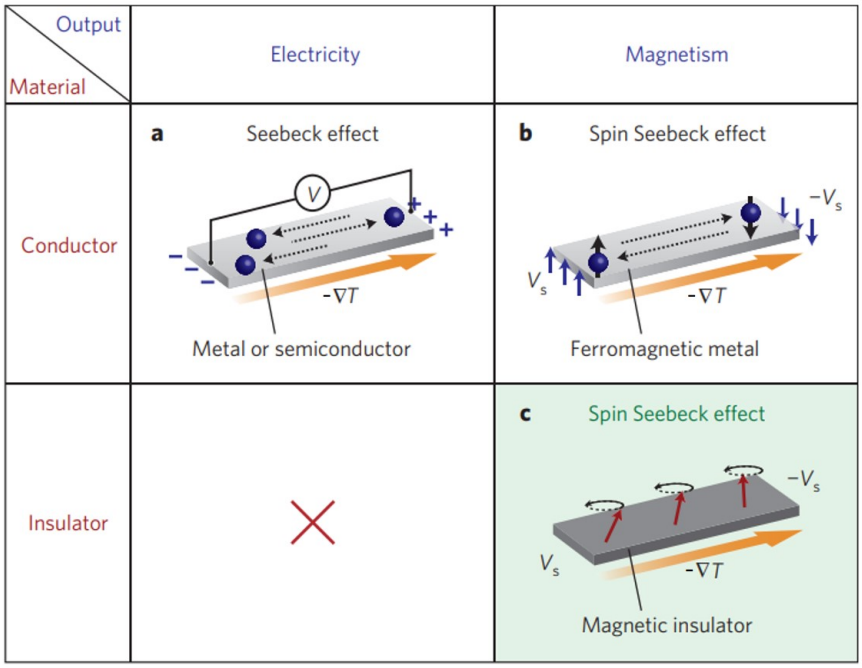

Figure 1.4: An illustration of Seebeck effect in conductors and spin Seebeck effect in both conductors and insulators [123].

ISHE with opposite signs at the two ends. However, there were some doubts and debates on these early experiments due to the possible contamination by the anomalous Nernst effect in the presence of unavoidable temperature gradient perpendicular to the FM/NM interface [29] and magnetic proximity effect [28], also because of the unreasonable long spin propagation length in the FM. But later the demonstration of longitudinal SSE (LSSE) in YIG/Au [94, 43] as shown in Fig 1-5(b) has unambiguously proved the generation of pure spin current free from anomalous Nernst effect by applying thermal gradient. Moreover, the LSSE then becomes a commonly used method to efficiently generate pure spin current that has been widely adopted for a variety of spintronics studies.

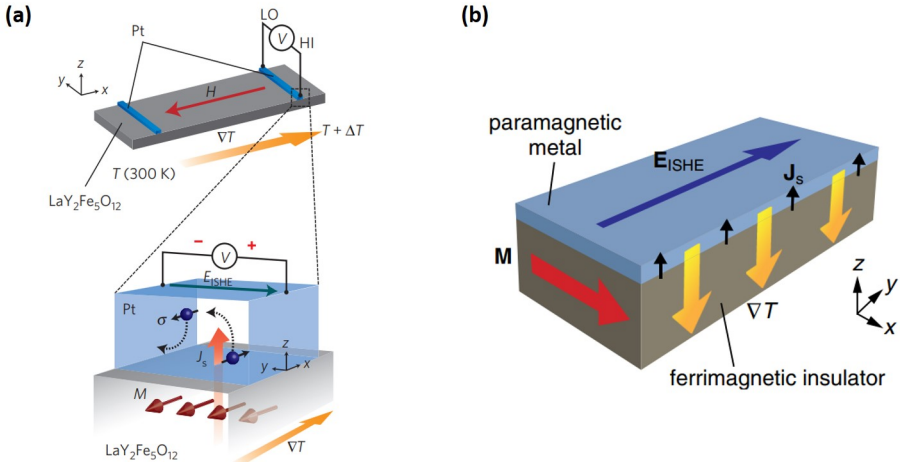

Figure 1.5: Illustration of transverse (a) and longitudinal (b) spin Seebeck measurement geometry. Adopted from [123] and [43] respectively.

Chapter 2

Manipulation of Magnetic Anisotropy in Rare Earth Iron Garnet Thin Films and Observation of Topological Hall Effect in TmIG/Pt

This chapter contains materials published in Qiming Shao, Yawen Liu, Guoqiang Yu, Se Kwon Kim, Xiaoyu Che, Chi Tang, Qing Lin He, Yaroslav Tserkovnyak, Jing Shi and Kang L. Wang. Topological Hall effect at above room temperature in heterostructures composed of a magnetic insulator and a heavy metal. Nat. Electronics 2, 182–186 (2019)

2.1 Brief Introduction to Rare Earth Iron Garnet

Rare earth iron garnet (REIG) refers to the group of oxides with chemical formula $3R_2O_3{\cdot}5Fe_2O_3$ or $R_3Fe_5O_{12}$, where R stands for rare earth ions such as Y, Tm, Tb, Eu, etc. REIGs share the same cubic crystal structure with a unit cell of 160 atoms. The R^{3+} ions occupy 24 dodecahedral sites (or **c** sites) and are surrounded by O^{2-} ions forming a dodecahedron. 24 Fe^{3+} ions are on octahedral sites (or **d** sites) while the other 16 Fe^{3+} occupy tetrahedral sites (or **a** sites) [114]. The crystal structure diagram of REIG unit cell is shown in Figure 2.1.

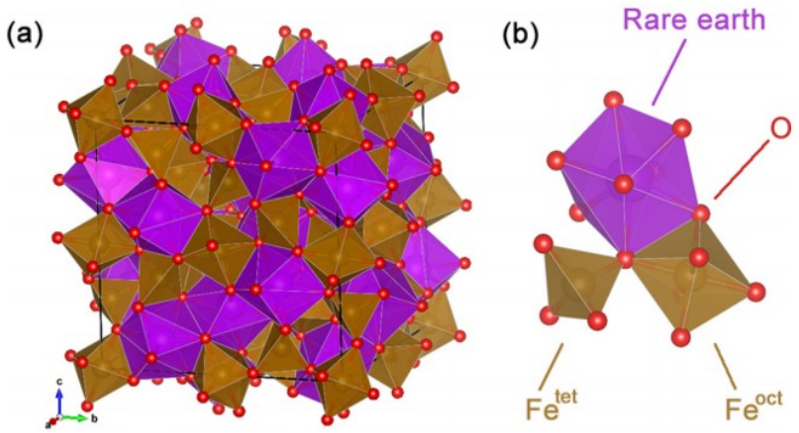

Figure 2.1: Crystal structure of rare earth iron garnets. (a) Cubic unit cell. (b) Local polyhedra environment experienced by Fe and R ions from their neighboring oxygen ions. Adopted from [77]

The magnetic property of REIG family is the so called ferrimagnetism. The magnetic moment of the **d** sites Fe^{3+} is strongly coupled to the **a** sites Fe^{3+} via superexchange which takes one O^{2-} as medium and the two sets of Fe^{3+} lie antiparallel to each other. Thus the Fe^{3+} ions provide a net moment of 40 μ_B per unit cell (at 0 K). As shown in Figure

2.2, different REIGs own almost identical Curie temperature (T_c). This is because that the net moment of Fe^{3+} dominates the total magnetic moment of REIGs at high temperature and T_c is thus determined by the strength of the Fe^{3+}-O^{2-}-Fe^{3+} superexchange. As for the R^{3+} ions, some of them exhibit no magnetic moment throughout the entire temperature range such as Y^{3+} and Lu^{3+}. As a result, the total magnetic moment of YIG and LuIG solely depends on the net moment of Fe^{3+} and monotonically increases as the temperature decreases. Some other R^{3+} such as Tm^{3+} and Tb^{3+} have magnetic moment that is antiferromagnetically coupled to the ferrimagnetic component of Fe^{3+}s in a relatively loose way. As the temperature decreases, the interaction between R^{3+} and Fe^{3+} becomes stronger and R^{3+} contributes larger moment. The temperature point that R^{3+} moment cancels out Fe^{3+} net moment is called compensation point at which the REIG exhibit no net magnetic moment. Above the compensation point, net moment of REIG aligns with Fe^{3+} net moment, while below it is towards the R^{3+} moment direction. Fe^{3+} net moment is then antiparallel to REIG's net moment below compensation point.

In recent years, magnetic insulators (MI) especially REIGs are playing an increasingly important role in spintronics studies. First, MI is a source that can generate pure spin current thermally via spin Seebeck effect or resonantly via spin pumping. In MI, spin current is in the form of spin waves that carry linear and angular momentum. The quanta of spin waves are called magnons; therefore, the spin current in MI is sometimes called magnonic spin current.[118] This advantage allows researchers to study how spin current propagate and convert to charge current in different materials and their unique behaviors. Second, spin currents in the form of spin waves in MI are free of Joule heating that ex-

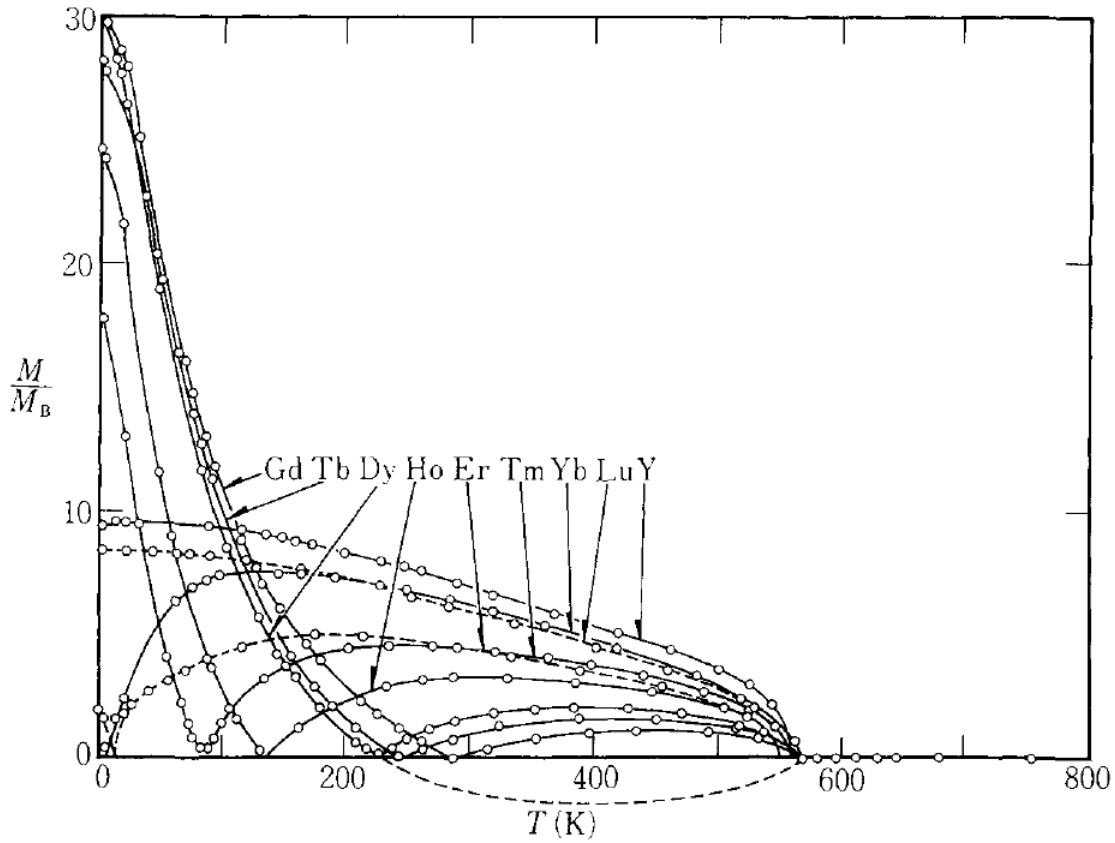

Figure 2.2: Temperature dependence of saturation magnetic moment of various rare earth iron garnets. [114]

ists in metals and semiconductors. When spin current is injected into MI, it is allowed to propagate with a much longer (micron meters [15])distance compared to it is in conductors (about a few nm). This offers the possibility to build next-generation energy-efficient all magnetic devices. Third, by stacking thin films of target material on MI thin films, target materials can acquire ferromagnetism and even spin-orbit coupling from the MI layer via proximity effect. The adjacent MI layer may significantly polarize the electronic states and modify the band structure of the target layer thus offer the opportunity to observe novel transport phenomena such as quantum anomalous Hall effect in topological insulator (TI)

and graphene [128, 36, 120, 73]. Any non-insulating magnetic material would unavoidably have current flowing through itself and mix its intrinsic anomalous Hall and magnetoresistance signal into the measurements. So MI-based heterostructures are unique and very helpful for this type of studies.

To better serve the purpose of building special MI-based heterostructure for certain goals, it is very important to engineer and manipulate the magnetic anisotropy of MI. In the next section, I will present how we grow high quality ferrimagnetic REIG thin films via pulse laser deposition (PLD) and control the property of their magnetic anisotropy by design via various methods.

2.2 Engineering of Magnetic Anisotropy in ReIG

2.2.1 Pulsed Laser Deposition

Pulsed laser deposition (PLD) is a common and powerful technique for oxide thin film growth. During my Ph.D research and in our lab, we have been using PLD to grow high-quality REIG thin films. In this subsection I will briefly introduce the technique of PLD growth and our home-made PLD system.

The main components and functionality of our PLD system are illustrated in Figure 2.3(a) and the real picture is shown in Figure 2.3(b). High-energy laser beam is focused by optical lens into a vacuum chamber and strikes the target material to be deposited. The struck target material then becomes plasma plume traveling to the top substrate, nucleates and forms uniform film there. During growth, the target keeps rotating to get uniformly

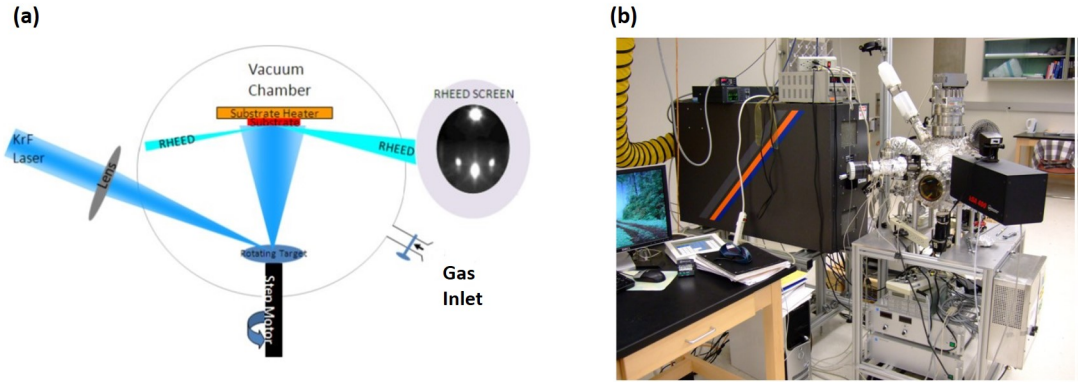

Figure 2.3: Schematic Illustration (a) and real picture (b) of pulsed laser deposition system

struck over a large area. Desired growth temperature that varies from material to material is set using the substrate heater on the sample holder. Depending on the type and property of the material, our chamber can grow under an ultra high vacuum (UHV) environment or ozone atmosphere by introducing a gas flow through the gas inlet. With the reflection high-energy electron diffraction (RHEED) component in our chamber, we can check the crystal quality of the film surface during and after growth. We can also track growth rate by counting number of layers based on RHEED oscillations like shown in Figure 2.4.

2.2.2 Magnetic Anisotropy

Magnetic anisotropy refers to the phenomenon that how how the free energy of a magnetic system depends on the directions of the magnetization. In ferromagnets, magnetic anisotropy determines the equilibrium magnetization orientation. In ferromagnetic thin films, the main origins of magnetic anisotropy are:

- Magnetocrystalline anisotropy: The behavior that magnetization in certain crystallographic directions takes more energy than in other directions is described as magne-

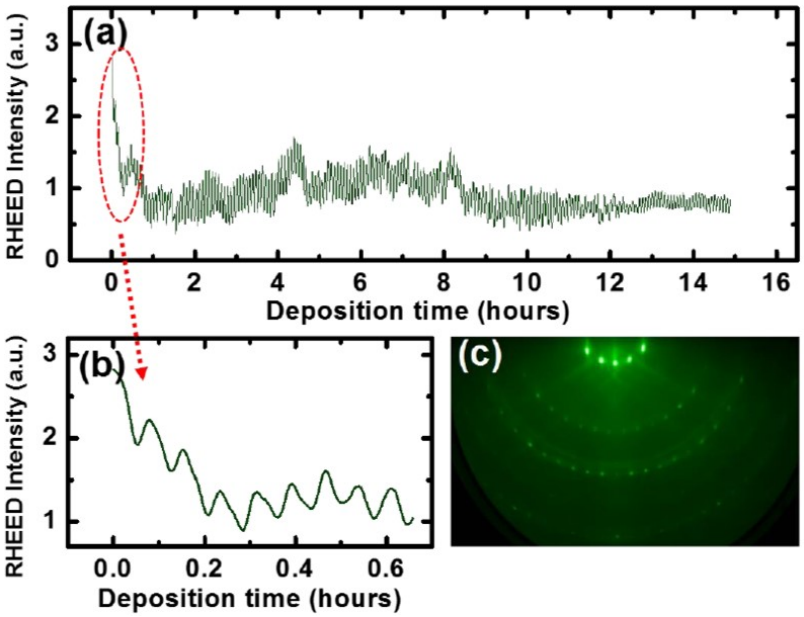

Figure 2.4: (a) 227 layers (100 nm) thick YIG film of continuous layer by layer RHEED oscillations observed during the growth on (110) GGG substrate using pulsed laser deposition technique. (b) Zoom-in data of RHEED oscillations for a chosen time slot. (c) RHEED pattern of YIG film showing single crystalline structure of YIG after deposition. Adopted from [119].

tocrystalline anisotropy. Magnetocrystalline anisotropy primarily origins from spin-orbit interaction. Mutual interaction of the magnetic dipoles may also contribute to it.

- Shape anisotropy: Shape anisotropy is simply the demagnetization field associated with shape of the sample. In thin films, a shape anisotropy energy $\frac{1}{2}\mu_0 M^2 cos^2\theta$ (where θ is the angle between the film normal and $\mathbf{M}$) leads to an energetic saving for keeping the magnetization in the film plane [5].

- Stress-induced anisotropy. Upon applying an external stress, ferromagnets may favor some magnetization direction energetically due to magnetoelastic effect.

2.2.3 Control of Magnetic Anisotropy in REIGs via Interfacial Strain and Magnetoelastic Effect

In most ferromagnetic thin films, the magnetic moment prefers the in-plane anisotropy due to relatively large demagnetization field. However, in many cases perpendicular magnetic anisotropy (PMA) is preferred. Researchers have been trying hard to engineer the magnetic anisotropy in ferromagnetic thin films. One of commonly used approach is tuning the anisotropy using magnetoelastic effect.

Magnetoelastic effect is also called inverse magnetostrictive effect. The magnetostriction constant λ characterize the shape change of ferromagnetic materials upon magnetization. And the inverse version, magnetoelastic effect characterizes how the sample's magnetization changes when mechanical stress σ is applied. The summarized facts of the effect of magnetostriction on the garnets' anisotropy are [22]:

1. Epitaxial magnetic films are normally in a state of mechanical stress σ due to the lattice mismatch between the film and substrate.

2. If the film is magneostrictive, the stress will produce a uniaxial magnetic anisotropy that is superimposed on the magnetocrystalline anisotropy.

3. For garnets with negative magnetostriction constant ($\lambda_{100}, \lambda_{111} < 0$), the magnetoelastic contribution tends to make the easy axis to be normal to the film plane if the the film is in tension ($\sigma > 0$), and a hard axis.is if the film is in compression ($\sigma < 0$).

Therefore, we can utilize the magnetoelastic effect to provide a uniaxial magnetic anisotropy in our REIG thin films. For materials like REIGs that have cubic crystal

structure, the effective perpendicular anisotropy field (H_A) can be derived by including the magnetostrictive contribution into the cubic anisotropy energy. The values for different film plane orientation are listed in Table 2.1.

Film Plane	H_A	
(100)	$(2K_1 - 3\sigma\lambda_{100})/M$	
(110)	$[2K_1 - 3\sigma(\lambda_{100} + \lambda_{111})]/2M$	M rotates in [110]
	$(2K_1 - 3\sigma\lambda_{111})/M$	M rotates in [100]
(111)	$(-4K_1 - 9\sigma\lambda_{111})/3M$	

Table 2.1: H_A of an epitaxial magnetic film for different film plane [22]

In our experiments, we have selected TmIG as the magnetic films to grow, its magnetostriction constants together with those of YIG and TbIG at room temperature are listed in Table 2.2. Regarding the lattice constants of TmIG being 12.323 Å, we obtained relatively large H_A in TmIG thin films on neodymium gallium garnet (NGG) substrate that has lattice constant 12.509 Å.

Material	$\lambda_{100}(10^{-6})$	$\lambda_{111}(10^{-6})$
TmIG	1.4	-5.2
TbIG	-3.3	12
YIG	-1.4	-2.4

Table 2.2: Magnetostriction constant of TmIG, TbIG and YIG [30]

2.2.4 Characterization of Magnetic Anisotropy in REIG Thin Films

it is important to have reliable characterization methods to quantitatively keep track of the engineered magnetic anisotropy field in REIG films. Here we introduce two

commonly used measurable terms from which H_A can be calculated, as well as how they can be measured:

- Saturation field H_{sat}: When magnetic field is applied along the hard axis or hard plane of a ferromagnet, the point where magnetization becomes saturated is called saturation field. In ferromagnetic thin films with PMA, H_{sat} can be obtained when applying an in-plane external field. And this H_{sat} satisfies the following relation with respect to H_A and $4\pi M_s$ where M_s is the saturation magnetization of the film:

$$H_A = H_{sat} + 4\pi M_s \tag{2.1}$$

  M-H curves of ferromagnets, from which H_{sat} can be easily read out, are usually measured with vibrating sample magnetometer (VSM). Another way we can also obtain H_{sat} is to perform Hall measurement. For ferro- or ferri- magnetic insulators such as REIGs, this can be done by measuring electric signals in the adjacent thin heavy metal (HM) layer deposited on top of REIG. Anomalous Hall effect (AHE) signal would arise from the Hall channel of the HM layer [121, 110]. At the same temperature, the AHE signal level is directly proportional to the magnitude of REIG's magnetic moment **M** in the out-of-plane direction. We apply external field in the in-plane direction. When the field is small, **M** stays perpendicular to the film plane due to its PMA property thus AHE signal stays as maximum value. And when the field is large enough, **M** will be pulled to the film plane and AHE signal will vanish due to zero out-of-plane **M** component. In this way we can get H_{sat} from the AHE vs. H curve..

- Effective demagnetization field M_{eff}: As it is named, M_{eff} is the effective demagne-

tization field when we take H_A into consideration. $4\pi M_{eff}$ is related to $4\pi M_s$ and H_A as:

$$4\pi M_{eff} = 4\pi M_s - H_A \tag{2.2}$$

M_{eff} can be determined from the angular dependence of ferromagnetic resonance (FMR) resonance field, which FMR is a method widely used for characterizing g-factor, magnetic anisotropy field, damping constant and et al. By measuring and fitting the angular dependence of FMR resonance field, we can extract out $4\pi M_{eff}$ and g factor simultaneously. The illustration of the coordinate system used in the analysis is shown in Figure 2.5 (a) and equations we base on are Equation 2.3 - 2.6, where $\theta_{H(M)}$ is the polar angle of the external field(magnetization), ω is the angular frequency of microwave, γ is the gyromagnetic ratio that $\gamma = g\mu_B/\hbar$, where g, μ_B and $\hbar$ are g-factor, Bohr magneton number and reduced Planck constant, and H_R is the resonance field at given ω and θ_H [71]. By solving for the expressions of θ_M from 2.3 and from 2.4 - 2.6 separately, a formula associating H_R with θ_H and other constant parameters can be derived. Thus we can obtain a H_R vs. θ_H relation for given $4\pi M_{eff}$ and g-factor. Thanks to their relatively orthogonal affects on the H_R vs. θ_H curves (Figure 2.5 (b) and (c)), we can fit the best values of these two parameters by comparing calculated relations with experimentally measured data. With the $4\pi M_{eff}$ value got from fitting, we can simply calculate H_A from Equation 2.2.

$$sin(2\theta_M) = (2H_R/4\pi M_{eff})sin(\theta_M - \theta_H) \tag{2.3}$$

$$(\frac{\omega}{\gamma})^2 = H_1 \times H_2 \tag{2.4}$$

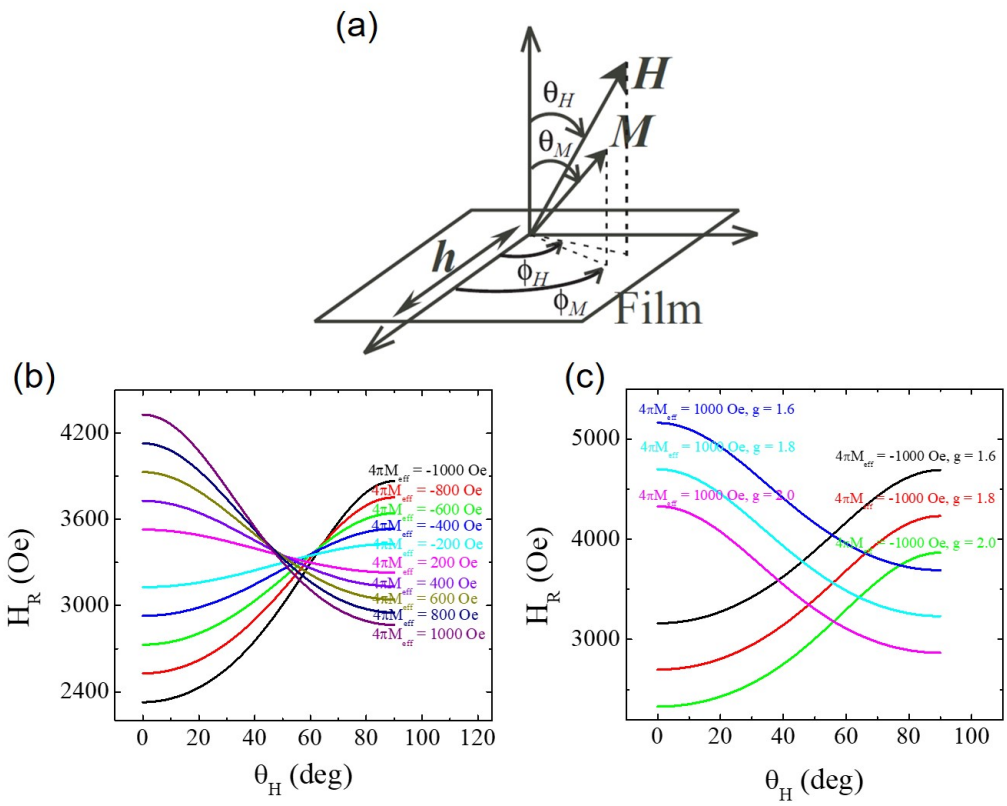

Figure 2.5: Schematic illustrations of the coordinate system used in the analysis of FMR and H_R vs. θ_H for with different $4\pi M_{eff}$ and g. (a) Coordinate system illustration. Adopted from [71]. (b) When changing $4\pi M_{eff}$ value alone, H_R vs. θ_H curve (g = 2.0) mainly rotates. (c) When g is varying, H_R vs. θ_H curve is shifting up or down. We used frequency f = 9.32 GHz which is the cavity frequency in our Bruker EPR facility for calculating curves in (b) and (c).

$$H_1 = H_R cos(\theta_H - \theta_M) - 4\pi M_{eff} cos^2\theta_M \tag{2.5}$$

$$H_2 = H_R cos(\theta_H - \theta_M) - 4\pi M_{eff} cos2\theta_M \tag{2.6}$$

2.2.5 High-quality TmIG Thin Films with Perpendicular Magnetic Anisotropy

We used our homemade PLD to grow high-quality TmIG thin films. The target was densified from powder that was synthesized using similar methods as described in [106]. We selected NGG(111) as the substrate as it provides relatively large tensile strain due to

lattice mismatch with TmIG [121]. Before deposition, the substrates went through standard cleaning process and then were baked at $\sim 220^{\circ}$C with a base pressure $< 10^{-6}$ for at least five hours inside the PLD chamber. We used a 248 nm KrF excimer pulsed laser running at 156 mJ and 1 Hz frequency to strike at the target. Typical growth time varies from 10 minutes for ultra thin films up to 12 hours to get thick ones. After growth, the films were annealed ex-situ using rapid thermal annealing (RTA) at 750 °C for 300 seconds under atmosphere with oxygen gas flow.

To check the crystalline quality, surface morphology and magnetic property of the TmIG films, we performed RHEED, atomic force microscopy (AFM), VSM and FMR measurement on the annealed samples. Characterization data of a representing 10 nm thick TmIG film is shown in Figure 2.6.

2.3 Observation of THE in TmIG/Pt via Controlling over Magnetic Anisotropy

2.3.1 Magnetic Skyrmions in Magnetic Insulators

Magnetic skyrmions are quasiparticles [113] that haven been predicted theoretically [7, 100, 16] and observed experimentally [99, 75, 27]in condensed matter systems. Compared to trivial magnetic bubbles [63], the recently discovered skyrmions in B20 compounds and transition metal/ heavy metal thin films have the following outstanding advantages to serve the interest of being used as information carriers [75, 37, 23]. First, it has been demonstrated that the size of skyrmions can be scaled down to sub-100 nm in material

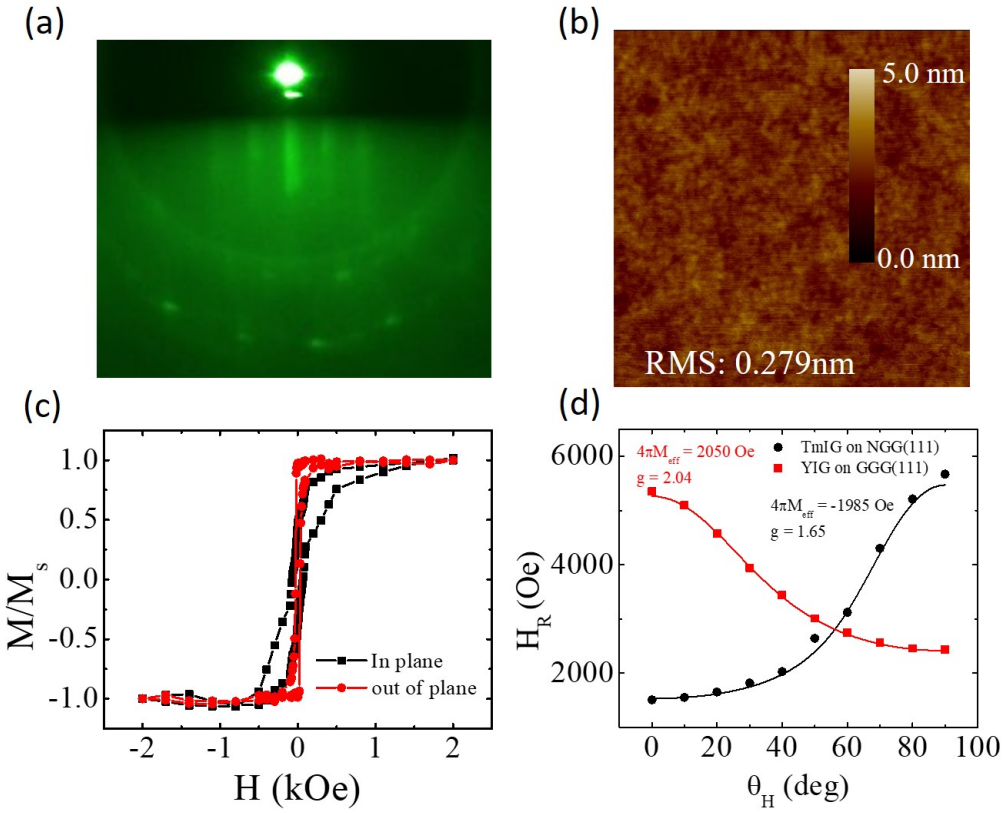

Figure 2.6: Characterization data of 10 nm TmIG film on NGG(111) substrate. (a)RHEED pattern with clear rod feature indicates that the surface is good single crystalline (b) Atomic force microscopy image shows that the surface of the film is ultra flat. (c) M-H curve measured with VSM demonstrates that the magnetic film has its easy axis in the out-of-plane direction. (d) FMR angular dependence data and the corresponding fitting result of PMA TmIG and easy-plane YIG. A negative $4\pi M_{eff}$ value of -1985 Oe indicates that magnetic moment prefers out-of-plane direction.

systems with substantial Dzyaloshinskii-Moriya interaction (DMI) due to inversion symmetry breaking either in bulk or at the interface [19], which is much smaller than the size of magnetic bubbles that was around 0.1 - 10 μm . Second, by applying low magnitude of electric current and electric field, skyrmions can be moved [37, 131, 125], which has big convenience for the purpose of scaling skyrmion-based devices compared to applying external magnetic field. Third, for the purpose of designing applicable memory devices, electrical

writing and reading is essential. It has been demonstrated that writing of skyrmions can be achieved via spin-polarized current at room temperature [35, 138], meanwhile skyrmions can be detected electrically with topological Hall effect (THE). THE origins from Berry phase acquired by the spin-polarized carriers when they travel through a skyrmion texture [80, 140].

MIs that host skyrmions are particularly attractive. since they have very low damping and allow long-distance information transmission free of Joule heating [38]. Moreover, various exotic phenomena based on magnon-skyrmion interactions [103], like magnon quantum Hall [78], long-range magnon transport [83], and magnon driven skyrmion motion [46], have been predicted in insulating skyrmion systems. To date, however, the only B20 magnetic insulator (Cu_2OSeO_3) that has been reported to host bulk DMI-stabilized skyrmions has a Curie temperature ($T_C \sim 60$ K)[105]. In this insulating skyrmion system, magnetic excitations[85] and thermally-driven skyrmion motion[72, 89] have been observed. The choice of magnetic insulators is limited due to the strict requirement of the crystal structure with inversion symmetry breaking, which is essential to generate strong DMI. The commonly studied high-temperature magnetic insulators, like garnets and ferrites, are centrosymmetric and thus magnetic bubbles lack a preferred chirality due to the absence of DMI.

2.3.2 Observation of the Topological Hall Effect

In our experiment, we realized the electrical detection of above-roomtemperature magnetic skyrmions by observing a pronounced THE in a bilayer heterostructure composed of the TmIG thin film in contact with a Pt film. The TmIG films grown on NGG(111)

as explained in previous section exhibit robust PMA at room temperature. A thin 4-nm-thick Pt layer was then sputtered on the TmIG at room temperature. Exchange coupling between TmIG and Pt makes the conducting electrons spin-polarized, which results in the AHE, spin Hall magnetoresistance (SMR) as well as the THE (Figure 2.7) at and above room temperature in a patterned Hall bar device. Assuming a smooth spin texture, we obtained a generic expression for antisymmetric Hall resistivity (ρ_{xy}) based on symmetry grounds

$$\rho_{xy} = \rho_o B_z + \rho_A m_z + \frac{\rho_T}{4\pi} \iint d^2 r m \times (\frac{\partial m}{\partial x} \times \frac{\partial m}{\partial y}) \tag{2.7}$$

where ρ_o is ordinary Hall effect (OHE) coefficient, ρ_A is the saturation AHE resistivity, m_z is the average z component of the magnetization unit vector in the Hall contact area and the third term is the THE contribution (ρ_{THE}). In the THE term, ρ_T is the THE coefficient and the integral counts how many times m(r) = m(x,y) wraps a unit sphere, which is the skyrmion number in real space.

We observe a typical sharp hysteresis loop of ρ_{xy} as a function of out-of-plane external field (B_z) for the TmIG (3.2 nm)/Pt (4 nm) bilayer at 350 K (Figure 2.7(b)), where the step function at low fields is due to the AHE, and the linear background with a negative slope at large fields arises from the OHE. Above 350 K, unusual ρ_{xy} dips at low positive fields and peaks at low negative fields emerge and gradually disappear at large fields as shown in Figure 2.7(b). We identity the overshoot in these out-of-plane hysteresis loops as the THE due to the presence of magnetic skyrmions[137, 65]. Moving spinpolarized electrons (as evidenced by AHE and SMR) can pick up the skyrmion-induced Berry phase by adjusting their spins to the local spin direction of the skyrmion texture, which gives rise to the THE.

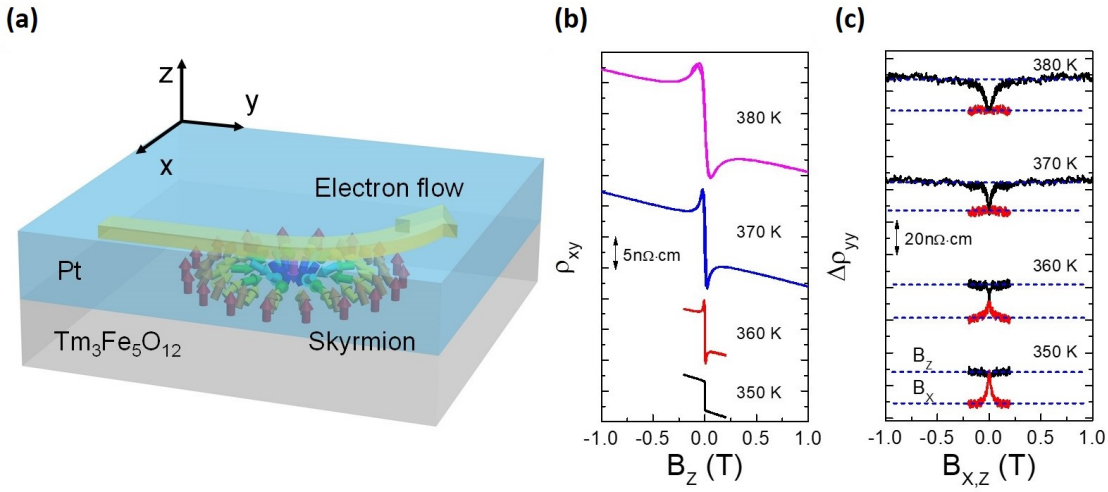

Figure 2.7: Illustration of the THE and transport properties in TmIG/Pt. (a), Schematic of the THE in the TmIG/Pt. The current at the TmIG/Pt interface goes through the emergent electromagnetic field generated by the skyrmion in the TmIG and gives rise to the transverse Hall current. (b), Hall resistivity as a function of the out-of-plane magnetic field at different temperatures. Above 350 K, the THE is observed as peaks and dips occur at low fields. (c), Longitudinal resistivity as a function of both out-of-plane (black, along the ±z direction) and in-plane (red, along the ±x direction) magnetic fields at different temperatures, from which we determine the out-of-plan magnetization component of TmIG as a function of external field using the theory of spin Hall magnetoresistance. The data are offset for clarity. All data are from the TmIG (3.2 nm)/Pt (4 nm) bilayer.

To obtain the AHE contribution in ρ_{xy}, we determine mz as a function of B_z by tracking the change in longitudinal resistance $\delta\rho_{yy}$ (Figure 2.7(c)) because $\delta\rho_{yy} \propto m_z^2$ according to the theory of SMR[11]. We plot the measured ρ_{xy} and the simulated contributions from the OHE and AHE together in Figure 2.8(a) for T = 360 K, where we observe an apparent difference between these two plots. By subtracting the contributions from the OHE and AHE, we determine the magnitude of ρ_{THE} (Figure 2.8(a)).

2.3.3 Field and Temperature Dependence

To host magnetic skyrmions in the TmIG, there must be a sizeable interfacial DMI energy (D) at the interface between the TmIG and the Pt for stabilizing magnetic chiral structures. Experimentally, Pt/ferromagnetic metal bilayers have been reported to show a very strong interfacial DMI, $D \approx 1 - 2mJ \cdot m^{-2}$, which supports sub-100 nm skyrmions at room temperature[74, 131]. In theory, we also expect to have a sizeable interfacial DMI at the TmIG/Pt interface due to a strong coupling between Pt and Fe atoms, as evidenced by the AHE and SMR. We estimated the magnitude of D in our TmIG/Pt bilayer by employing a domain wall motion technique as described in ref.[87]. The determined D is $\sim 51\mu Jm^{-2}$ at room temperature ([108] Supplementary Note 3). Although the absolute value of D at room temperature for our TmIG/Pt is smaller than the case in Pt/ferromagnetic metal bilayers, the ratio of D over exchange stiffness (A) is comparable as A is estimated to be $\sim 0.84pJm^{-1}$ ([108] Supplementary Note 4). To highlight the importance of interfacial DMI, we applied an in-plane external field to overcome the DMI effective field and eliminate the magnetic chiral structures. Experimentally, we observed that, when the applied in-plane field increases, the overshoot in the out-of-plane hysteresis loops becomes less obvious (Figure 2.8(b)), which suggests reduced THE.

The appropriate anisotropy energy (K) of TmIG is achieved by varying the temperature to satisfy the requirement for the presence of skyrmions. Theory shows that K should be $\leq \frac{\pi^2}{16}\frac{D^2}{A}$ to form a skyrmion lattice [115], which suggests that skyrmions can only be stabilized in a weak anisotropy regime. For our TmIG/Pt, K can be continuously tuned from positive (PMA) to negative (easy-plane anisotropy) by changing the tempera-

ture, which passes the zeroanisotropy energy. This tunability is critical for the formation of skyrmions in a window of temperature. The increase of temperature reduces K, most probably due to the reduced magneto-elastic coefficient that contributes to the PMA. To illustrate the importance of the tunable K, we plot the temperature dependence of K in Figure 2.8(c). K is initially much larger than $\frac{\pi^2}{16}\frac{D^2}{A}$ at T = 300 K. As the temperature increases, K decreases then eventually becomes negative. By varying the temperature, we obtain a skyrmion phase diagram from the THE as a function of temperature and external field (Figure 2.8(d)). We can see that the THE emerges when K is close to zero. With sizeable D and appropriate K, we conclude that the presence of magnetic skyrmions is the driving force for observation of the THE in TmIG/Pt.

Then we look at the external field dependence of THE. We anticipate a spin spiral phase (or a balanced number of skyrmions with topological charge +1 and -1) near zero field and a ferromagnetic phase at large fields, in which the THE is minimized. We estimate the stability of a skyrmion lattice by employing a free energy minimization method, in which we consider exchange, anisotropy, DMI and Zeeman energy [6, 2]. Here, we assume a perfect hexagonal skyrmion lattice for simplicity of calculation. Because ρ_{THE} is proportional to the skyrmion density, we compute a skyrmion density diagram as a function of normalized K and Zeeman energy (Figure 2.8(e)), where $B_E = M_S B_z$ is the Zeeman energy ([108] Supplementary Note 5). Full micromagnetic simulations reveal an even larger skyrmion window of K and Bz when the magnetostatic energy is included ([108] Supplementary Note 6). In agreement with the calculated skyrmion density in Figure 2.8(e), ρ_{THE} at a given temperature first increases and then decreases with the external field (Figure 2.8(d)).

Also, below 370 K, ρ_{THE} at a given field increases as the temperature increases (Figure 2.8(d)) due to the reduced PMA (Figure 2.8(c)), which agrees with Figure 2.8(e) and is consistent with the very recent observation in Ir/Fe/Co/Pt multilayers [115]. Furthermore, we observe a larger external field window at a higher temperature for stable skyrmions in Figure 2.8(d) when K transitions from PMA ($K > 0$) to easy-plane anisotropy ($K < 0$) near 370 K (Fig 2.8(c)). Thanks to the great tunablity of K in the TmIG/Pt bilayer by varying the temperature, the stability of skyrmions against an external field is enhanced and the ρ_{THE} is increased in the easy-plane anisotropy regime. Our observations are consistent with calculations (Figure 2.8(e)) and the prediction of ref. [2]. Therefore, the temperature and external field dependences of THE agree with the theoretical expectations, confirming the existence of magnetic skyrmions in TmIG/Pt.

2.3.4 Thickness Dependence of Magnetic Insulator TmIG

We now investigate the TmIG thickness (tTmIG)-dependent THE in TmIG/Pt (4 nm) bilayers to clarify the importance of the interfacial DMI. Because the magnitude of the interfacial DMI is inversely proportional to the ferromagnetic layer thickness [14], we do not expect the presence of magnetic skyrmions in the thick TmIG limit. In extremely thin TmIG, the ferromagnetism disappears. Experimental results as a skyrmion phase diagram for the THE for t_{TmIG} = 3.2, 4 and 6 nm are shown in Figure 2.9(a)–(c). There are two major findings. First, for all TmIG thicknesses, the THE only emerges when the magnetic anisotropy is in the transition from PMA to easy-plane anisotropy or close to zero. This is consistent with theory, as discussed above. Second, near the magnetic anisotropy transition temperature, the temperature–field window of the THE becomes smaller as tTmIG increases

and eventually disappears for $t_{TmIG} = 6.4$ nm ([108] Supplementary Note 7). This shows that even when K meets the conditions for skyrmion formation, the skyrmion cannot exist in thicker films. The absence of the THE in thicker TmIG films suggests that the DMI is negligible in these films, which is consistent with an interfacial DMI from the Pt/TmIG interface.

We also investigated the possibilities of other topological origins for the ρ_{THE} and the skyrmion density inferred from the observed ρ_{THE}. First, our ρ_{THE} is unlikely to be due to the emergent magnetic field associated with avoided band crossings in reciprocal space [116, 117], which requires a crystalline structure, because the TmIG is an insulator with no itinerant electrons and Pt is a normal metal with no topological characteristics. Furthermore, our Pt is at best polycrystalline due to the nature of the sputtering process, which can average out the effects of the emergent magnetic fields. Second, the noncollinear spin texture at the atomic scale, which has been shown to be able to induce AHE in frustrated magnets, cannot be used to explain our ρ_{THE} as the TmIG is not a frustrated magnet. The ρ_{THE} must therefore be due to the presence of magnetic skyrmions and related localized chiral spin textures that carry non-zero topological charge. Experimentally, we achieved a maximum ρ_{THE} around 4.6 $n\Omega \cdot cm$ for the 3.2-nm-thick TmIG. This corresponds to a maximum skyrmion density (ρ_{sk}) around 4,800 μm^{-2} if we use $\rho_{THE} = \frac{\rho_0 Ph}{e}\rho_{sk}$ [80]. Here, $\rho_0 = -4.64 \times 10^{-12}\Omega \cdot cm \cdot mT^{-1}$, $\frac{h}{e}$ is the quantum flux and we assume P = 0.1. This is much larger than the estimated maximum skyrmion density (Figure 2.8(e)), which is $\sim 70\mu m^{-2}$. This discrepancy has also been reported in metallic magnetic multilayers [115, 62] and could be due to multi-band transport, distorted spin texture and the non-

adiabatic effect [95]. The difference between the measured and estimated ρ_{THE} in various skyrmionic platforms is the latest topic to attract extensive discussions ([108] Supplementary Note 5).

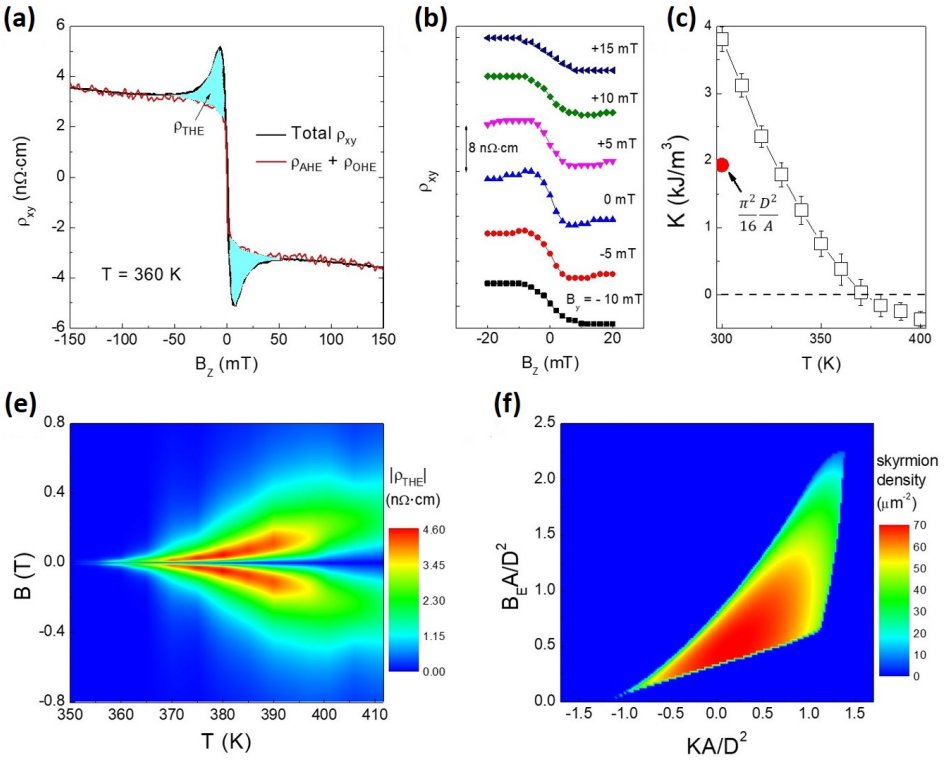

Figure 2.8: Observation of THE. (a), Hall resistivity (black curve) as a function of an out-of-plane magnetic field at T = 360 K. The red curve shows the contribution of the AHE and the OHE. The light blue region indicates the contribution of THE. (b), Out-of-plane Hall hysteresis loops in the presence of different in-plane external fields. (c), Anisotropy energy K (black square symbols and curve) as a function of T. The red symbol is $\frac{\pi^2}{16}\frac{D^2}{A}$, where D is the interfacial DMI energy and A is the exchange stiffness. The anisotropy transitions from PMA to easy-plane anisotropy near 370 K. Error bars are estimated from the uncertainty in determining the effective anisotropy field and magnetization. (d), Skyrmion phase diagram from the THE as a function of temperature T and external field B_z. The color bar indicates the value of measured THE resistivity. Interpolation between experimentally measured data points is applied. (e), Theoretical skyrmion density diagram as a function of the normalized anisotropy energy (KA/D^2) and the Zeeman energy (B_EA/D^2). All data are from the TmIG (3.2 nm)/Pt (4 nm) bilayer.

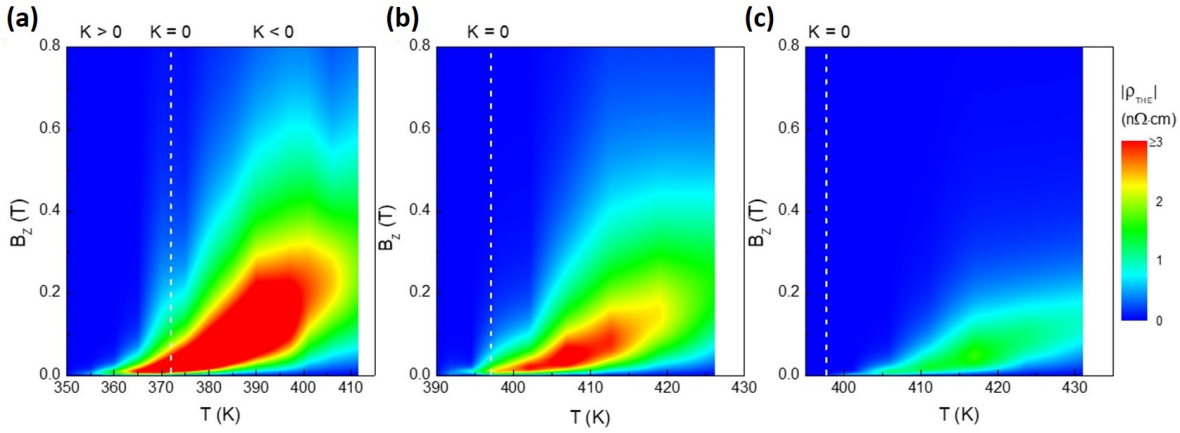

Figure 2.9: Magnetic insulator thickness dependence of the THE. (a)–(c), Experimentally obtained evolution of the skyrmion phase diagram as a function of TmIG thickness (t_{TmIG}) in TmIG/Pt (4 nm) bilayers with $t_{TmIG} = 3.2$ nm (a), $t_{TmIG} = 4$ nm (b) and $t_{TmIG} = 6$ nm (c). Note that the highest THE resistivity drops as t_{TmIG} increases (4.58, 3.44 and 1.66 $n\Omega cm$ for 3.2, 4 and 6 nm, respectively) (Figure 2.8(d) and [108] Supplementary Note 7). Dashed white lines indicate the temperature at which the magnetic anisotropy transitions from PMA to in-plane anisotropy ([108] Supplementary Figure 7). We set the highest value of the plotted THE resistivity to 3 $n\Omega \cdot cm$ to provide good color contrast. Interpolation between experimentally measured data points is applied.

Chapter 3

Study of Anomalous Hall Effect and Spin Seebeck Effect in Ferromagnetic Insulator Based Heterostrucutures

3.1 Overview of Anomalous Hall Effect in in Ferromagnetic Insulator Based Heterostrucutures

Thin films of ferrimagnetic insulator (FMI) such as YIG, TmIG and TbIG have offered many unique opportunities for exploring new physical effects associated with magnonics and spintronics [3, 28, 11, 94, 79, 54, 67, 15]. In particular, they have been widely used with heavy metals (HM) to form heterostructures such as bilayers and trilayers in which a

variety of interesting pure spin current related phenomena have been discovered including the spin Seebeck effect (SSE) [124], spin-orbit torque (SOT) [1, 110] anomalous Hall effect (AHE) [28, 55, 67], magnon-mediated current drag [52], and the spin Hall magnetoresistance (SMR) effect [11, 79, 7]. Among them, the AHE is seemingly the simplest but in fact the most intriguing effect that has not yet been completely understood. Since the electrons in FMI/HM heterostructures travel only in the HM layer, the AHE has to arise from two possible origins: (a) the HM interface layer becomes magnetized via proximity coupling with the FMI; (b) spin current generated by the spin Hall effect in HM partially enters the FMI depending on the magnetization direction of the FMI. These two mechanisms are independent from each other but can also coexist.

In YIG/HM bilayers, perhaps the most studied FMI/HM heterostructures, YIG films have in-plane magnetic anisotropy. Hence, the AHE response should saturate as the YIG magnetization is fully aligned with the perpendicular magnetic field which occurs at $\sim 2kOe$. In reported experimental data, however, the AHE signal is always found to increase until the magnetic field reaches a much higher level ($>$ 10 kOe) [28, 68]. This large discrepancy raises a serious question about the origin of the field-dependent Hall signal. Another puzzling feature is that the AHE signal shows a sign reversal below room temperature in YIG/Pt [28, 67] but not in YIG/Pd [55], which has not been satisfactorily addressed and therefore demands further investigations. Thanks to the perpendicular anisotropy (PMA) of TmIG films, the low-field Hall responses in TmIG/Pt exhibit a characteristic hysteresis loop which allows for straightforward identification of the AHE signal associated with FMI magnetization [121, 1, 110]. Recently, AHE results in TmIG/W have been analyzed by

tracking the hysteresis loops in the low field range [107]. Both the minimum in AHE and the sign reversal in TmIG/W were attributed to an increased contribution of the proximity-induced effect as the temperature is decreased. For the proximity-induced contribution in rare earth iron garnet (REIG)/HM, the AHE likely share a common origin due to the wave-function hybridization of the 3d-electrons of Fe in REIG with the conduction electrons in HMs. Understanding the AHE temperature dependence in TmIG/Pt will shed light on the physical origin of the AHE in other REIG/HM heterostructures.

3.2 Temperature Dependence of Anomalous Hall Effect in TmIG/Pt heterostructures

3.2.1 Observation of Low-field and High-field Anomalous Hall Effect in TmIG/Pt and their Sign Changes

15 nm thick TmIG films are grown on (111)-oriented neodymium gallium garnet (NGG) substrates using pulse laser deposition (PLD). Robust PMA is obtained in the strained TmIG films as described in chapter 2. Typical characterization data is shown in Figure 2.6. TmIG films are then transferred to a high-vacuum magnetron sputtering chamber for metal deposition. To prevent possible oxidation, a 5 nm SiO_2 layer is deposited on top of Pt or Cu/Pt before exposed to air. We perform standard photolithography to fabricate Hall bar devices with the length of 300 μm and the width of 100 μm. Magneto-transport measurements are carried out in Quantum Design's Physical Property Measurement System over the temperature range of 5 to 300 K and with the magnetic field up to 12 T.

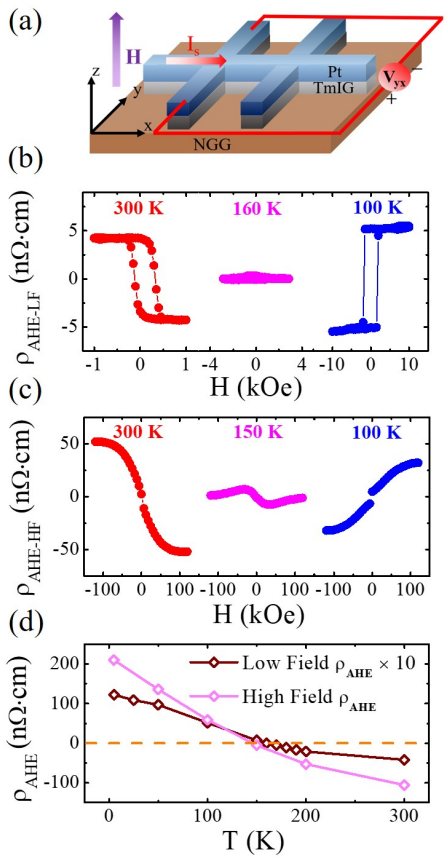

Figure 3.1: Illustration of AHE sign change and temperature dependence in TmIG/Pt (3nm). (a) Schematic diagram of device geometry and measurement setup. (b) and (c) Low-field (ρ_{AHE-LF}) and high-field (ρ_{AHE-HF}) AHE hysteresis at different temperatures after subtracting the linear ordinary Hall background. Sign change occurs in both ρ_{AHE-LF} and ρ_{AHE-HF}. (d) Temperature dependence of the saturation values of both ρ_{AHE-LF} and ρ_{AHE-HF}. ρ_{AHE-LF} is magnified by 10 times.

We first present the AHE results of TmIG/Pt (3 nm) in Figure 3.1 The device and measurement schematics are shown in Figure 3.1(a). In the low-field range, a clear Hal (ρ_{yx}) hysteresis loop can be observed at 300 K. After subtracting the linear background, the low-field squared loop is shown in Figure 3.1(b) and denoted as ρ_{AHE-LF}. It has the opposite sign to the normal magnetic hysteresis loop, and therefore it is negative. When the sample is cooled down from room temperature, it undergoes a sign reversal at $\sim 150K$ and turns

positive at lower temperatures. The coercive field increases with decreasing temperature, which is consistent with the increasing trend of the magnetostriction coefficient at low temperatures [31].

When extending the measurements to a higher field range up to 12 T, we observe an increasing AHE signal denoted as ρ_{AHE-HF} that only saturates at higher fields (Figure 3.1(b)). By measuring ρ_{AHE-HF} at different temperatures, we find that it changes sign at $\sim 150K$, which approximately coincides with the sign change temperature of the ρ_{AHE-LF}. Systematic temperature dependence comparison for both low- and high-field (at 12 T) AHE signals displayed in Figure 3.1(c) clearly shows that they follow the same trend, but ρ_{AHE-HF} is one order of magnitude larger than ρ_{AHE-LF}. In YIG/Pt bilayers reported previously, a similar high-field behavior was also observed [28, 68]. However, due to the easy-plane anisotropy of YIG, the low-field component was seamlessly blended with the high-field signal, which is common to all YIG/HM bilayers. Thanks to the PMA of TmIG films, these two components can be readily separated from each other. The squared ρ_{AHE-LF} loop can be easily identified with the TmIG magnetic hysteresis loop, but the ρ_{AHE-HF} response is not obvious.

Similar high-field AHE signal was reported in Pt deposited on SiO_2 substrate that includes 7% Fe atoms [68]. In our bilayer structure fabrication, however, room temperature Pt sputtering deposition and subsequent lithography processes should not cause Fe outward diffusion into the Pt layer to form inclusions and thus we do not consider the superparamagnetism from Fe-rich particles. This scenario can further be refuted by the fact that the observed saturation field remains largely temperature independent. We also exclude

the possibility of the nonlinear ordinary Hall effect from two bands [61]. Its failure on this scenario can be easily demonstrated with the unreasonable parameters obtained from the following fitting results:

When the carriers are from multiple channels, the total transverse conductivity can be written as:

$$\sigma_{xy}^{tot} = \sum_i \frac{n_i e \mu_i^2 B}{1 + \mu_i^2 B^2} \tag{3.1}$$

If $\mu_i B \sim 1$ in one channel, a nonlinear $\sigma_{xy}^{tot} vs. B$ curve will be observed. The other channels have low mobility, i.e., $\mu_i B \ll 1$ and $(\mu_i B)^2$-term in the denominator can be ignored. Then here we can use a simple form to include both the high- and low-mobility channels,

$$\sigma_{xy}^{tot} = \frac{n_{hi-eff} e \mu_{hi}^2 B}{1 + \mu_{hi}^2 B^2} + n_{0-eff} e \mu_0^2 B \tag{3.2}$$

where n_{hi-eff} and n_{0-eff} are carrier densities associated with the two channels which could be from the interfacial and the bulk parts of Pt film respectively. The best fits are shown in Figure 3.2 and the fitting parameters are listed in Table 3.1. As we can see from the fitting results, although the fits capture the nonlinearity of both curves, the resulting mobility of one channel is as high as $\sim 103\ cm^2 \cdot V^{-1} \cdot s^{-1}$. Such a high mobility channel is unlikely to exist in the sputtered polycrystalline Pt films. In addition, its corresponding effective carrier density needs to change sign as well as the temperature is decreased. Thus, we conclude that the two-band model is not suitable to account for the high-field nonlinear Hall signal.

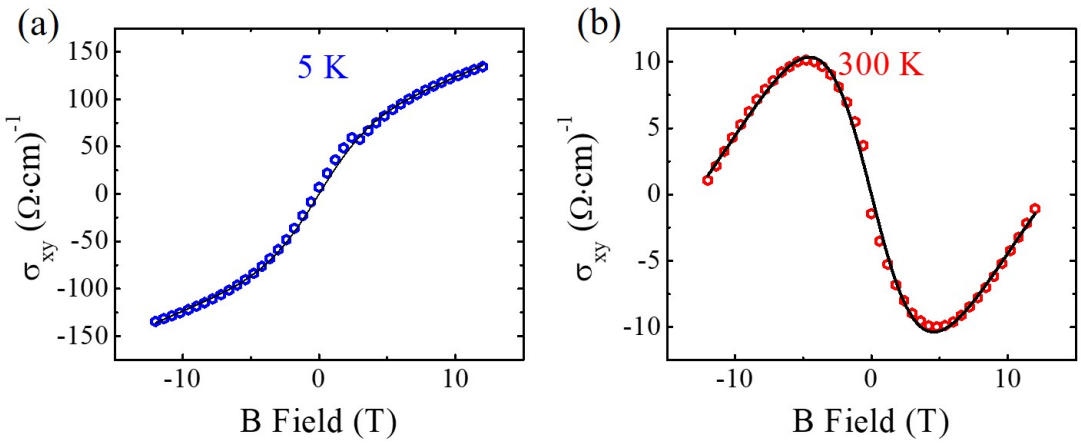

Figure 3.2: Fitting of σ_{xy} vs. B at 5 K (a) and 300 K (b) of AHE in TmIG/Pt(2 nm) based on the two-band model

T (K)	$n_{hi-eff}(m^{-3})$	$\mu_{hi}(cm^2 \cdot V^{-1} \cdot s^{-1})$	$n_{0-eff}(m^{-3})$	$\mu_0(cm^2 \cdot V^{-1} \cdot s^{-1})$
5	3.7×10^23	1590	6.1×10^25	91
300	-1.1×10^23	1641	3.6×10^25	39.3

Table 3.1: Fitting results of high-field AHE in TmIG/Pt(2 nm) with two-band model at 5 K and 300 K

Despite the smooth TmIG surface, atomic level surface roughness such as step edges unavoidably exists. Conduction electrons in Pt interact with all interfacial Fe moments, including both strongly and weakly coupled moments to the TmIG layer magnetization. The latter requires high magnetic fields to saturate, which we interpret as the source of ρ_{AHE-HF}. Although the actual mechanism remains unclear, here we assume that the proximity-induced Pt moments by loosely coupled interfacial Fe moments in TmIG behaves as nearly independent entities with their own anisotropy.

3.2.2 Anomalous Hall Effect in TmIG/Cu/Pt and Absence of High-field Feature and Sign Change

One important question to address here is the role of the spin current effect, the alternative mechanism for AHE in FMI/HM [11]. This effect arises from the spin current entering the FMI in the form of the spin transfer torque, but does not rely on the existence of the proximity-induced magnetic interface in HM resulting from interfacial hybridization. To clarify the role of the interface, we fabricate and perform systematic measurements on two control samples: TmIG/Cu(3 nm)/Pt(2 nm) and NGG/Pt(2 nm). In the first sample, the TmIG/Pt interface is absent, so is the proximity-induced magnetic layer in Pt. However, the thin Cu layer should be transparent to spin current except for interface attenuation. In the second sample, no magnetic interface is present. Figure 3.3(a) displays the 300 K data of three relevant samples over a large magnetic field range. A striking feature is that ρ_{AHE-HF} does not exist unless Pt is put in direct contact with TmIG.

The ρ_{AHE-LF} results of the three samples are equally striking. There is no hysteresis in NGG/Pt on any field scale, as expected of paramagnetic Pt. The contrast between the other two samples is more interesting. We have seen in Figure 3.1(a) that ρ_{AHE-LF} of TmIG/Pt(2 nm) is $\sim -5n\Omega \cdot cm$. Although invisible in Figure 3.3(a), the ρ_{AHE-LF} of TmIG/Cu(3)/Pt(2) is now clearly present in Figure 3.3(b) on a magnified scale. At 300 K, ρ_{AHE-LF} is only$\sim +0.03n\Omega \cdot cm$, with the opposite sign and two orders smaller in magnitude compared to TmIG/Pt. Moreover, as the temperature is decreased to 150 K, ρ_{AHE-LF} increases by a factor of five but maintains the positive sign, which is in sharp contrast with the behavior of TmIG/Pt. Therefore, after the insertion of a thin Cu layer between TmIG

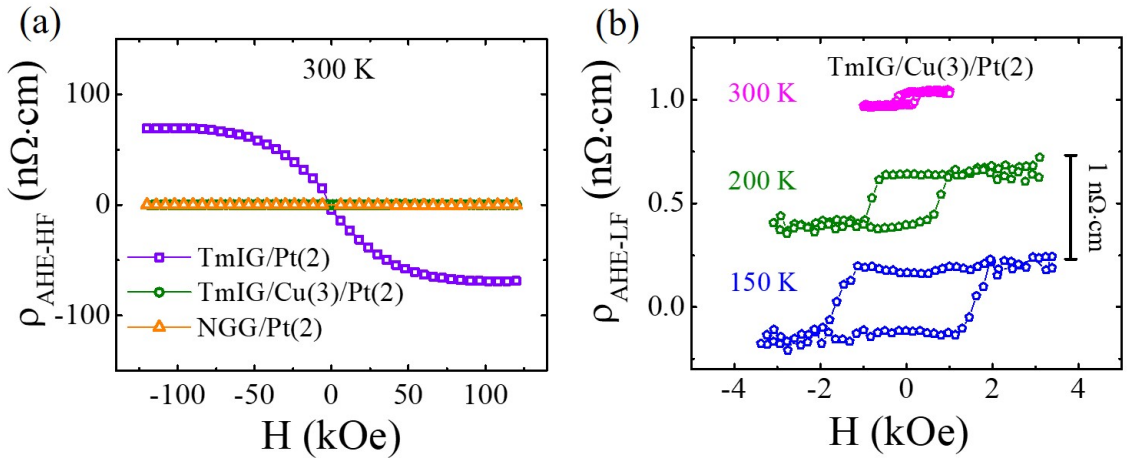

Figure 3.3: AHE in control samples. (a) ρ_{AHE-HF} of TmIG/Pt(2), TmIG/Cu(3)/Pt(2) and NGG/Pt(2) measured at 300 K. Numbers in the parentheses indicate the thickness in nanometer. Only TmIG/Pt(2) shows a high-field AHE signal. (b) ρ_{AHE-LF} in TmIG/Cu(3)/Pt(2) at 300, 200 and 150 K. ρ_{AHE-LF} monotonically increases without sign change from 300 K to 150 K.

and Pt, not only is ρ_{AHE-HF} completely quenched, but also the negative ρ_{AHE-LF} is totally suppressed and replaced by a much smaller positive signal. Moreover, the temperature dependence is distinctly different. These facts strongly suggest that the proximity effect at the TmIG/Pt interface is responsible for producing the large room-temperature negative AHE signal. Nevertheless, there should be a secondary contribution to AHE that may originate from the spin current effect. Since the spin current is not expected to decay in such a thin Cu layer due to the long spin diffusion length of Cu ($\sim$ 350 nm) [33], its contribution to AHE should largely be preserved after the Cu layer insertion except for shunting. This much smaller effect, even though it coexists, is overshadowed by the dominant proximity-induced AHE in TmIG/Pt. Within the framework of the spin current model, the sign of the AHE is determined by several physical quantities, but only the imaginary part of the spin-mixing conductance could change the sign when the chemical potential is varied [11].

The absence of the AHE sign change in TmIG/Cu/Pt indicates a smooth spin-mixing conductance near the Fermi energy. In YIG/Ag, density functional theory (DFT) calculations show no sign change over a large chemical potential range ($\sim$ eV) [34]. It is possible that the spin-mixing conductance in TmIG/Cu does not have radical changes either, although detailed DFT calculations have not yet to be reported.

3.2.3 Temperature Dependence of Anomalous Hall Effect in TmIG/Pt and TmIG/Cu/Pt with Different Layer Thicknesses

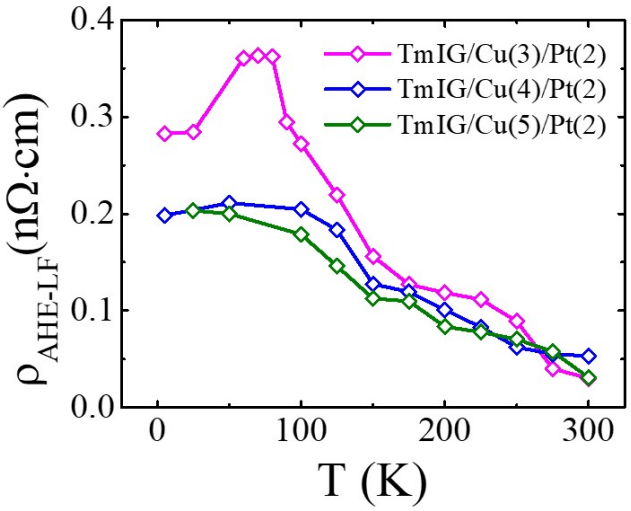

Figure 3.4: Temperature dependence of AHE in TmIG/Cu(t_{Cu})/Pt(2 nm). Temperature dependence of AHE in TmIG/Cu(t_{Cu})/Pt(2 nm) exhibit same trend with similar magnitude for t_{Cu} varies from 3 nm to 5 nm

To further show the contrast between the samples with and without the Cu-layer, we have also studied the temperature dependence of AHE in TmIG/Cu(t_{Cu})/Pt(2) and TmIG/Pt(t_{Pt}) with varying metal layer thicknesses t_{Cu} and t_{Pt}. As shown in Figure 3.4, in samples with t_{Cu} = 3, 4, and 5 nm, only the ρ_{AHE-LF} component is observed. At 300 K,

the ρ_{AHE-LF} magnitude for all three samples is $\sim +0.03 n\Omega \cdot cm$ insensitive to the Cu layer thickness and consistent with its long spin diffusion length. Furthermore, the measured AHE has the same sign and follows the same trend over the entire temperature range, which also rules out possible pin holes in Cu through which Pt connects TmIG directly.

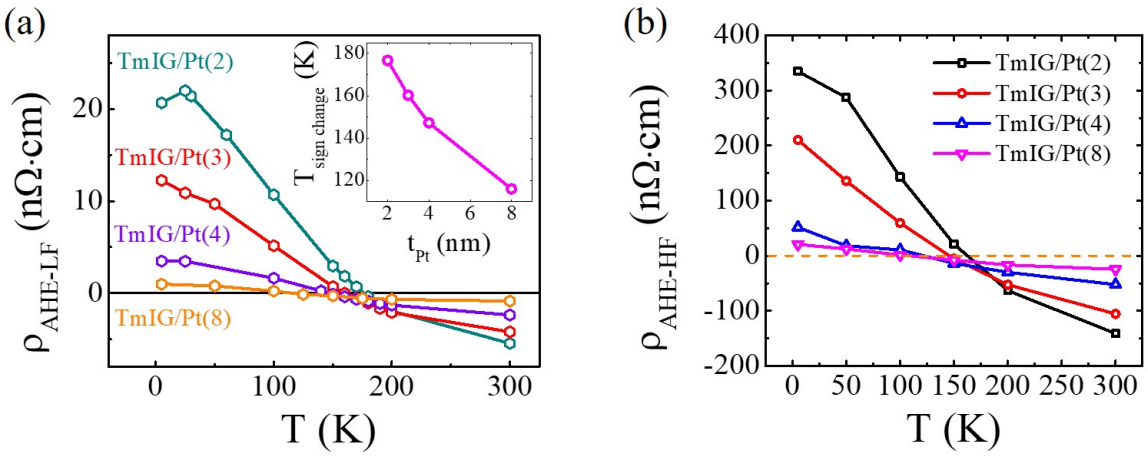

Figure 3.5: Temperature dependence of low-field (a) and high-field (b) AHE in TmIG/Pt with different Pt thickness.

In the TmIG/Pt(t_{Pt}) samples with t_{Pt}=2, 3, 4 and 8 nm, both the low- and high-field components change the sign within a narrow temperature window (Figure 3.5). As t_{Pt} varies from 2 to 8 nm, we observe a continuous shift in the sign change temperature from 175 K to 115 K (Figure 3.5(a) inset). In the meantime, the ρ_{AHE-LF} decreases by one order of magnitude, which suggests the interfacial nature of the proximity-induced effect.

3.2.4 First-principles Calculation of Anomalous Hall Effect Temperature Dependence in TmIG/Pt

To reveal the mechanism of the temperature dependence of AHE in TmIG/Pt, we have performed DFT calculations [4, 49, 48, 47, 88]. The intrinsic anomalous Hall conductivity (AHC) is calculated using the Kubo-formula approach [136]:

$$\sigma_{xy}^{z} = \frac{e^2}{\hbar} \sum_{\mathbf{k}} \Omega^{z}(\mathbf{k}) = \frac{e^2}{\hbar} \sum_{\mathbf{k}} \sum_{n} f_{\mathbf{k}n} \Omega_{n}^{z}(\mathbf{k}) \tag{3.3}$$

and

$$\Omega_{n}^{z}(\mathbf{k}) = \sum_{n' \neq n} \frac{2Im[< \mathbf{k}_n | V_x | \mathbf{k}_{n'} >< \mathbf{k}_{n'} | v_y | \mathbf{k}_n >]}{(\epsilon_{\mathbf{k}n} - \epsilon_{\mathbf{k}n'}^{2})} \tag{3.4}$$

where $f_{\mathbf{k}n}$ is the Fermi occupation factor of the n-th eigenstate with a wavevector $\mathbf{k}$, and Ω_{n}^{z} is the Berry curvature for the n-th band. We have simulated the proximity effect of TmIG on Pt by making a weakly magnetized bulk Pt. To match the TmIG substrate a 4% tensile strain along the (111) plane is applied. According to previous reports, the proximity-induced magnetic moment in Pt ranges from 0 0.1 μB in different layers[94, 61, 53]; therefore, we have used the median value of 0.05 μB per Pt atom in the present calculations. From Equation 3.3, the AHC is determined by integrating the Berry curvature in the entire Brillouin zone for all bands below the Fermi energy. In Figure 3.6(a), we plot the Berry curvature of this hypothetical bulk Pt. It is clear that the Berry curvature is large only near the L point. Such a large Berry curvature is produced by two bands near the Fermi energy as shown in the Figure 3.6(b), where the blue (red) color in the band structures represents a positive (negative) contribution to the Berry curvature. Since the energies of these two bands are so close to the Fermi energy, their occupation numbers are very sensitive to temperature. As shown in Figure 3.6(c), the occupation of band 1 at the L point decreases

very rapidly with temperature when we consider the effect of the Fermi distribution function at finite temperatures. This results in the monotonic decrease of AHC with the temperature and eventually its sign reversal at around 150 K as displayed in Figure 3.6(d)., in a good agreement with the experimental observation. Using the longitudinal resistivities from experimental data ($\rho_{xx} = 4.2 - 5.1 \times 10^{-5}\ \Omega \cdot cm$ in a temperature range of 5 K-300 K) and the relationship $\sigma_{xy} = \rho_{yx}/\rho_{xx}^2$, the calculated values of ρ_{yx}, 8.4 $n\Omega \cdot cm$ at 5 K and - 3.4 $n\Omega \cdot cm$ at 300 K, both agree reasonably well with the corresponding experimental values in Figure 3.5(a).

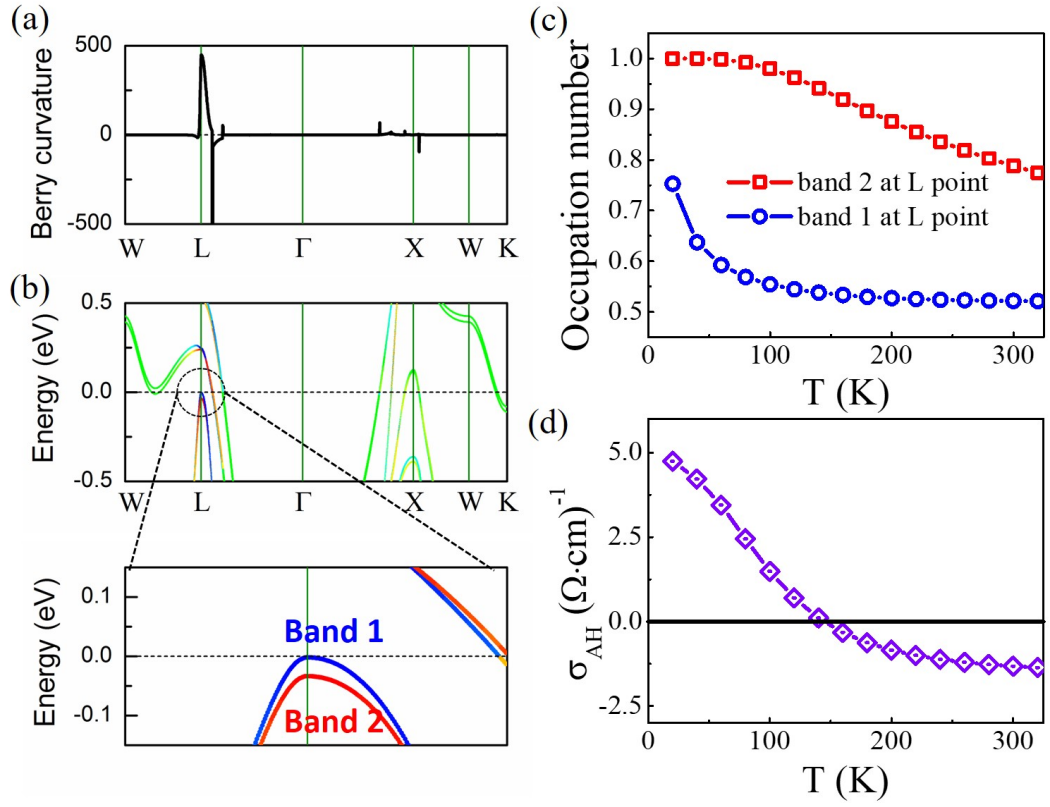

Figure 3.6: DFT calculation results of AHE conductivity of Pt on TmIG. (a) Berry curvature and (b) band structure of strained Pt with a magnetic moment of 0.05 μB. (c) Temperature dependence of occupation number of bands 1 and 2 at L point and (d) the resulting temperature dependence of AHC σ_{AH}.

We have also conducted calculations with different magnitudes of induced moment in Pt ranging from 0.05 μB to 0.20 μB (Figure 3.7) and found that the sign change point smoothly shifts to right as the moment increases. This qualitatively matches the trend of the sign change temperature in Figure 3.5(a) as we reduce the thickness of the Pt films. Therefore, as our simple DFT calculations explain all the main features of our experimental results for TmIG/Pt, the AHE should mainly stem from the induced ferromagnetism in HM.

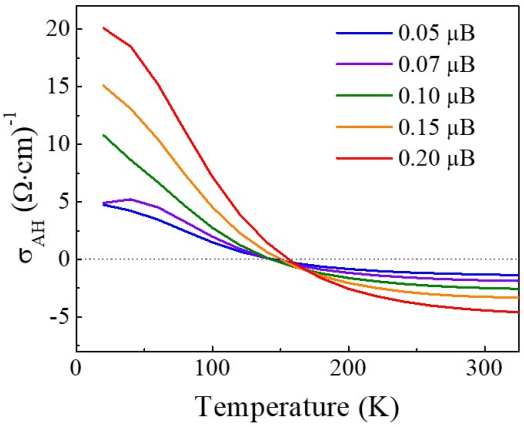

Figure 3.7: Temperature dependence of AHE conductivity σ_{AH} of Pt calculated from DFT with different magnitudes of magnetic moment.

3.2.5 Magnetic Compensation in TmIG Measured by Anomalous Hall Effect

In TmIG, Tm^{3+} has a 4f-magnetic moment which is anti-aligned with the net Fe^{3+} moment in each formula unit. As the temperature is decreased, the Tm moment gradually increases. At a particular temperature when the moments from Tm and Fe atoms cancel each other, this is the so-called magnetic compensation. In $\sim$ 50 % of samples grown for

this study, the magnetic compensation effect has been observed. The actual reason for the compensation temperature variation is unclear. Under an external magnetic field, the direction of the net magnetic moment of Fe^{3+} flips above and below the compensation temperature. In TmIG, the 3d-electrons of Fe are more delocalized than the 4f-electrons of Tm. Therefore, in the TmIG/Pt bilayers the magnetic moments of Fe instead of Tm dictates the induced ferromagnetism in Pt, and in the TmIG/Cu/Pt trilayers, the spin transfer torque is dominated by the interaction with the Fe moments. This process reflectsed in the abrupt sign reversal of the AHE responses in both TmIG/Pt and TmIG/Cu/Pt as shown in Figure 3.8(a). If we simply reverse the sign of the measured AHE signal below the compensation temperature, the AHE should follow a smooth temperature dependence trend, which is indeed the case as shown in 3.8(b). Upon reversal of the AHE signal for the samples with magnetic compensation, the temperature dependence of AHE for all samples can be compared with each other on an equal footing.

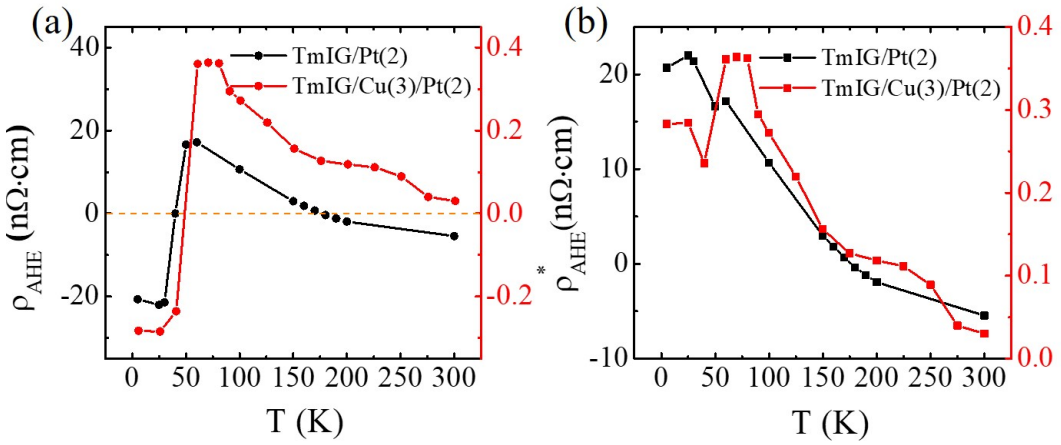

Figure 3.8: Magnetic compensation in TmIG measured by AHE. (a) Temperature dependence of AHE in TmIG/Pt(2) and TmIG/Cu(3)/Pt(2) with different vertical scales. A common sign flip occurs at around 50 K in both samples. (b) Temperature dependence of AHE in TmIG/Pt(2) and TmIG/Cu(3)/Pt(2) after the AHE sign in (a) is manually reversed below the compensation temperature point. The overall trend of both sign corrected curves evolve smoothly with temperature.

Chapter 4

Study of Spin Transport in Ferromagnetic/Antiferromagnetic Insulator Based Heterostructures

4.1 Introduction to Spin Transport in Antiferromagnetic Insulator Related Heterostructures

4.1.1 Overview of Antiferromagnetic Materials in Spintroncis

In modern spintronic devices, structures based on ferromagnetic (FM) materials have been the focus of study, e.g. spin valve and magnetic tunnel junction devices. Antiferromagnetic (AFM) materials, however, mostly serve as a static supporting role that pins one of the FM layers via the exchange-bias effect [66, 82], due to its lack of readable net magnetic moment. In the last two decades, rapid progress has been witnessed in the

study of spin Hall effect, spin Seebeck effect (SSE) and spin pumping (SP). Researchers are now able to realize more efficient pure spin current generation electrically, thermally or by resonantly applying microwave. Meanwhile better understanding on the transport property of spin current in different material systems is developed and higher-resolution detection is also achieved. For the purpose of building next-generation energy-efficient spintronic devices, AFMs have attracted tremendous attention because of their unique properties:

- AFMs exhibit negligible stray fields because of their vanishing magnetization on macroscopic scale. This provides AFMs robustness against perturbation due to magnetic fields [64] thus ensures scalability of magnetic nanodevices [50, 84].

- AFMs display ultrafast dynamics. Magnetic resonance in AFMs, which is called antiferromagnetic resonance (AFMR), operates in the terahertz (THz) regime [20, 45, 42, 81], which is at least two orders larger than typical ferromagnetic resonance in gigahertz (GHz) range in ferromagnetic (FM) materials. And the resonance frequency in AFMs is governed by the strong exchange interaction between antiparallel aligned sublattice spins as different to it in FMs, which is determined by the magnetic anisotropy and Zeeman energy. The higher-frequency spin dynamics in AFMs makes it possible to be used for ultrafast information processing and communication.

- AFMs host magnons with opposite charalities. Either charality can be selectively excited by electromagnetic waves with left or right circular polarization, or by applying magnetic field to lift degeneracy of the two chiral eigenmodes.

4.1.2 Magnetic Resonance in Uniaxial Antiferromagnetic Materials

Due to the absence of net moment, magnetic resonance condition in AFM materials displays different characteristic behaviors compared to ferromagnetic (FM) materials. The physical picture of AFMR represents some of the unique properties of AFMs in spin dynamics. While in AFMR magnons are excited coherently, which is different from the incoherently excited magnons in SSE, the field dependence of AFMR is still very helpful to understanding SSE in AFMs. Here I briefly go through the derivation of AFMR in an uniaxial AFM material formulated by Kittel [42].

We denote the magnetic moment of the two sublattice in an uniaxial AFM as $\mathbf{m}_1$ and $\mathbf{m}_2$. Treated with the mean field approximation, the exchange fields applied on sublattice 1 and 2 are:

$$\mathbf{H}_1(ex) = -\lambda \mathbf{m}_2; \mathbf{H}_2(ex) = -\lambda \mathbf{m}_1 \tag{4.1}$$

where λ is positive. We also denote the crystalline anisotropy field as $\mathbf{H}_A$ and z-direction external field (along the easy axis determined by crystalline anisotropy) as $\mathbf{H}_0$. Neglecting damping terms, equations of motion of the two sublattice magnetization are:

$$\frac{d\mathbf{m}_1}{dt} = \gamma[\mathbf{m}_1 \times \mu_0 \mathbf{H}_{eff}] = \gamma[\mathbf{m}_1 \times \mu_0(\mathbf{H}_0 + \mathbf{H}_A - \lambda \mathbf{m}_2)] \tag{4.2}$$

$$\frac{d\mathbf{m}_2}{dt} = \gamma[\mathbf{m}_2 \times \mu_0 \mathbf{H}_{eff}] = \gamma[\mathbf{m}_2 \times \mu_0(\mathbf{H}_0 - \mathbf{H}_A - \lambda \mathbf{m}_1)] \tag{4.3}$$

The signs of $\mathbf{H}_A$ are different in the two equations because the crystalline anisotropy acts in opposite directions for $\mathbf{m}_1$ and $\mathbf{m}_2$. The two positive resonance angular frequencies solved from 4.2 and 4.3:

$$\omega_{res} = \pm\gamma\mu_0 H_0 + \gamma\mu_0[H_A(2H_{ex} + H_A)]^{1/2} \tag{4.4}$$

where H_{ex} is magnitude of the sublattice exchange field. The two corresponding eigenmodes

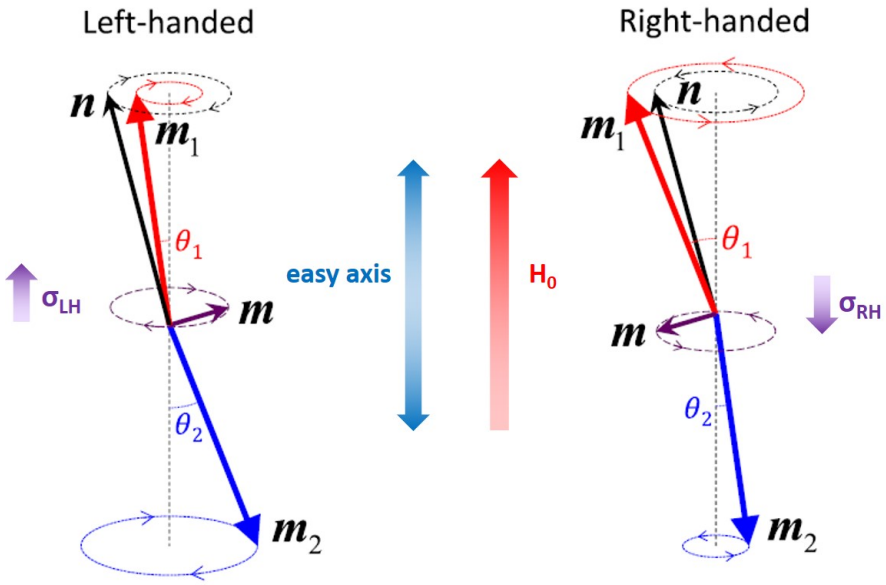

Figure 4.1: Illustration of the two eigenmodes in AFMR. The two eigenmodes of Equation 4.4 have opposite chiralities and opposite ratios between the cone angles of $\mathbf{m}_1$ and $\mathbf{m}_2$. A magnetic field along the easy axis breaks the degeneracy of the two modes. Adopted from [13].

are depicted in Figure 4.1.

This equation is essential in understanding the physical picture of AFMR. First, compared to the resonance condition in FMs, a finite resonance frequency exists at zero magnetic field due to the exchange and crystalline anisotropy. And the two eigenmodes are degenerate. Second, when a z-direction external field is applied, the degeneracy of two eigenmodes is lifted and the resonance frequency shows a linear response (until spin-flop transition field). They have opposite chiralities, opposite ratios between the cone angles of $\mathbf{m}_1$ and $\mathbf{m}_2$, and distinct resonance frequencies associated with different energy. We shall call the lower-frequency branch left-handed mode or β mode and call the higher-frequency one right-handed mode or α mode in later texts.

When a relatively large external field is applied in the direction perpendicular to the easy axis of an unaxial AFM, magnetic moment of the two sublattice will tilt towards the field direction and produce a net moment which we can call canted spin moment or canted moment for short (Figure 4.2 (a)). If the external field is applied parallel to the easy axis of AFM, the case is more interesting. At small field, the two sublattice moment $\mathbf{m}_1$ and $\mathbf{m}_2$ do not turn but stay in the easy-axis direction. When the field exceeds a critical point, the lowest energy state is shown in the right configuration of Figure 4.3 (b) thus there is a transition in the sublattice moment arrangement. This transition is called spin flop and we call the critical point spin-flop transition field (H_{SF}). Above the H_{SF}, a net moment will be generated in the field direction similar to the case in Figure 4.2 (a). In both situations, if the applied field is large enough, in principle Zeeman energy can eventually dominate over crystalline anisotropy and exchange interaction so that both sublattice moments can be totally aligned to the field direction.

With the concepts introduced above, we now look at and compare resonance modes in AFMs and FMs that have different chiralities and polarization orientations with respect to (effective) external field. We start with the case of ferromagnetic resonance (FMR) which is simpler. As shown in Figure 4.3 (a), magnetic resonance occurs in FMs as magnetic moment $\mathbf{m}$ precesses about the effective external field $\mathbf{H}_0$ coherently. It has right-handed chirality and polarization direction of the excited magnons is antiparallel to the effective field direction. As for AFMR, when the field is applied along the easy axis, it exhibits two eigenmodes with opposite chiralities and spin polarization as shown in Figure 4.1. The left-handed mode has polarization σ orientation same as external field $\mathbf{H}_0$ direction while

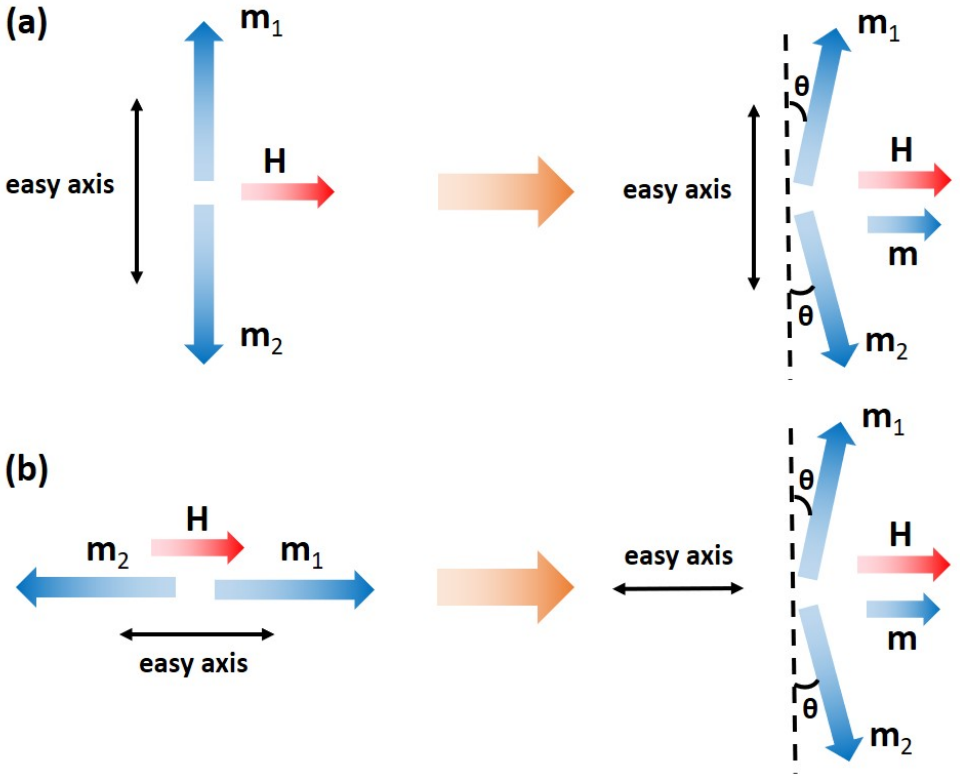

Figure 4.2: Illustration of canted spin moment and spin flop in AFM. (a) When a relatively large external field is applied perpendicular to the easy axis of AFM, a canted spin moment is induced. (b) When external field is applied along the easy axis and it is above a critical value, spin flop transition occurs associated with a net moment in the field direction.

the right-handed mode displays opposite orientation. When the external field applied along easy axis direction exceeds H_{SF} of the AFM material or the field is applied perpendicular to the easy axis, in both scenarios only the right-handed mode exists as illustrated in Figure 4.3 (b). We call it quasi-ferromagnetic resonance (QFMR) mode to be distinguished from the FMR mode. But as it is named, QFMR owns the same chirality and relative polarization orientation as they are in FMR.

A representing field-frequency diagram of AFMR in uniaxial AFM MnF_2 is shown in Figure 4.4. When the external field **H** is applied along the c-axis which is the easy axis

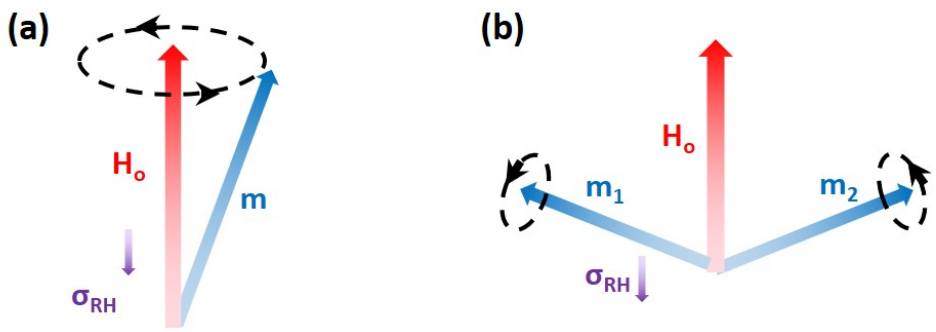

Figure 4.3: Illustration of FMR mode in FMs and QFMR mode in AFMs. (a) Schematic diagram of FMR mode in FMs (b) Illustration of QFMR in AFMs.

we denote before, the two linear branches with circle symbol correspond to the left-handed mode (lower branch) and right-handed mode (higher branch). After the H_{SF} at 9.27 T, the two modes collapse and emerge as one branch of QFMR mode. When **H** is applied perpendicular to c-axis, there is only one QFMR branch denoted with square symbol.

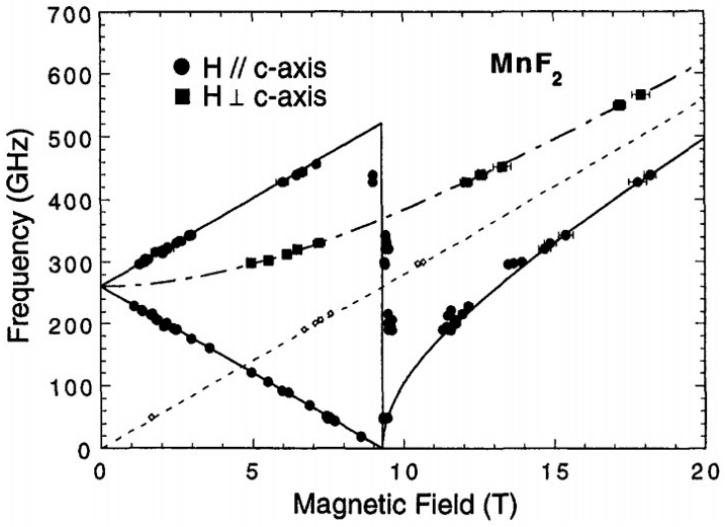

Figure 4.4: Frequency versus external magnetic field relations of the AFMR signals in MnF_2. Full dots and solid curves describe the data and theoretical results for field along easy axis configuration. Rectangles and dash dotted line characterize the perpendicular field configuration. The dotted line is the paramagnetic resonance line with g = 2.0. Adopted from [21]

4.1.3 Spin Seebeck Effect in Antiferromagnetic Insulators

There have been active studies in the origins of SSE in antiferromagnetic insulators (AFMI). In the early report, it was claimed that SSE in Cr_2O_3/Pt only shows up when a strong magnetic field above the H_{SF} is applied and the magnitude is proportional to the net equilibrium magnetization of Cr_2O_3 [104]. Later, Wu et al. reported that a finite SSE signal exists in MnF_2/Pt with applied field less than H_{SF}, indicating that field-induced moment should not be the single source of SSE in AFMIs [132]. From the physical picture of AFMR we have discussed previously, it is expected that a field applied in the easy-axis direction can create an imbalance in the two AFM magnon eigenmodes, which will give rise to a SSE signal that corresponds to the left-handed mode. And a characteristic SSE peak is supposed to appear as temperature varies [97, 98]. However, in neither of the previous reports of SSE in Cr_2O_3/Pt and MnF_2/Pt, there is clue of left-handed mode contribution. If there is any, the SSE signal below H_{SF} should show an opposite sign compared to it after H_{SF}. Recently Li et al. reported the observation of β mode (left-handed mode) AFM magnon contributed to SSE signal in FeF_2 associated with a characteristic peak at $\sim$11.6 K as shown in Figure 4.5 [51].

4.1.4 Overview of Spin Transport in Ferromagnetic/Antiferromagnetic Insulator Based Heterostrucures

Besides the active studies in AFMI based heterostructures, a great deal of attention has been paid to FMI/AFMI based heterostructures. Among them the most studied is probably YIG/NiO/Pt sandwich structure. In 2014, Wang et al. reported a robust spin

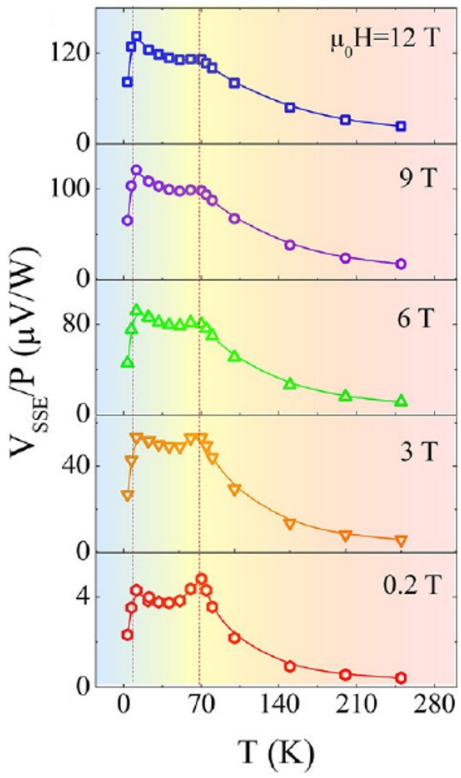

Figure 4.5: Temperature dependence of V_{SSE} in FeF_2/Pt heterostructuref V_{SSE}. Temperature dependence of V_{SSE}/P for H = 12, 9, 6, 3, and 0.2 T from top to bottom indicated by different colors. Two vertical dashed lines indicate the peak positions. Solid curves are guides to the eye. Adopted from [51]

propagation in YIG/NiO/Pt with NiO thickness up to 100 nm in their spin pumping measurement. They also found when a thin NiO layer ($\sim$ 1 nm) is inserted between YIG and Pt, there is an enhancement in the SP signal compared to Pt on bare YIG [127]. In 2016, an enhancement in SSE signal with thin NiO/CoO layer inserted between YIG and Pt/Ta was reported by Lin et al. [56]. In their SSE temperature dependence plot, a characteristic peak that is likely to be associated with Neel temperature (T_N) of the AFM thin film is depicted. Besides the interesting behaviors of SP and SSE in YIG/NiO/Pt, people also found that spin Hall magnetoresistance (SMR) signal undergoes an unique sign change in

such heterostructure that is absent in YIG/Pt. Lin et al. and Hou et al. reported this sign reversal of SMR separately. The former group attributed it to spin backflow at the YIG/NiO interface [57] and the latter one claimed that perpendicular coupling between the magnetic order of YIG and NiO should account for this phenomenon [26].

However, all these studies are more or less phenomenological. Considering the fact that NiO has tri-axial anisotropy in the (111) plane which is mostly studied, it is rather difficult to draw an intuitive but comprehensive physical picture of the coupling mechanism between the AFM NiO and FM YIG layer. Not to mention that NiO films grown on YIG are always polycrystalline and no epitaxial growth of NiO on single crystalline YIG has been realized yet. To address this issue of the magnetic moment coupling and spin transport mechanisms at the FMI/AFMI interface, an uniaxial AFMI is highly preferred. In 2018, Qiu et al. published a paper studying the SSE in YIG/Cr_2O_3/Pt heterostructure [93], which Cr_2O_3 is an unaxial AFMI. They claimed that their Cr_2O_3 films grown on YIG(111) have easy axis in the out-of-plane direction as shown in Figure 4.6(b). In such material system, a shut off of spin current is observed once the temperature is below T_N of Cr_2O_3 when the AFM order is established (Figure 4.6(e), (g) and (f)), no matter the spin current is generated thermally via SSE or by microwave excitation via spin pumping. The explanation they proposed is that spin current generated in the YIG layer with polarization direction in the film plane can not transmit through the AFM-state Cr_2O_3 layer with Neel vector perpendicular to the film plane.

The unique spin-current-shut-off behavior in YIG(111)/Cr_2O_3/Pt leaves some intriguing questions to be answered. Suppose we still choose YIG as our FMI layer and

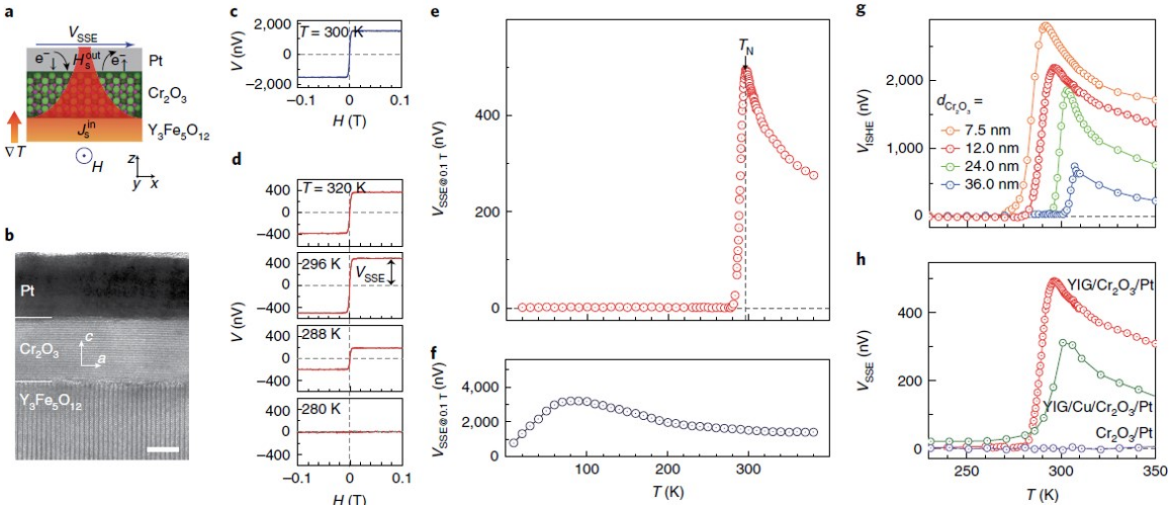

Figure 4.6: SSE measurement and result in YIG(111)/Cr_2O_3/Pt heterostructure. a, schematic illustration of SSE measurement in YIG/Cr_2O_3/Pt b, cross-sectional TEM image of the YIG/Cr_2O_3/Pt trilayer. The easy axis c of the Cr_2O_3 is in the out-of-plane direction. c, V_{SSE} vs. H in YIG/Pt at 300 K. d, The external magnetic field H dependencies of the voltage signal V measured in the YIG/Cr_2O_3/Pt trilayer device at various temperatures. e, The temperature dependence of the spin Seebeck voltage V_{SSE} at H = 0.1 T for the YIG/Cr_2O_3/Pt trilayer device at $d_{Cr_2O_3}$= 12 nm. f, The temperature dependence of the spin Seebeck voltage V_{SSE} at H = 0.1 T for a YIG/Pt bilayer device. g, The temperature dependence of spin pumping signals V_{ISHE} for YIG/Cr_2O_3/Pt trilayer devices with different Cr_2O_3 layer thickness. h, The temperature dependence of the spin Seebeck voltage V_{SSE} at H = 0.1 T for the various devices. Adopted from [93]

Cr_2O_3 as the AFMI layer. First, from the material science perspective, is it possible to grow epitaxial single crystalline Cr_2O_3 film on YIG with c axis in the film plane? There is strong motivation to achieve this as such a material structure would allow us to systematically study the very fundamental physical mechanism of spin transport at the AFM/FM interface. Second, in the desired material system, while spin current seems to be blocked when its polarization direction is orthogonal to the Neel vector, how would the transmission behave when the spin current polarization is parallel to the Neel vector of Cr_2O_3? Would the AFM magnon carry the spin current generated in the YIG layer and give rise to a finite SSE signal even after it is below T_N [44]? Moreover, if strong exchange coupling

exists at the AFMI/FMI interface, will that exchange field lift the degeneracy of two AFM magnon eigenmodes and give rise to a measurable SSE signal with the AFM layer as its source? With all these urgent and significant questions, we launched our research project of studying spin transport in YIG/Cr_2O_3 based heterostructure.

4.2 Growth of Cr_2O_3 Thin Films on YIG(110)

4.2.1 Crystal and Magnetic Structure of Cr_2O_3

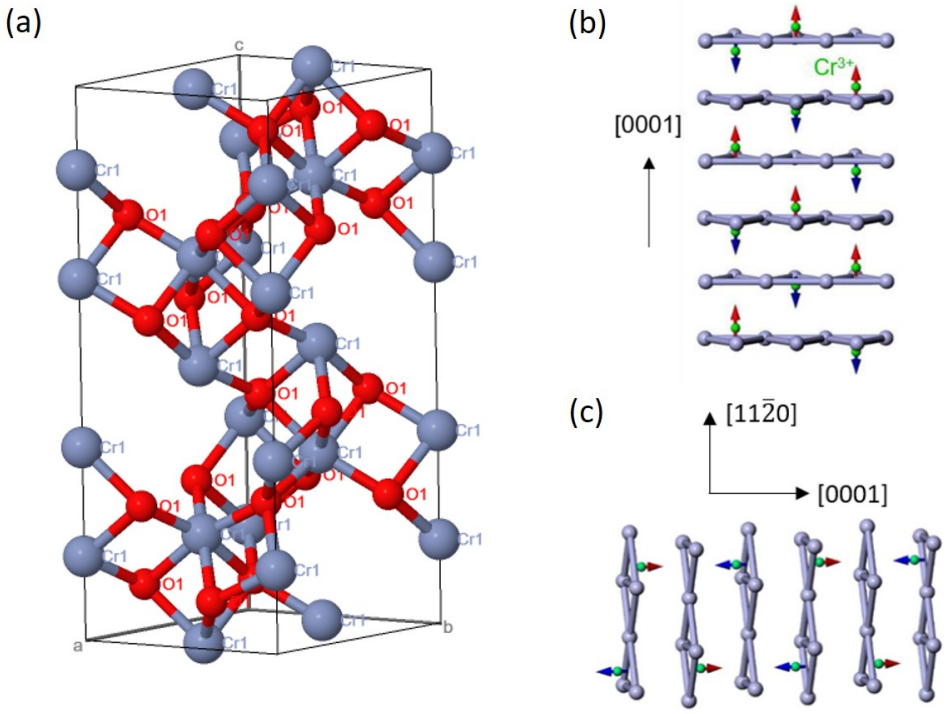

Figure 4.7: Crystal structure and spin orientation of Cr_2O_3. (a) Schematic diagram of Cr_2O_3 unit cell. (b) and (c) Illustration of Cr_2O_3 spin structure from different views

As shown in Figure 4.7, Cr_2O_3 has hexagonal lattice with lattice parameter a = 4.96 Å and c = 13.6 Å. Six Cr-O-Cr layers are stacked along c axis in one unit cell. In AFM

state, spin-up and spin-down Cr^{3+}s lie alternatively along c axis direction, which each Cr^{3+} carries a spin angular momentum s = 3/2. Thus the [0001] plane of Cr_2O_3 is a uncompensated plane while the $(11\bar{2}1)$ and $(10\bar{1}0)$ planes are compensated. The paramagnetic-antiferromagnetic transition temperature (Neel temperature T_N) of bulk Cr_2O_3 is 307 K.

4.2.2 Lattice Matching between Cr_2O_3 and YIG

To consider the possibility of growing Cr_2O_3 films epitaxially on single crystalline YIG with c axis of Cr_2O_3 in the film plane, here we discuss on the potential matching patterns between Cr_2O_3 and YIG. YIG has cubic lattice with lattice constant a = 12.376 Å. Its (111), (110) and (100) planes would be exposed as hexagonal, rectangle and square patterns respectively as shown in Figure 4.8 (a). On the other side, Cr_2O_3 belongs to hexagonal lattice with lattice parameter a = 4.96 Å and c = 13.6 Å. Its (0001), $(11\bar{2}0)$ and $(10\bar{1}0)$ planes are drawn in Figure 4.8 (b).

We first look at it from symmetry and geometry view. If we choose GGG(111) as substrate having YIG grown epitaxially on it, in the most ideal situation we should only be able to get single crystalline Cr_2O_3 with (0001) orientation on it due to matching between the two hexagonal lattice planes. To grow $(11\bar{2}0)$ or $(10\bar{1}0)$ Cr_2O_3 that has in-plane c axis on YIG, rectangle lattice plane is preferred or maybe necessary. YIG with (100) orientation is not a good choice either. Inevitably we can only get at most twin crystalline Cr_2O_3 on it as the two orientations are identical. So even without estimating the lattice mismatch, growing Cr_2O_3 on YIG (110) is the best option we can try to realize the desired material structure.

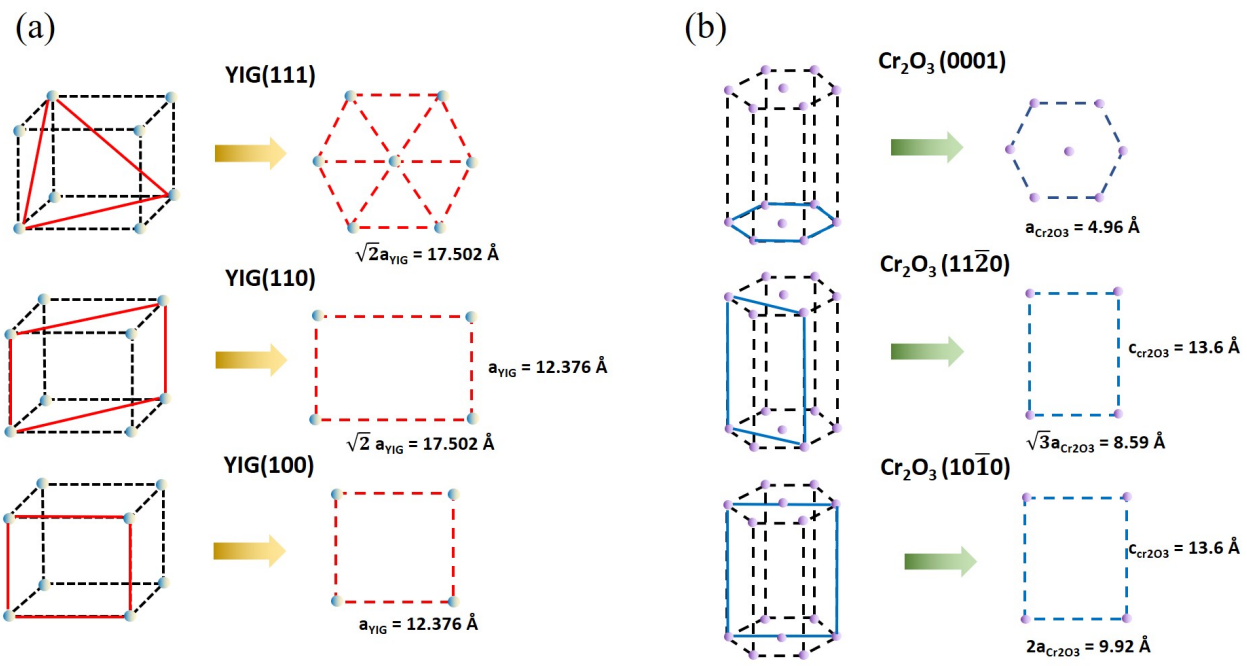

Figure 4.8: Illustration of lattice planes of YIG and Cr_2O_3

4.2.3 Growth of Monolayer Single Crystalline Cr_2O_3 and Polycrystalline Cr_2O_3 on YIG (110)

We grow epitaxial high-quality YIG on GGG (110) substrate via pulsed laser deposition as the first step. Prior to deposition, all substrates underwent standard cleaning process and were baked in high-vacuum PLD chamber at $\sim 220\ C^{\circ}$ for at least three hours. We applied similar recipe as used for TmIG growth described in Chapter 2. The thickness of YIG films is about 15 nm with some small variations. After deposition, the samples were annealed ex-situ with rapid thermal annealing (RTA) at 750 ° for 300 s. The annealed YIG films were well crystallized, ultra smooth and exhibited desired magnetization as shown in Figure 4.9. From the M-H curve (Figure 4.9(d)), we can see that YIG film grown on GGG

(110) has $< 110 >$ as its easy axis and $< 001 >$ as the hard axis.

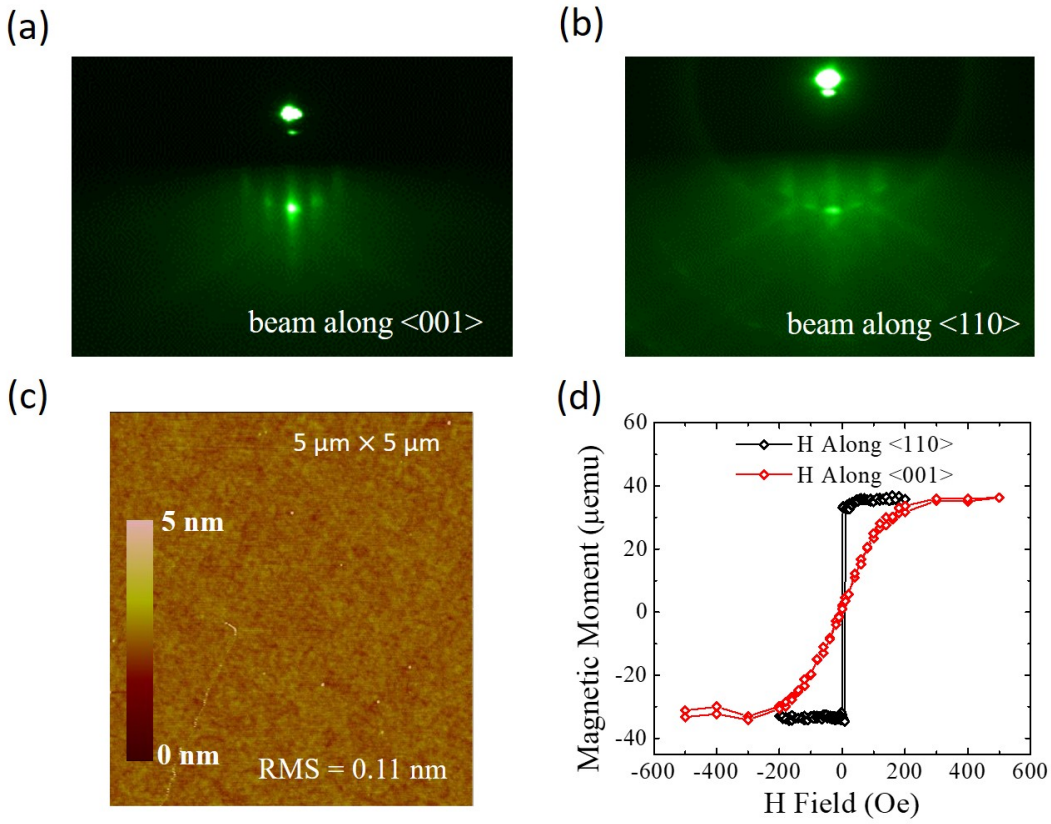

Figure 4.9: Characterization of YIG grown on GGG (110). (a), (b) RHEED pattern of YIG film with beam along $< 001 >$ and $< 110 >$ direction. (c) AFM image of the YIG surface. Root-mean- square (RMS) roughness is 0.11 nm indicating it is ultra flat. (d) M-H curve measured with VSM. Easy-axis behavior shows up when field is along $< 110 >$ direction while $< 001 >$ direction is hard axis.

Cr_2O_3 was then grown on the annealed and cleaned YIG films with PLD. In our experiments on about 70 samples from growth, characterization to device fabrication and SSE measurement, we found that the condition window to obtain good-quality Cr_2O_3 is very narrow. The main factors we identified that have significant influence on the quality of Cr_2O_3 is summarized in Figure 4.10. We shall discuss them in details later relying on

RHEED pattern and surface morphology from AFM as primary metrics. Besides these conditions, we have been conducting the growth of Cr_2O_3 under a ozone pressure 1.5 mTorr and introducing 7 sccm of oxygen gas flow during the RTA annealing.

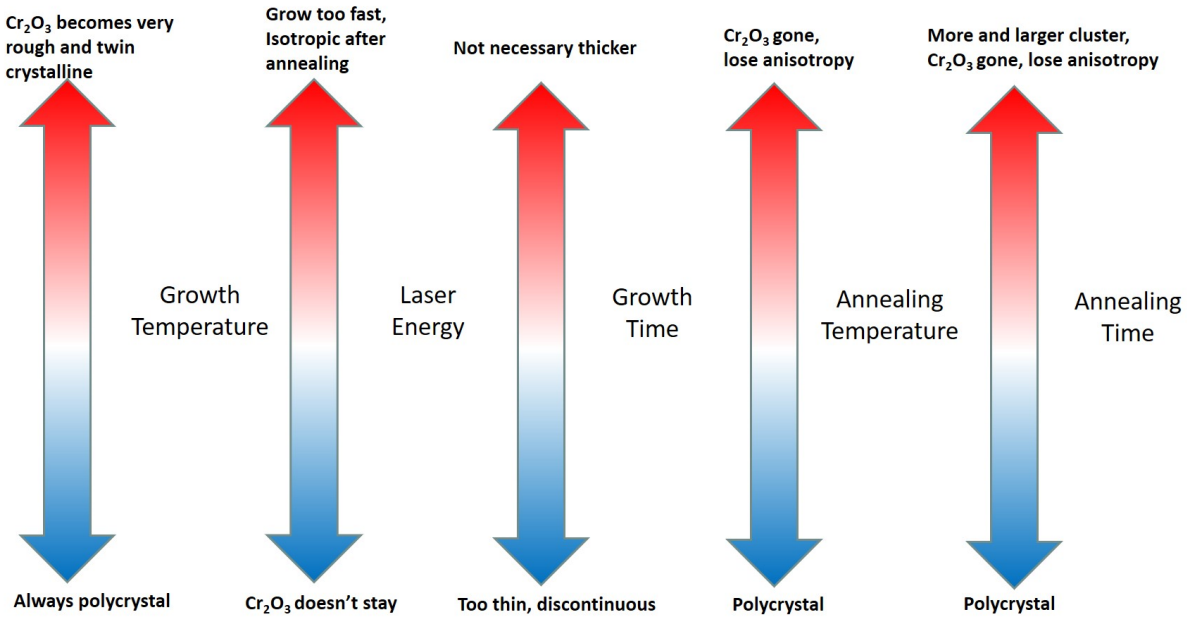

Figure 4.10: Summary of identified key factors that influence Cr_2O_3 growth on YIG (110).

We first examine the effect of growth temperature which is applied on the substrate during Cr_2O_3 growth. We keep the laser energy at the same level which results in a relatively gentle $5 - 10nm/hr$ growth rate of normal oxides at low temperature ($\sim 220\ C^\circ$). With RHEED and atomic force microscopy characterization on the as-grown films, we found that neither too low ($< 300\ C^\circ$) nor too high ($> 650\ C^\circ$) growth temperature gave Cr_2O_3 with satisfying quality. With low growth temperature at $\sim 220\ C^\circ$, the as-grown Cr_2O_3 films have a roughness about six times as high as that of the bottom YIG and no RHEED pattern can be observed (Figure 4.11 (a)). We also found the low-temperature-grown Cr_2O_3 can only be polycrystalline no matter what post annealing condition was applied. However,

too high growth temperature does not produce good quality of Cr_2O_3 film either as shown in Figure 4.11 (c). The RHEED result shows highly complex twin crystalline pattern and the atomic force microscopy image also displays very rough surface with nested clusters. The optimal growth temperature window we identified is between 400 C° to 500 C°, which produces flat surface and relatively organized crystalline structure indicated by the blur RHEED pattern that can be improved by post annealing (Figure 4.11 (b)).

The next two important factors to be discussed about are annealing temperature and time in the post annealing step. First, it was found that Cr_2O_3 grown at 450 C° had different crystalline quality after being post annealed at temperature from 575 C° to 750 C° by tracking RHEED patterns (Figure 4-12 (a)). Annealing temperature above 700 C° is preferred for observation of clearer RHEED patterns, which is confirmed in many other samples. In the previous report, Cr_2O_3 was also annealed at 800 C° for 30 mins [93]. On the other hand, it was also found that Cr_2O_3 hardly stays on YIG (110) as a smooth thin film during long time annealing at high temperature. As shown in Figures 4.12 (b) and (c), after being annealed for a long time or at high temperature, Cr_2O_3 films become much rougher due to formation of clusters, which results in the exposure of YIG surface. When we deposit Pt on such samples and measure SSE, the signal is dominated by the exposed YIG areas and the role of Cr_2O_3 can hardly be distinguished. However, from the feedback of transport measurement result and transmission electron microscopy (TEM), the necessary annealing temperature and time fall into the narrow window. For the purpose of getting epitaxial single crystalline Cr_2O_3 thin films on YIG (110) as primary goal, in our limited experiments we had to deal with randomness and significant variations from sample

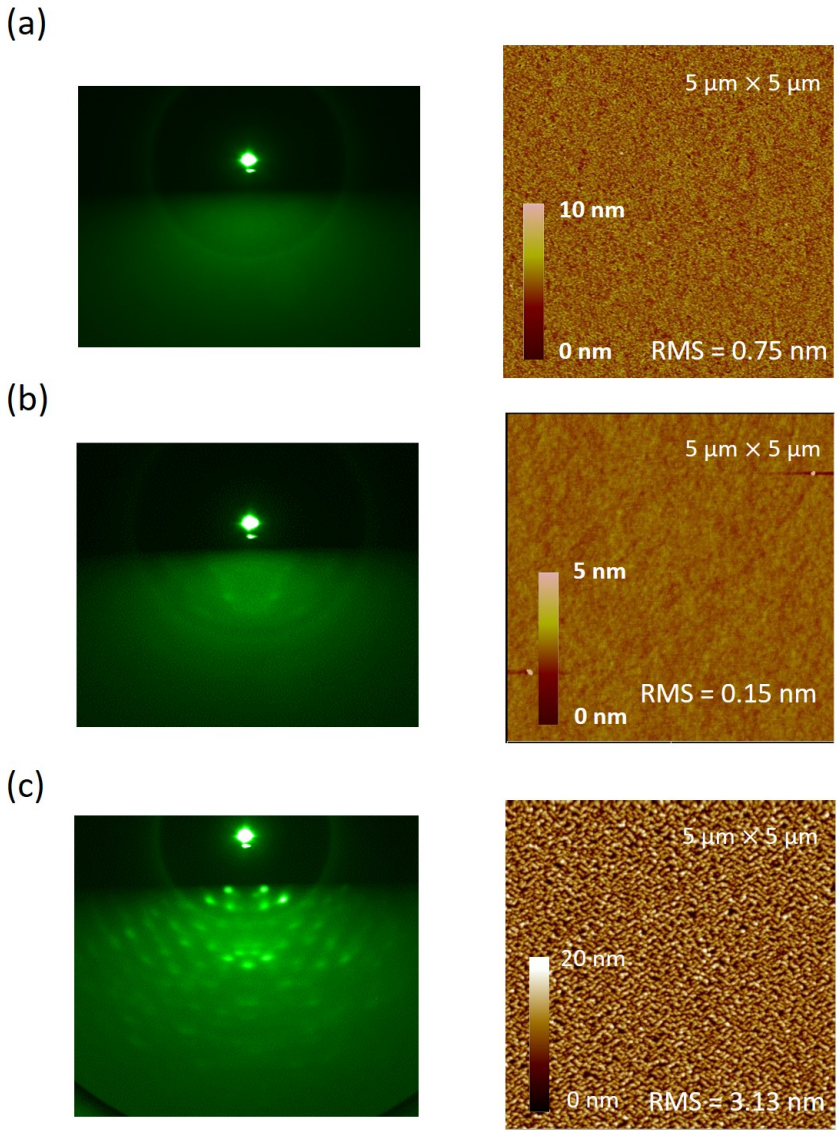

Figure 4.11: RHEED pattern and AFM image of as-grown Cr_2O_3 films from different growth temperature. (a) Cr_2O_3 grown at $\sim$ 220 C°. (b) Cr_2O_3 grown at $\sim$ 450 C°. (c) Cr_2O_3 grown at $\sim$ 700 C°.

to sample.

Finally, I want to comment on the factors of laser energy and growth time. Due to the large lattice mismatch resulted in an energy barrier, when grown at relatively high

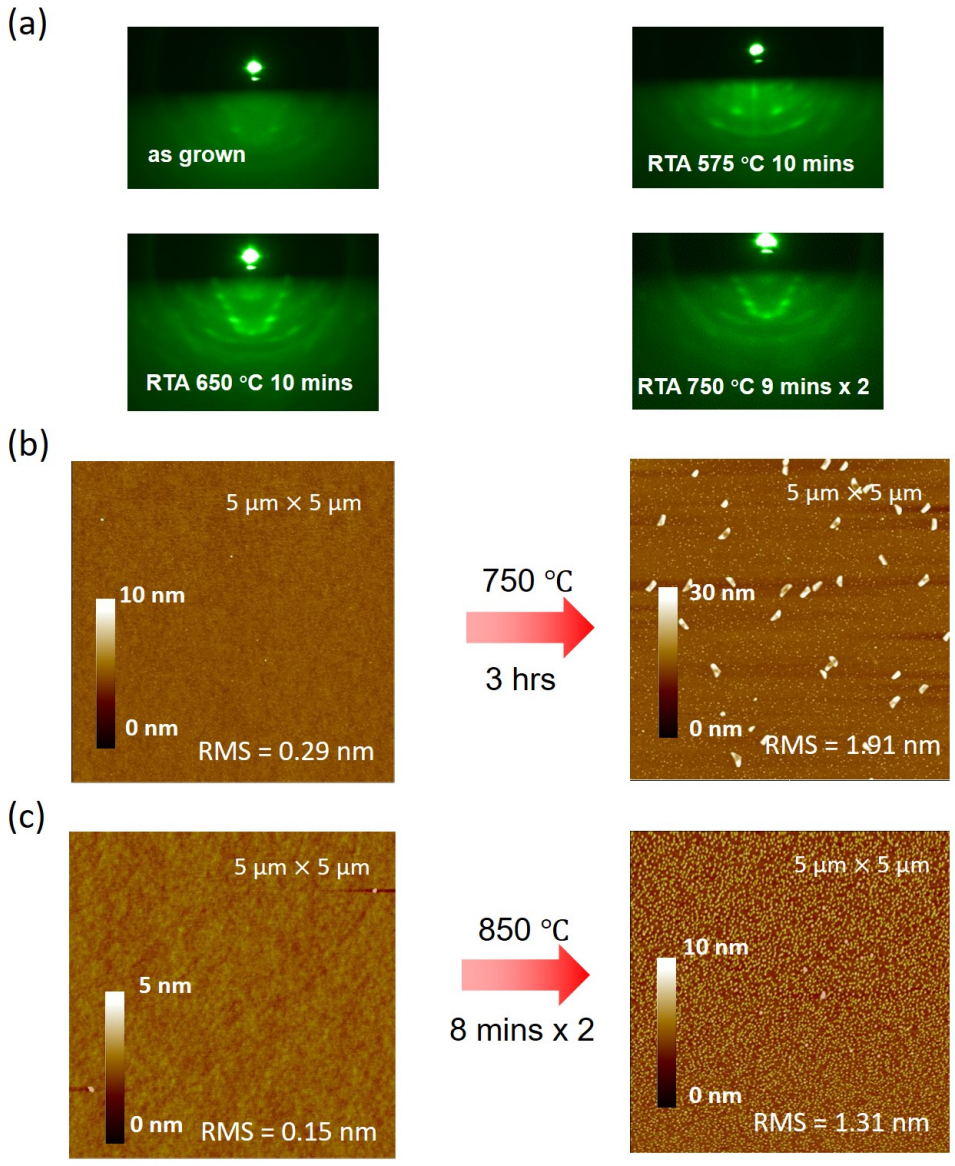

Figure 4.12: Influence of post annealing on Cr_2O_3 captured by RHEED and AFM. (a) Evolution of RHEED pattern from the same Cr_2O_3 sample after multi post annealing. The sample was initially grown at 450 $C°$. (b) and (c) Change of surface morphology before and after post annealing measured by AFM. In all annealing conditions, "8 mins x 2" means that two times of annealing is applied and each time annealing time is 8 mins. So is "9 mins x 2" in (a). This is due to the limitation of RTA facility's maximum running time at high temperature.

temperature ($> 400\ C^{\circ}$) Cr_2O_3 hardly sticks to the YIG (110) surface, which is indicated by the extremely slow growth rate compared to other oxides frequently grown in our lab. To resolve this issue, one option is to decrease the growth temperature. But if growth temperature is decreased too much, it inevitably affects the initial crystal quality of Cr_2O_3 which can not be improved by post annealing. Another choice is to increase the laser power, striking out more material plasma in unit time meanwhile giving it larger kinetic energy. This approach has enabled us to avoid formation of exposed YIG when Cr_2O_3 clusters are formed. Meanwhile we get better control over Cr_2O_3 thickness by growth time. But within the limited number of samples we have tried, the Cr_2O_3 films are only polycrystalline. Nevertheless, it is still possible to get better crystalline condition back by increasing growth temperature while using high laser energy.

After discussing about the critical parameters in the growth of Cr_2O_3 films, now let's focus on some of the typical good samples we have obtained and identified by SSE measurement. Figure 4.13 presents the transmission electron microscopy (TEM) and Energy-dispersive X-ray spectroscopy (EDS) images of a monolayer single crystalline Cr_2O_3 grown on YIG (110). As shown in Figure 4.13 (a), the sample is a fabricated SSE device and the materials from left to right are GGG, YIG, Cr_2O_3, Pt and Al_2O_3. Just between the YIG region and Pt region, there is a continuous layer of Cr_2O_3 atom pairs with very sharp interface, which we call monolayer Cr_2O_3. This is confirmed by the EDS image (Figure 4.13 (b)) that between the YIG and Pt, one layer of material containing Cr element is there which is the Cr_2O_3. Carefully examining at the Cr_2O_3 layer in Figure 4.13 (a), we can see that the atom pairs lie in the same orientation that is single crystalline. Due to the fact that

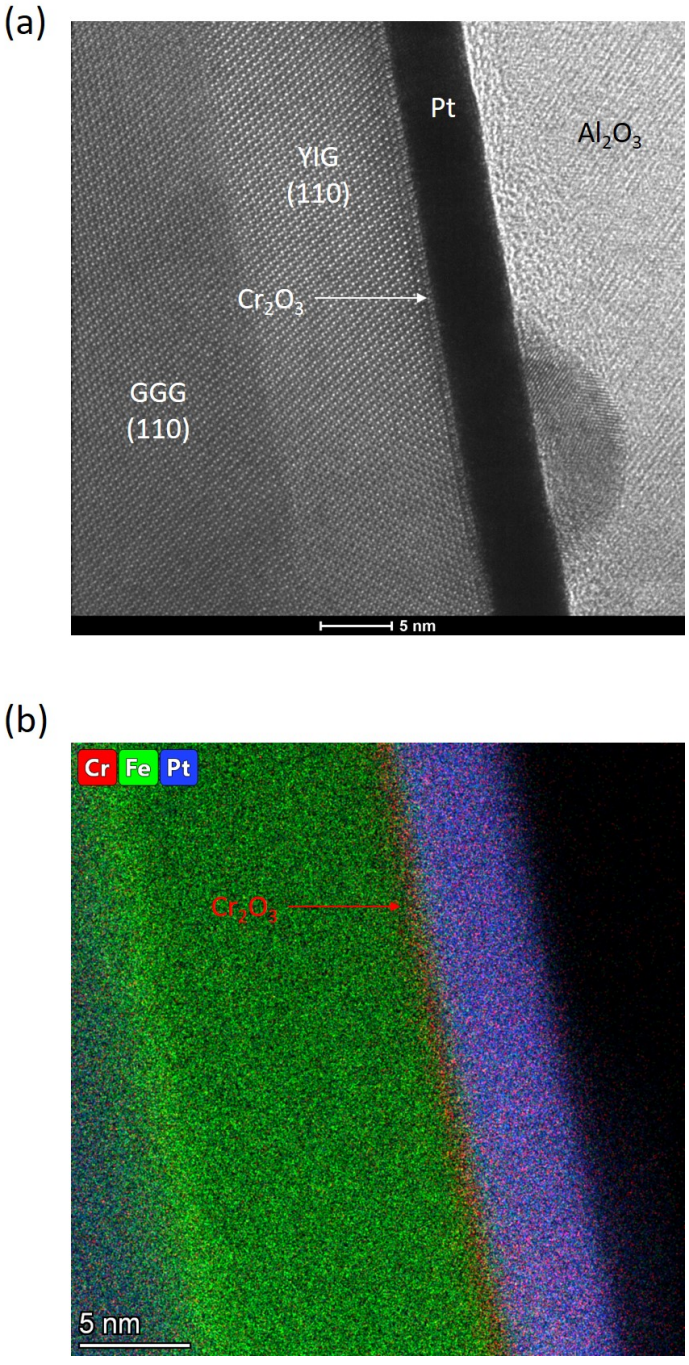

Figure 4.13: TEM and EDS image of monolayer Cr_2O_3 grown on YIG (110). (a) High-resolution TEM image of GGG(110)/YIG/Cr_2O_3/Pt/Al_2O_3. Monolayer of Cr_2O_3 that has one pair of atoms lie in between YIG and Pt with very sharp interface. (b) EDS image confirms that the very thin layer is Cr_2O_3.

we were targeting at 5 nm when we grew Cr_2O_3 and it nearly impossible that the growth just terminated naturally after one monolayer, we believe the formation of this monolayer should come from the annealing process that just one layer of Cr_2O_3 can stay on YIG (110) surface relatively stably.

We also conducted TEM and EDS characterization on relatively thick polycrystalline Cr_2O_3, which is indicated by the RHEED pattern and AFM image (Figure 4.14 (a), (b)). As shown in Figure 4.14 (c), on top of single crystalline epitaxial YIG, there is a continuous Cr_2O_3 layer with average thickness about 12 nm confirmed by the EDS image in Figure 4.14 (d). Cr_2O_3 forms a polycrystalline film with random orientations in different grains. In the area where we performed high-resolution TEM, no preferred orientation can be found in the polycrystalline Cr_2O_3.

Besides the monolayer single crystalline Cr_2O_3 and the thick polycrystalline ones, we could infer from the SSE results that a mixture of monolayer regions and thick regions were formed during the annealing process. And Cr_2O_3 in both regions is polycrystalline. The TEM and EDS images (Figure 4.15) confirmed their coexistence. As shown in Figure 4.15 (a), Cr_2O_3 indicated by red color appears both as monolayer at the blue-yellow (YIG-Pt) interface and as thicker film ($\sim$ 10 nm) in other region. Figure 4.15s (b) and (c) then show their crystalline condition. The lattice orientations of Cr_2O_3 in both regions appear to be random in different areas, which is consistent with the observed polycrystalline ring pattern in RHEED. This also supports our assumption that Cr_2O_3 grown under certain conditions could form monolayer an entire during post annealing.

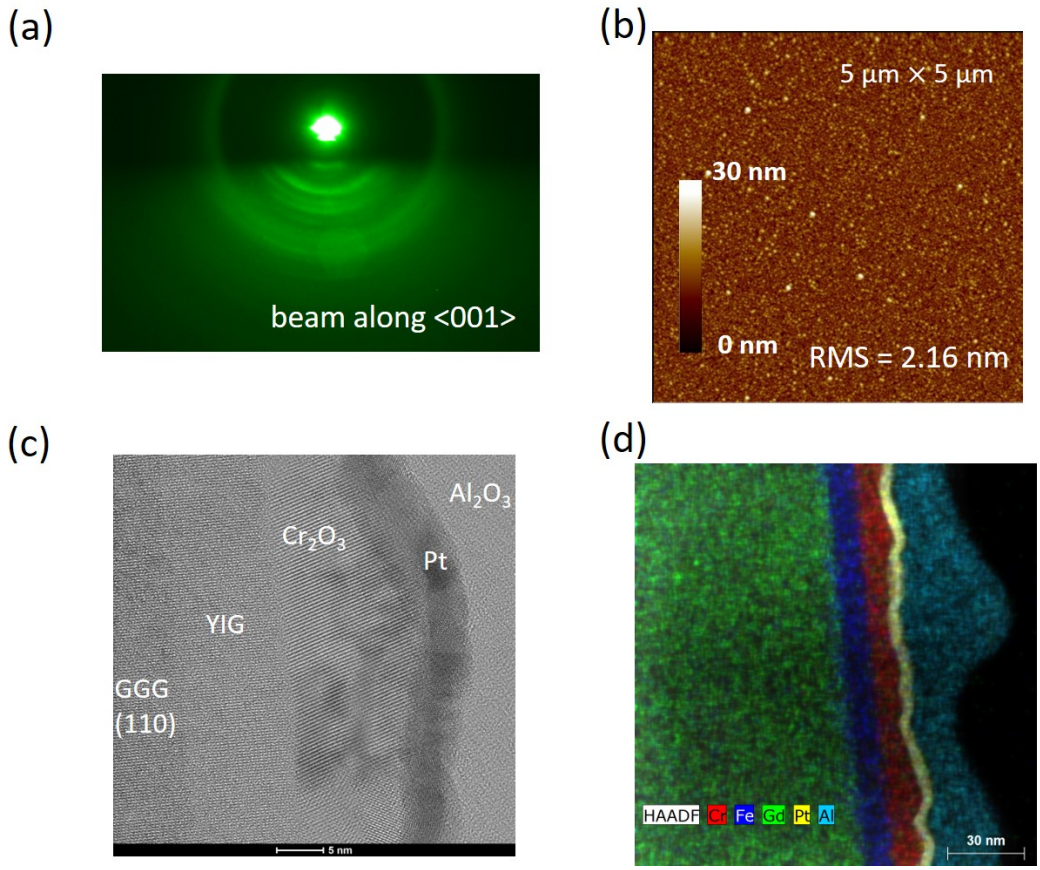

Figure 4.14: RHEED, AFM, TEM and EDS image of thick polycrystalline Cr_2O_3 grown on YIG (110). (a) The ring pattern in RHEED indicates the Cr_2O_3 is polycrystalline. (b) AFM image shows that Cr_2O_3 is rough but basically covers the surface. (c) High-resolution TEM image of the heterostructure. YIG is single crystalline with sharp interfaces but the Cr_2O_3 on top is rather rough. Different Cr_2O_3 grain region has random orientation. (d) EDS image confirms the existence of each layer.

4.3 Spin Seebeck Effect in YIG/Cr_2O_3/Pt

4.3.1 Spin Seebeck Device and Measurement

After the PLD growth of YIG and Cr_2O_3 thin films followed by annealing after each layer, we then deposited 5 nm of Pt on the GGG(110)/YIG/Cr_2O_3 samples using an AJA sputtering system and performed device fabrication. We first performed standard

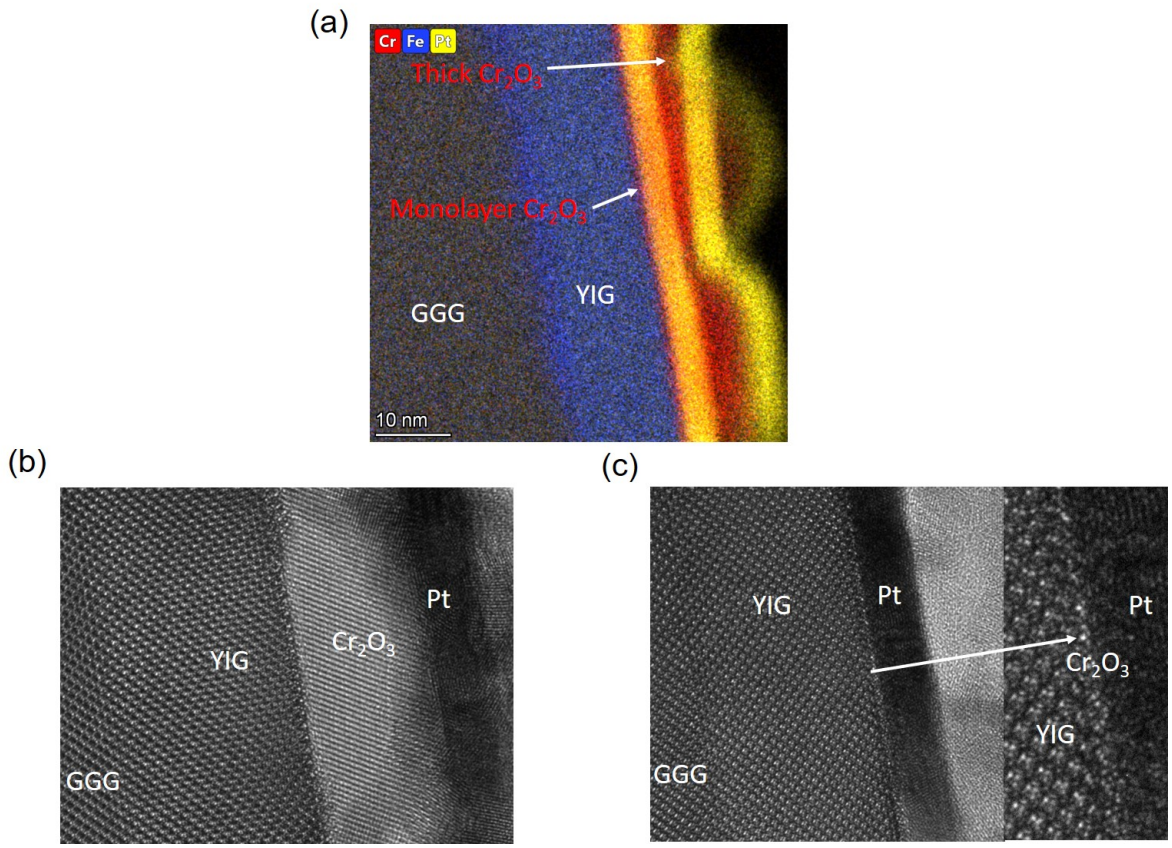

Figure 4.15: EDS and TEM images of Cr_2O_3 with mixed thickness. (a) EDS image of YIG/Cr_2O_3/Pt that shows the co-existence of monolayer and thick Cr_2O_3. Due to the finite thickness of the sample foil ($\sim$ 50 nm), we can see projections from different layers, which some have monolayer Cr_2O_3 and some have thick one. Two layers of Pt are present due to the projections from different z positions. (b) TEM image of one region with thick Cr_2O_3. (c) A area where there is monolayer Cr_2O_3 in between YIG and Pt. The right part is a zoom-in of the interface.

photolithography process to write photoresist pattern on the Pt layer, and then did etching with inductively coupled plasma (ICP) to get pattern. After cleaning, the samples are deposited with a 50 nm Al_2O_3 layer by atomic layer deposition (ALD). Then we performed photolithography again and deposited 30 nm Cr/5 nm Au with an e-beam evaporator afterwards to make the on-chip top heater. We had used two shapes of SSE devices as shown in Figure 4.16. In both types of devices, the light gray part is the bottom Pt detector

and the dark part is the top Cr/Au heater. The two parts are well insulated from each other by the Al_2O_3 layer and their overlapping region is where the heat is generated and conducted to the bottom YIG/Cr_2O_3. The distance between the two outer Pt electrodes is 3.5 mm.

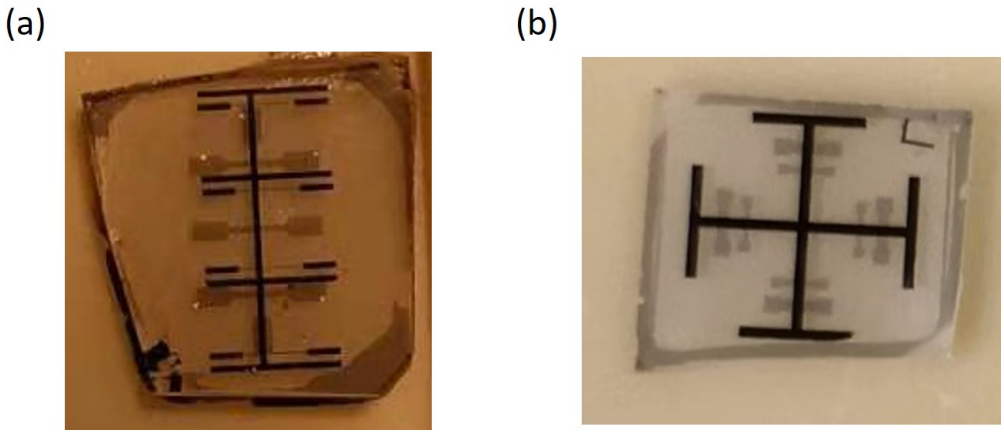

Figure 4.16: Pictures of SSE devices. In our experiments, we have been making SSE devices with two shapes. We call (a) Hall-bar shape and (b) cross shape

The samples were measured in Quantum Design's DynaCool Physical Property Measurement System (PPMS) and Janis's 4 K Closed Cycle System down to a temperature of 4 K. In the measurement, we used a Keithley 6221 as AC source meter to apply an AC current with a constant amplitude in the Cr/Au heater, a Keithley 2000 to measure the AC voltage on the heater, and SR830 locked-in amplifiers combined with SR560 preamplifiers to detect the inverse spin Hall effect (ISHE) voltage in the Pt channel. We typically set the frequency of heating current at 17 Hz, then measured the 2ω SSE signal at 34 Hz. The signals were amplified by 1000 times with the SR560 preamplifier.

In SSE measurements, one important factor that people have to pay attention to is the sample's actual temperature. This is because when intense heating is applied, the actual

sample temperature can differ from the system temperature reported by the thermometer. To address this issue, we performed the temperature difference calibration using the Pt channel as a thermometer to measure the actual sample temperature. We first measured a Pt resistance (R) vs. system read temperature (T) curve with heater off, in which case the system temperature can be relied on(black plots in Figure 4.17). We can see that R changes linearly with decreasing T with a finite slop, stays flat once temperature is below 20 K, and starts to rise when T is below 7 K. In the region with red data points, we first set the system temperature at 1.6 K, then started to apply a heating current. Due to the heat generated from the heater, the PPMS system could not reach the set temperature 1.6 K anymore but ended up at a higher temperature in the reading. We repeated this for different heating currents. Another Pt resistance vs. T curve by connecting those red points can be obtained as heating current varies. Finally, the difference between system read temperature and the sample's actual temperature when heater is turned on can be extracted as shown in Figure 4.17 (b) by finding the corresponding point with the same R. In the low temperature region ($< 20K$), when a heating power of 13.2 mW is applied, there is a temperature difference about 6 K between the system temperature and actual sample temperature. Note that this heating power is already relatively large in our measurements. The thermal conductivity of the materials as well as cooling power are small in the low temperature region, which results in a relatively large difference. When temperature is higher above 20 K, the difference between the system read and sample's actual temperature becomes much smaller and negligible. Another issue people often have arguments about in SSE measurements is the proper way of doing normalization so that inverse spin Hall

voltages at different temperature can be fairly compared [112]. In our data processing, we normalize the measured ISHE voltage by heating power. And this value should be proportional to the conversion ratio of heat current to spin current [51].

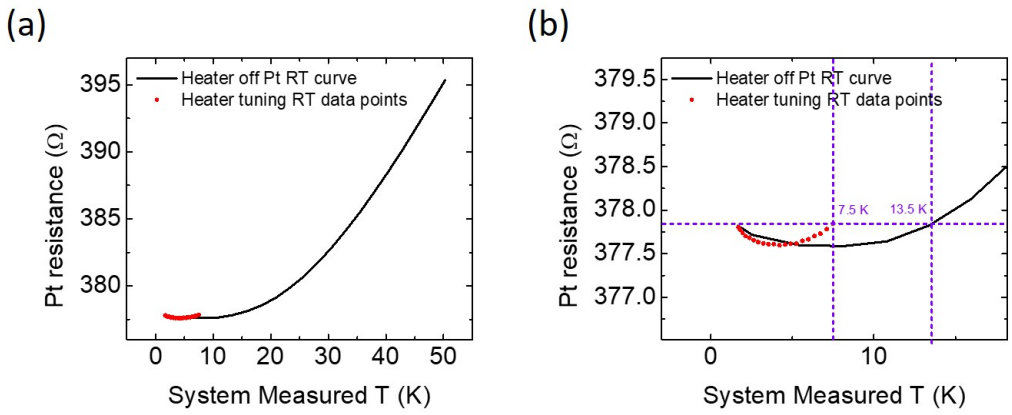

Figure 4.17: Temperature difference calibration in SSE measurement. Pt resistance vs. system read temperature curve for entire temperature range (a) and low temperature range (b). In the most right red data point, a heating power 13.2 mW was applied. The difference between system read temperature and sample's real temperature is estimated to be 6 K in that condition.

4.3.2 Spin Seebeck in Monolayer Single Crystalline Cr_2O_3

Before we discuss about SSE in YIG(110)/Cr_2O_3/Pt, let's first look at SSE in standard YIG/Pt devices. In all our measurement setups, ISHE voltage is measured along +x direction, magnetic field H is applied along +y direction, and their cross product points to the $-\nabla T$ direction. As shown in Figure 4.18 (a), at 300 K, SSE vs. H curve exhibits a sharp hysteresis loop when field is along $< 110 >$ direction which is the easy axis of YIG. A hard-axis behavior shows up if field is swept along $< 001 >$ direction. In our experiment, we noticed that the 2ω SSE signals from y channel of the lock-in amplifier had an opposite

sign to the loops measured with DC method. Nevertheless the sign and magnitude were consistent in all AC measurements regardless of the heating current frequency. We defined that loops with the orientation shown in Figure 4.18 (a) have positive sign. When we varied temperature, SSE vs. T curves show basically the same behavior in the two perpendicular orientations (Figure 4.18 (b)) and are consistent with the results from other groups [93].

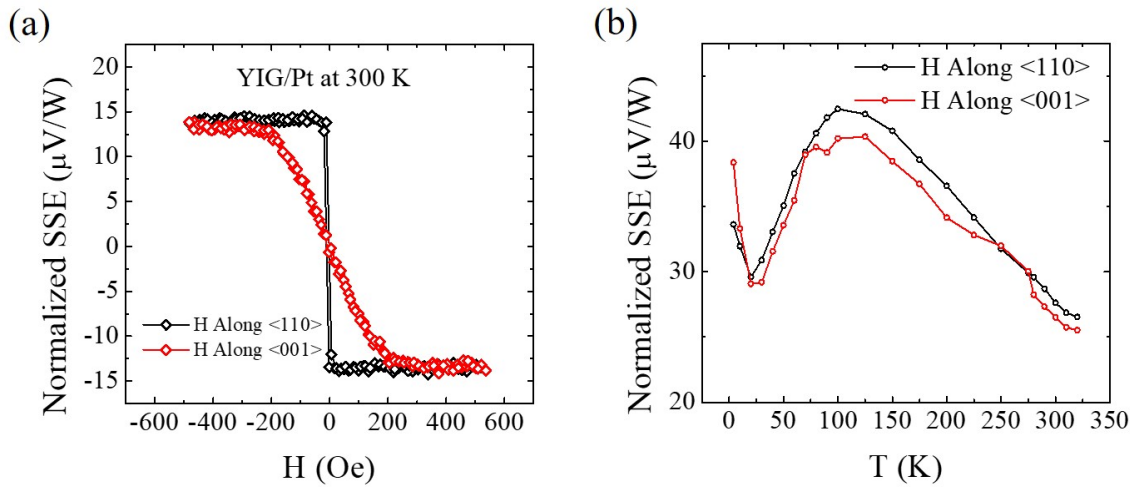

Figure 4.18: SSE signal in standard YIG/Pt device. (a) SSE vs. H curve shows easy-axis behavior with H along $< 110 >$ direction and hard-axis behavior when field is along $< 001 >$. (b) While there being small discrepancy, temperature dependence of SSE in two orientations shows basically the same behavior and keeps the same sign.

For SSE in YIG(110)/Cr_2O_3/Pt devices, let's begin with one sample with mono-layer single crystalline Cr_2O_3 that was later characterized and confirmed with TEM as shown in Figure 4.13. When we applied magnetic field along $< 110 >$ direction which is the easy axis of YIG and measured the SSE signal at different temperatures, it was surprisingly found that the SSE hysteresis loop flips orientation at around 60 K, which means SSE signal changes sign. Figure 4.19 (a) shows the SSE hysteresis loops in the entire temperature range and (b) shows the evolution of the loop with more temperature points near the

sign change temperature. When we measured SSE in the perpendicular channel with field also rotated by 90 degree which now is along the $< 001 >$ direction, it was observed that in similar temperature range ($< 60K$) where SSE sign reverses in previous orientation, it shows a shut off in SSE signal now as shown in Figures 4.19 (c) and (d). We extracted the SSE signal at different temperature in these two field orientations, and plotted in Figure 4.20. The unique behaviors in the two orthogonal field directions can be clearly recognized. Notice that (c) and (d) have much smaller signals compared to (a) and (b). This is because in the field along $< 001 >$ case, we had to measure the signals across a very short channel that is just about 1/20 of the length in the other orientation. In Figure 4.20, data points in the red curve are multiplied by a constant factor in order to align the two curves at 300 K so that they are comparable.

It is important to develop a comprehensive understanding of this behavior and its physical origin. As shown in the top panel of Figure 4.21, when the applied magnetic field points up, the right-handed magnon with polarization downwards is populated in the FMI layer. When an AFMI layer is inserted between the FMI and HM layer, however, the right-handed magnon should not simply flip the orientation after transmitting through the AFMI layer. In a recent paper published by Cheng et al. [12], it was proposed that in the FMI/AFMI/FMI heterostructure, the strong exchange coupling between the left FMI and middle AFMI plays a significant role. When the AFMI Neel vector is along the H direction so as the M of YIG, an imbalance in its two AFM modes will be introduced by the exchange field at interface. The preferred mode then owns the polarization with direction same as the magnetic field as shown in the bottom panel of Figure 4.21. In our FMI/AFMI/HM

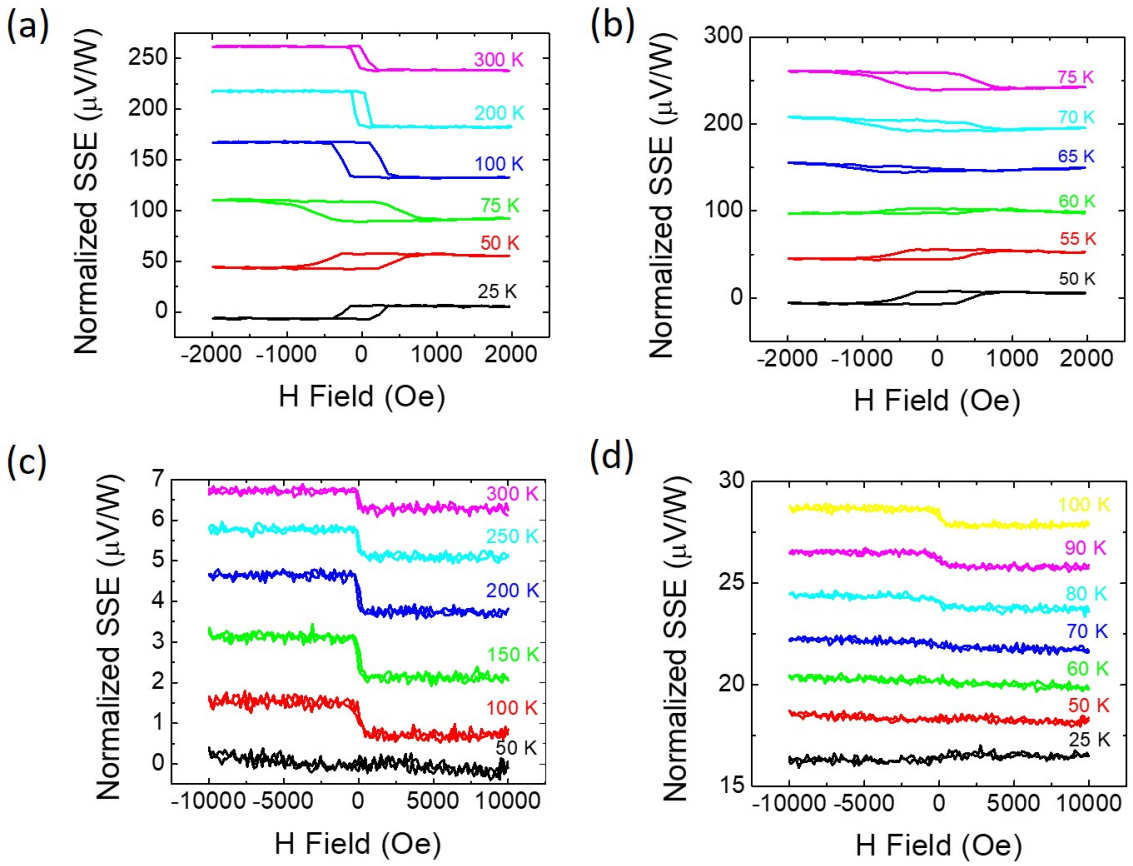

Figure 4.19: Illustration of sign reversal and shut off of SSE in monolayer single crystalline YIG(110)/Cr_2O_3/Pt. (a) and (b) shows the sign change of SSE at around 60 K when magnetic field is applied along $< 110 >$ direction. (c) and (d) shows the shut off of SSE signal when field is applied along $< 001 >$ direction

SSE device, when a thermal gradient is applied, this branch of AFM magnon is populated and gives rise to the ISHE signal in the right HM layer. As for the right-handed magnon populated in the FM layer that has polarization opposite to the magnetic field, however, due to the large energy gap between FM and AFM magnons, it will be blocked at the interface. Coming back to our situation of YIG(110)/Cr_2O_3/Pt heterostructure, we propose the following explanation: The field orientation in which SSE reverses sign is the Neel vector direction. When measurement is performed in that geometry, the right-handed FM

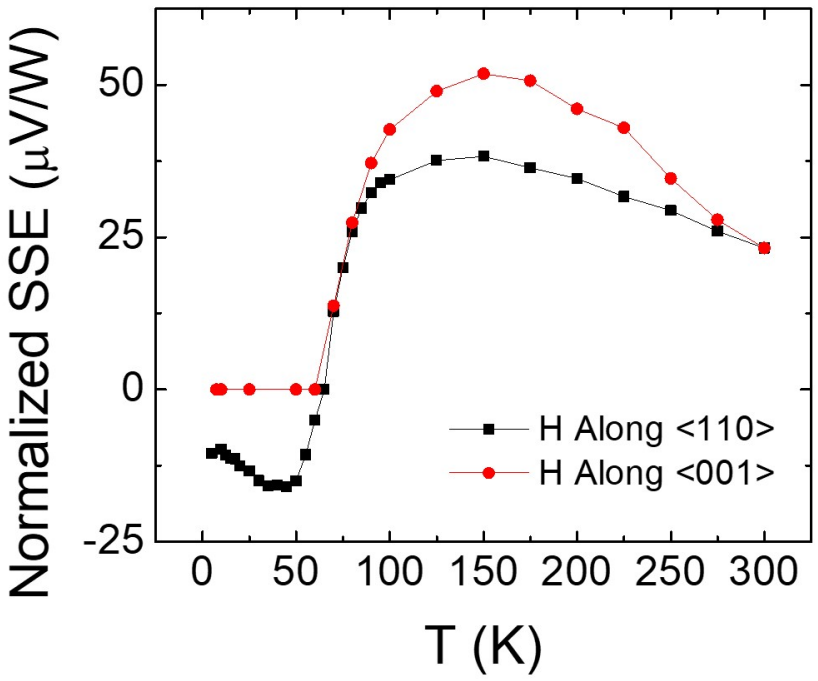

Figure 4.20: Temperature dependence of SSE in monolayer single crystalline YIG(110)/Cr_2O_3/Pt with magnetic field from two perpendicular orientations. The red curve is amplified by a factor that aligns the SSE signal from two orientations at 300 K.

magnon from YIG contributes to the SSE signal when it is above monolayer Cr_2O_3's Neel temperature. However, once it is below the Neel temperature and AFM order is established, FM magnons from the YIG start to be blocked at the interface and the induced AFM magnons from Cr_2O_3 that have opposite polarization begin to contribute. When the AFM magnons dominate over the transmitted FM magnons, the measured SSE reverses sign. When the field is applied in the other direction which would be perpendicular to the Neel vector direction, there will be no AFM magnon induced in Cr_2O_3. Meanwhile once Cr_2O_3's Neel order forms and spin fluctuation existing in the paramagnetic state freezes, the FM magnon can not propagate through Cr_2O_3 as explained by [93], resulting in an observed

SSE shut off.

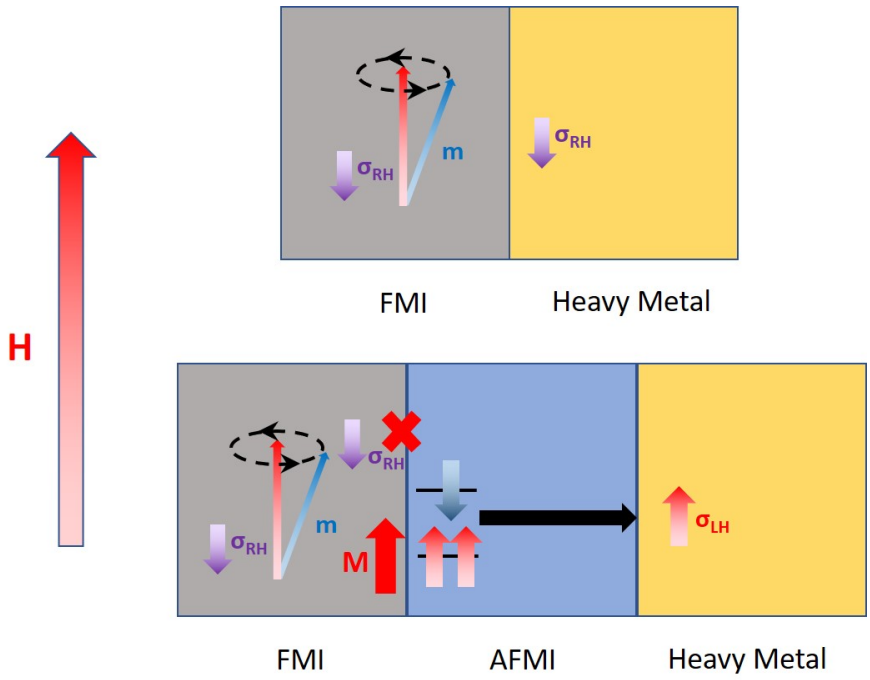

Figure 4.21: Illustration of observed SSE sign reversal in YIG(110)/Cr_2O_3/Pt heterostructure. With magnetic field in the up direction applied, top panel shows the situation in FMI/HM bilayer and the bottom panel illustrates the FMI/AFMI/HM trilayer which the Neel vector of uniaxial AFMI is also in the up-down direction

4.3.3 Spin Seebeck in Thick Polycrystalline Cr_2O_3

While a lot of effort was devoted, we found it extremely hard to grow single crystalline Cr_2O_3 on YIG(110) with controllable thickness and free from pin holes, which has been discussed in the material growth section. So we further conducted our measurements in the samples with polycrystalline Cr_2O_3 to confirm the conclusions from the monolayer Cr_2O_3 case. First, as proposed in the previous section, right-handed magnon contribution gets shut off regardless of its relative orientation. Thus the similar shut off behavior would

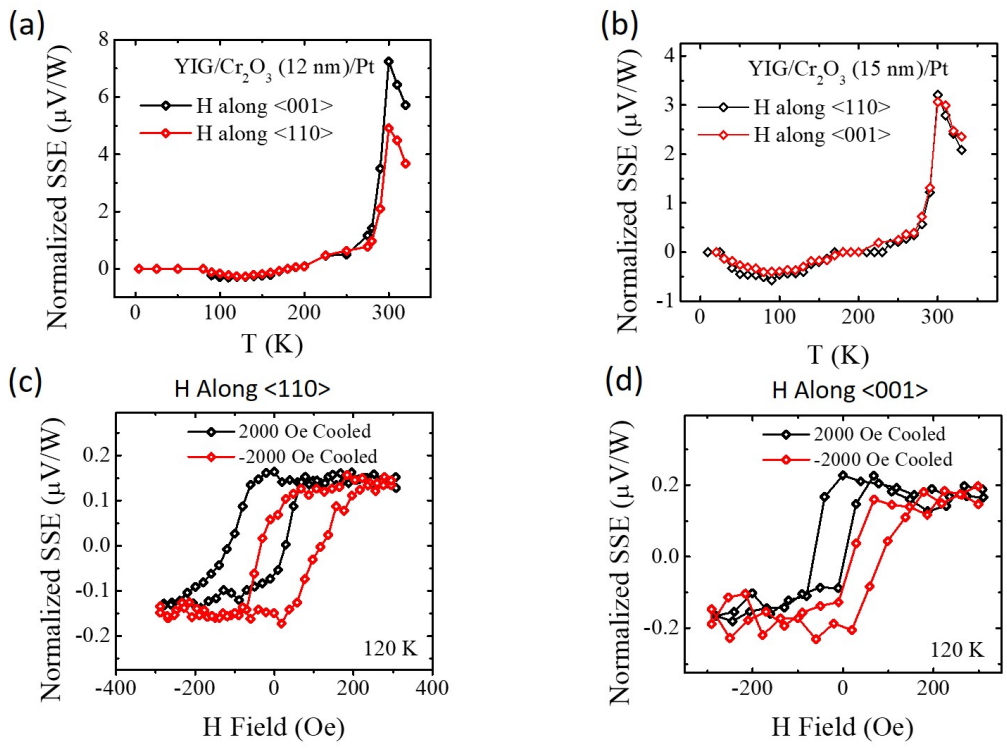

Figure 4.22: Temperature dependence of SSE and illustration of observed exchange bias in thick YIG(110)/Cr_2O_3/Pt. (a) and (b) Temperature dependence of SSE signal in two YIG(110)/Cr_2O_3/Pt which Cr_2O_3 films are thick and polycrystalline. A characteristic phase transition peak at 300 K, shut off of SSE signal below 260 K and later reversed SSE signals are observed. (c) and (d). Observation of exchange bias in YIG(110)/Cr_2O_3/Pt. The sample is the same one as shown in (a). A bias field about 25 Oe is observed in both field orientations.

show up in samples with thicker polycrystalline Cr_2O_3. To think about it intuitively, with c axis randomly distributed, there should always be a number of polycrystalling grains with the of Neel vector parallel to the field direction. Such a component would result in a reversed SSE signal in YIG/ polycrystalline Cr_2O_3/Pt devices. It would be the case for every direction; therefore, the SSE behavior should be isotropic. With this hypothesis, we performed measurements in samples with thicker Cr_2O_3 and the results confirmed our expectation. As shown in Figures 4.22 (a) and (b) for YIG(110)/Cr_2O_3/Pt samples, in which

Cr_2O_3 is about 12 nm and 15 nm respectively, the SSE signals first show a shut off once temperature is below 260 K, then emerge again with a reversed sign in lower temperature range. There are also characteristic peaks observed at 300 K that corresponds to the paramagnetic-antiferromagnetic phase transition that was also reported in [93]. Moreover, in the sample shown in Figure 4.22 (a), we have observed the exchange bias effect. It exists in the entire temperature range where SSE shows a negative signal. Representative SSE vs. H loops measured at 120 K with field in both orientations are shown in Figures 4.22 (c) and (d). The bias field is about 25 Oe. This observation further confirms the well-established antiferromagnetism in our Cr_2O_3 films.

At last, I present results from three samples that show the characteristic peak or bump at 300 K and sign reversal at about 60 K, but no shut off of SSE. As shown in Figure 4.23, we believe there is formation of polycrystalline monolayer Cr_2O_3 in these samples during annealing, which is associated with the sign change temperature of 60 K. Meanwhile there are also thick regions which block spin current thus attenuate the total signal below about 260 K and give the AFM peak at 300 K. But due to the presence of the monolayer part, the overall SSE signal never gets totally shut off as in other thick ones. Nevertheless, this set of results is consistent with the other data and supports our argument that Cr_2O_3 is hard to stay on YIG(110) surface or tends to form monolayer during the high-temperature annealing.

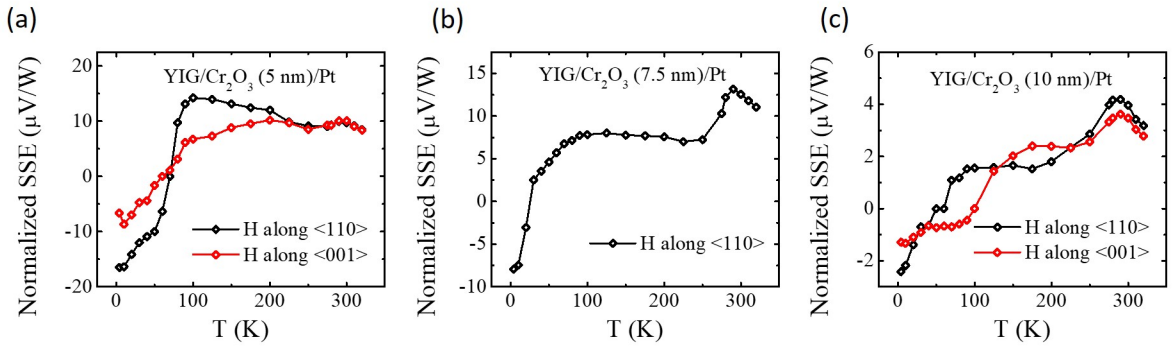

Figure 4.23: Temperature dependence of SSE in YIG(110)/Cr_2O_3/Pt samples with mixed-Cr_2O_3-thickness regions.

Chapter 5

Summary

I would like to have a brief summary for each chapter before the end of my thesis.

In Chapter 1, we first had an overview over the research topics people focus on in spintronics studies. We have a brief introduction to magnetic proximity effect, anomalous Hall effect (AHE), spin Hall effects and spin Seebeck effect (SSE), which are very important phenomena studied in spintronics and are also the focus of my PhD research.

In Chapter 2, we first briefed the structural and magnetic properties of rare earth iron garnets (REIG). Then we demonstrated our capability of growing high-quality REIG thin films with our pulsed laser deposition (PLD) system. The magnetic anisotropy in our REIGs films can be well engineered by design and we successfully got high-quality TmIG films with robust perpendicular magnetic anisotropy (PMA). With good control over the quality, thickness and PMA of the TmIG films, we were able to observe topological Hall effect (THE) at above room temperature in ultra thin TmIG/Pt samples. The observed THE signals are demonstrated to originate from the emergence of magnetic skyrmions at the

interface by comparing phase diagrams from experimental data and theoretical simulations.

In Chapter 3, I presented our work on studying temperature dependence of AHE in TmIG/Pt. We demonstrated the causal relationship between the proximity effect of the TmIG/Pt interface and the AHE in this system by separating the high- and low-filed AHE components. Large AHE magnitude and the sign change in its temperature dependence are observed when Pt is in direct contact with TmIG. The first-principles calculations based on induced ferromagnetism in Pt capture the key features in our experimental observations.

In Chapter 4, I showed our study on spin Seebeck effect in ferromagnetic magnetic insulator (FMI)/antiferromagnetic insulator (AFMI)/Pt heterostructures. Basic physical pictures of ferromagnetic resonance and antiferromagnetic resonance were briefed and compared to better introduce the concept and unique properties of AFM magnon in AFMI. We explored the critical parameters that have significant influence on Cr_2O_3 growth. High-quality Cr_2O_3 thin films grown on YIG (110) were demonstrated. In the transport measurements, we observed a sign change in SSE signal, which indicates the presence of left-handed AFM magnon contribution. The physical mechanism of magnon transmission at the FMI/AFMI interface is also revealed from the shut-off behavior in SSE below when it is below Cr_2O_3's Neel temperature.

Bibliography

[1] Can Onur Avci, Andy Quindeau, Chi-Feng Pai, Maxwell Mann, Lucas Caretta, Astera S. Tang, Mehmet C. Onbasli, Caroline A. Ross, and Geoffrey S. D. Beach. Current-induced switching in a magnetic insulator. *Nature Materials*, 16(3):309–314, 2016.

[2] Sumilan Banerjee, James Rowland, Onur Erten, and Mohit Randeria. Enhanced stability of skyrmions in two-dimensional chiral magnets with rashba spin-orbit coupling. *Phys. Rev. X*, 4:031045, Sep 2014.

[3] Gerrit E. W. Bauer, Eiji Saitoh, and Bart J. van Wees. Spin caloritronics. *Nature Materials*, 11(5):391–399, 2012.

[4] P. E. Blöchl. Projector augmented-wave method. *Phys. Rev. B*, 50:17953–17979, Dec 1994.

[5] Stephen John Blundell. *Magnetism in condensed matter*. Oxford University Press, 2014.

[6] A. Bogdanov and A. Hubert. Thermodynamically stable magnetic vortex states in magnetic crystals. *Journal of Magnetism and Magnetic Materials*, 138(3):255 – 269, 1994.

[7] A. N. Bogdanov and U. K. Rößler. Chiral symmetry breaking in magnetic thin films and multilayers. *Phys. Rev. Lett.*, 87:037203, Jun 2001.

[8] C. Brüne, A. Roth, E. G. Novik, M. König, H. Buhmann, E. M. Hankiewicz, W. Hanke, J. Sinova, and L. W. Molenkamp. Evidence for the ballistic intrinsic spin hall effect in hgte nanostructures. *Nature Physics*, 6(6):448–454, Feb 2010.

[9] C.-Z. Chang, J. Zhang, X. Feng, J. Shen, Z. Zhang, M. Guo, K. Li, Y. Ou, P. Wei, L.-L. Wang, and et al. Experimental observation of the quantum anomalous hall effect in a magnetic topological insulator. *Science*, 340(6129):167–170, 2013.

[10] Cui-Zu Chang, Weiwei Zhao, Duk Y. Kim, Haijun Zhang, Badih A. Assaf, Don Heiman, Shou-Cheng Zhang, Chaoxing Liu, Moses H. W. Chan, Jagadeesh S. Moodera, and et al. High-precision realization of robust quantum anomalous hall state in a hard ferromagnetic topological insulator. *Nature Materials*, 14(5):473–477, Feb 2015.

[11] Yan-Ting Chen, Saburo Takahashi, Hiroyasu Nakayama, Matthias Althammer, Sebastian T. B. Goennenwein, Eiji Saitoh, and Gerrit E. W. Bauer. Theory of spin hall magnetoresistance. *Phys. Rev. B*, 87:144411, Apr 2013.

[12] Ran Cheng, Di Xiao, and Jian-Gang Zhu. Antiferromagnet-based magnonic spin-transfer torque. *Phys. Rev. B*, 98:020408, Jul 2018.

[13] Ran Cheng, Jiang Xiao, Qian Niu, and Arne Brataas. Spin pumping and spin-transfer torques in antiferromagnets. *Phys. Rev. Lett.*, 113:057601, Jul 2014.

[14] Jaehun Cho, Nam-Hui Kim, Sukmock Lee, June-Seo Kim, Reinoud Lavrijsen, Aurelie Solignac, Yuxiang Yin, Dong-Soo Han, Niels J. J. van Hoof, Henk J. M. Swagten, Bert Koopmans, and Chun-Yeol You. Thickness dependence of the interfacial dzyaloshinskii-moriya interaction in inversion symmetry broken systems. *Nature Communications*, 6(1):7635, 2015.

[15] L. J. Cornelissen, J. Liu, R. A. Duine, J. Ben Youssef, and B. J. van Wees. Long-distance transport of magnon spin information in a magnetic insulator at room temperature. *Nature Physics*, 11:1022 EP –, Sep 2015.

[16] Bertrand Dupé, Markus Hoffmann, Charles Paillard, and Stefan Heinze. Tailoring magnetic skyrmions in ultra-thin transition metal films. *Nature Communications*, 5(1):4030, 2014.

[17] M. I. D'Yakonov and V. I. Perel'. Possibility of Orienting Electron Spins with Current. *Soviet Journal of Experimental and Theoretical Physics Letters*, 13:467, Jun 1971.

[18] Satoru Emori, Uwe Bauer, Sung-Min Ahn, Eduardo Martinez, and Geoffrey S. D. Beach. Current-driven dynamics of chiral ferromagnetic domain walls. *Nature Materials*, 12:611 EP –, Jun 2013.

[19] Albert Fert, Vincent Cros, and João Sampaio. Skyrmions on the track. *Nature Nanotechnology*, 8(3):152–156, 2013.

[20] O. Gomonay, V. Baltz, A. Brataas, and Y. Tserkovnyak. Antiferromagnetic spin textures and dynamics. *Nature Physics*, 14(3):213–216, 2018.

[21] M. Hagiwara, K. Katsumata, H. Yamaguchi, M. Tokunaga, I. Yamada, M. Gross, and P. Goy. A complete frequency-field chart for the antiferromagnetic resonance in mnf2. *International Journal of Infrared and Millimeter Waves*, 20(4):617–622, Apr 1999.

[22] D. M. Heinz, P. J. Besser, J. M. Owens, J. E. Mee, and G. R. Pulliam. Mobile cylindrical magnetic domains in epitaxial garnet films. *Journal of Applied Physics*, 42(4):1243–1251, 1971.

[23] Stefan Heinze, Kirsten von Bergmann, Matthias Menzel, Jens Brede, André Kubetzka, Roland Wiesendanger, Gustav Bihlmayer, and Stefan Blügel. Spontaneous atomic-scale magnetic skyrmion lattice in two dimensions. *Nature Physics*, 7(9):713–718, 2011.

[24] J. E. Hirsch. Spin hall effect. *Phys. Rev. Lett.*, 83:1834–1837, Aug 1999.

[25] Y. S. Hor, P. Roushan, H. Beidenkopf, J. Seo, D. Qu, J. G. Checkelsky, L. A. Wray, D. Hsieh, Y. Xia, S.-Y. Xu, and et al. Development of ferromagnetism in the doped topological insulator $Bi_{2-x}Mn_xTe_3$. *Physical Review B*, 81(19), Jun 2010.

[26] Dazhi Hou, Zhiyong Qiu, Joseph Barker, Koji Sato, Kei Yamamoto, Saül Vélez, Juan M. Gomez-Perez, Luis E. Hueso, Fèlix Casanova, and Eiji Saitoh. Tunable sign change of spin hall magnetoresistance in Pt/NiO/YIG structures. *Phys. Rev. Lett.*, 118:147202, Apr 2017.

[27] Pin-Jui Hsu, André Kubetzka, Aurore Finco, Niklas Romming, Kirsten von Bergmann, and Roland Wiesendanger. Electric-field-driven switching of individual magnetic skyrmions. *Nature Nanotechnology*, 12(2):123–126, 2017.

[28] S. Y. Huang, X. Fan, D. Qu, Y. P. Chen, W. G. Wang, J. Wu, T. Y. Chen, J. Q. Xiao, and C. L. Chien. Transport magnetic proximity effects in platinum. *Phys. Rev. Lett.*, 109:107204, Sep 2012.

[29] S. Y. Huang, W. G. Wang, S. F. Lee, J. Kwo, and C. L. Chien. Intrinsic spin-dependent thermal transport. *Phys. Rev. Lett.*, 107:216604, Nov 2011.

[30] Shuichi Iida. Magnetostriction constants of rare earth iron garnets. *Journal of the Physical Society of Japan*, 22(5):1201–1209, 1967.

[31] Shuichi Iida. Magnetostriction constants of rare earth iron garnets. *Journal of the Physical Society of Japan*, 22(5):1201–1209, 1967.

[32] C. M. Jaworski, J. Yang, S. Mack, D. D. Awschalom, J. P. Heremans, and R. C. Myers. Observation of the spin-seebeck effect in a ferromagnetic semiconductor. *Nature Materials*, 9(11):898–903, 2010.

[33] F. J. Jedema, A. T. Filip, and B. J. van Wees. Electrical spin injection and accumulation at room temperature in an all-metal mesoscopic spin valve. *Nature*, 410(6826):345–348, 2001.

[34] Xingtao Jia, Kai Liu, Ke Xia, and Gerrit E. W. Bauer. Spin transfer torque on magnetic insulators. *EPL (Europhysics Letters)*, 96(1):17005, sep 2011.

[35] Wanjun Jiang, Pramey Upadhyaya, Wei Zhang, Guoqiang Yu, M. Benjamin Jungfleisch, Frank Y. Fradin, John E. Pearson, Yaroslav Tserkovnyak, Kang L. Wang, Olle Heinonen, Suzanne G. E. te Velthuis, and Axel Hoffmann. Blowing magnetic skyrmion bubbles. *Science*, 349(6245):283–286, 2015.

[36] Zilong Jiang, Cui-Zu Chang, Chi Tang, Peng Wei, Jagadeesh S. Moodera, and Jing Shi. Independent tuning of electronic properties and induced ferromagnetism in topological insulators with heterostructure approach. *Nano Letters*, 15(9):5835–5840, 2015.

[37] F. Jonietz, S. Mühlbauer, C. Pfleiderer, A. Neubauer, W. Münzer, A. Bauer, T. Adams, R. Georgii, P. Böni, R. A. Duine, K. Everschor, M. Garst, and A. Rosch. Spin transfer torques in mnsi at ultralow current densities. *Science*, 330(6011):1648–1651, 2010.

[38] Y. Kajiwara, K. Harii, S. Takahashi, J. Ohe, K. Uchida, M. Mizuguchi, H. Umezawa, H. Kawai, K. Ando, K. Takanashi, S. Maekawa, and E. Saitoh. Transmission of electrical signals by spin-wave interconversion in a magnetic insulator. *Nature*, 464(7286):262–266, 2010.

[39] C. L. Kane and E. J. Mele. Quantum spin hall effect in graphene. *Physical Review Letters*, 95(22), 2005.

[40] Ferhat Katmis, Valeria Lauter, Flavio S. Nogueira, Badih A. Assaf, Michelle E. Jamer, Peng Wei, Biswarup Satpati, John W. Freeland, Ilya Eremin, Don Heiman, and et al. A high-temperature ferromagnetic topological insulating phase by proximity coupling. *Nature*, 533(7604):513–516, 2016.

[41] Y. K. Kato, R. C. Myers, A. C. Gossard, and D. D. Awschalom. Observation of the spin hall effect in semiconductors. *Science*, 306(5703):1910–1913, 2004.

[42] F. Keffer and C. Kittel. Theory of antiferromagnetic resonance. *Phys. Rev.*, 85:329–337, Jan 1952.

[43] T. Kikkawa, K. Uchida, Y. Shiomi, Z. Qiu, D. Hou, D. Tian, H. Nakayama, X.-F. Jin, and E. Saitoh. Longitudinal spin seebeck effect free from the proximity nernst effect. *Phys. Rev. Lett.*, 110:067207, Feb 2013.

[44] Se Kwon Kim, Yaroslav Tserkovnyak, and Oleg Tchernyshyov. Propulsion of a domain wall in an antiferromagnet by magnons. *Phys. Rev. B*, 90:104406, Sep 2014.

[45] C. Kittel. Theory of antiferromagnetic resonance. *Phys. Rev.*, 82:565–565, May 1951.

[46] Lingyao Kong and Jiadong Zang. Dynamics of an insulating skyrmion under a temperature gradient. *Phys. Rev. Lett.*, 111:067203, Aug 2013.

[47] G. Kresse and J. Furthmüller. Efficient iterative schemes for ab initio total-energy calculations using a plane-wave basis set. *Phys. Rev. B*, 54:11169–11186, Oct 1996.

[48] G. Kresse and J. Furthmüller. Efficiency of ab-initio total energy calculations for metals and semiconductors using a plane-wave basis set. *Computational Materials Science*, 6(1):15 – 50, 1996.

[49] G. Kresse and D. Joubert. From ultrasoft pseudopotentials to the projector augmented-wave method. *Phys. Rev. B*, 59:1758–1775, Jan 1999.

[50] D. Kriegner, K. Výborný, K. Olejník, H. Reichlová, V. Novák, X. Marti, J. Gazquez, V. Saidl, P. Nemec, V. V. Volobuev, G. Springholz, V. Holý, and T. Jungwirth. Multiple-stable anisotropic magnetoresistance memory in antiferromagnetic mnte. *Nature Communications*, 7(1):11623, 2016.

[51] Junxue Li, Zhong Shi, Victor H. Ortiz, Mohammed Aldosary, Cliff Chen, Vivek Aji, Peng Wei, and Jing Shi. Spin seebeck effect from antiferromagnetic magnons and critical spin fluctuations in epitaxial fef_2 films. *Phys. Rev. Lett.*, 122:217204, May 2019.

[52] Junxue Li, Yadong Xu, Mohammed Aldosary, Chi Tang, Zhisheng Lin, Shufeng Zhang, Roger Lake, and Jing Shi. Observation of magnon-mediated current drag in pt/yttrium iron garnet/pt(ta) trilayers. *Nature Communications*, 7(1):10858, 2016.

[53] Xiao Liang, Yupeng Zhu, Bo Peng, Longjiang Deng, Jianliang Xie, Haipeng Lu, Mingzhong Wu, and Lei Bi. Influence of interface structure on magnetic proximity effect in pt/y3fe5o12 heterostructures. *ACS Applied Materials & Interfaces*, 8(12):8175–8183, Mar 2016.

[54] Tao Lin, Chi Tang, Hamad M. Alyahayaei, and Jing Shi. Experimental investigation of the nature of the magnetoresistance effects in pd-yig hybrid structures. *Phys. Rev. Lett.*, 113:037203, Jul 2014.

[55] Tao Lin, Chi Tang, and Jing Shi. Induced magneto-transport properties at palladium/yttrium iron garnet interface. *Applied Physics Letters*, 103(13):132407, 2013.

[56] Weiwei Lin, Kai Chen, Shufeng Zhang, and C. L. Chien. Enhancement of thermally injected spin current through an antiferromagnetic insulator. *Phys. Rev. Lett.*, 116:186601, May 2016.

[57] Weiwei Lin and C. L. Chien. Electrical detection of spin backflow from an antiferromagnetic insulator/$y_3fe_5o_{12}$ interface. *Phys. Rev. Lett.*, 118:067202, Feb 2017.

[58] Chao-Xing Liu, Shou-Cheng Zhang, and Xiao-Liang Qi. The quantum anomalous hall effect: Theory and experiment. *Annual Review of Condensed Matter Physics*, 7(1):301–321, Oct 2016.

[59] Luqiao Liu, Takahiro Moriyama, D. C. Ralph, and R. A. Buhrman. Spin-torque ferromagnetic resonance induced by the spin hall effect. *Phys. Rev. Lett.*, 106:036601, Jan 2011.

[60] Luqiao Liu, Chi-Feng Pai, Y. Li, H. W. Tseng, D. C. Ralph, and R. A. Buhrman. Spin-torque switching with the giant spin hall effect of tantalum. *Science*, 336(6081):555–558, 2012.

[61] Y. M. Lu, Y. Choi, C. M. Ortega, X. M. Cheng, J. W. Cai, S. Y. Huang, L. Sun, and C. L. Chien. Pt magnetic polarization on $\mathbf{y}_3fe_5\mathbf{o}_{12}$ and magnetotransport characteristics. *Phys. Rev. Lett.*, 110:147207, Apr 2013.

[62] Davide Maccariello, William Legrand, Nicolas Reyren, Karin Garcia, Karim Bouzehouane, Sophie Collin, Vincent Cros, and Albert Fert. Electrical detection of single magnetic skyrmions in metallic multilayers at room temperature. *Nature Nanotechnology*, 13(3):233–237, 2018.

[63] A. P. Malozemoff and Slonczewski; J. C. *Magnetic domain walls in bubble materials*. Academic Press, 1979.

[64] X. Marti, I. Fina, C. Frontera, Jian Liu, P. Wadley, Q. He, R. J. Paull, J. D. Clarkson, J. Kudrnovský, I. Turek, J. Kunes, D. Yi, J.-H. Chu, C. T. Nelson, L. You, E. Arenholz, S. Salahuddin, J. Fontcuberta, T. Jungwirth, and R. Ramesh. Room-temperature antiferromagnetic memory resistor. *Nature Materials*, 13(4):367–374, 2014.

[65] Jobu Matsuno, Naoki Ogawa, Kenji Yasuda, Fumitaka Kagawa, Wataru Koshibae, Naoto Nagaosa, Yoshinori Tokura, and Masashi Kawasaki. Interface-driven topological hall effect in srruo3-sriro3 bilayer. *Science Advances*, 2(7), 2016.

[66] W. H. Meiklejohn and C. P. Bean. New magnetic anisotropy. *Phys. Rev.*, 105:904–913, Feb 1957.

[67] Sibylle Meyer, Richard Schlitz, Stephan Geprägs, Matthias Opel, Hans Huebl, Rudolf Gross, and Sebastian T. B. Goennenwein. Anomalous hall effect in yig—pt bilayers. *Applied Physics Letters*, 106(13):132402, 2015.

[68] B. F. Miao, S. Y. Huang, D. Qu, and C. L. Chien. Physical origins of the new magnetoresistance in Pt/YIG. *Phys. Rev. Lett.*, 112:236601, Jun 2014.

[69] Ioan Mihai Miron, Kevin Garello, Gilles Gaudin, Pierre-Jean Zermatten, Marius V. Costache, Stéphane Auffret, Sébastien Bandiera, Bernard Rodmacq, Alain Schuhl, Pietro Gambardella, and et al. Perpendicular switching of a single ferromagnetic layer induced by in-plane current injection. *Nature*, 476(7359):189–193, 2011.

[70] Ioan Mihai Miron, Thomas Moore, Helga Szambolics, Liliana Daniela Buda-Prejbeanu, Stéphane Auffret, Bernard Rodmacq, Stefania Pizzini, Jan Vogel, Marlio Bonfim, Alain Schuhl, and et al. Fast current-induced domain-wall motion controlled by the rashba effect. *Nature Materials*, 10(6):419–423, 2011.

[71] Shigemi Mizukami, Yasuo Ando, and Terunobu Miyazaki. The study on ferromagnetic resonance linewidth for NM/80nife/NM (NM=cu, ta, pd and pt) films. *Japanese Journal of Applied Physics*, 40(Part 1, No. 2A):580–585, feb 2001.

[72] M. Mochizuki, X. Z. Yu, S. Seki, N. Kanazawa, W. Koshibae, J. Zang, M. Mostovoy, Y. Tokura, and N. Nagaosa. Thermally driven ratchet motion of a skyrmion microcrystal and topological magnon hall effect. *Nature Materials*, 13(3):241–246, 2014.

[73] Masataka Mogi, Taro Nakajima, Victor Ukleev, Atsushi Tsukazaki, Ryutaro Yoshimi, Minoru Kawamura, Kei S. Takahashi, Takayasu Hanashima, Kazuhisa Kakurai, Taka-Hisa Arima, and et al. Large anomalous hall effect in topological insulators with proximitized ferromagnetic insulators. *Physical Review Letters*, 123(1), Feb 2019.

[74] C. Moreau-Luchaire, C. Moutafis, N. Reyren, J. Sampaio, C. A. F. Vaz, N. Van Horne, K. Bouzehouane, K. Garcia, C. Deranlot, P. Warnicke, P. Wohlhüter, J.-M. George,

M. Weigand, J. Raabe, V. Cros, and A. Fert. Additive interfacial chiral interaction in multilayers for stabilization of small individual skyrmions at room temperature. *Nature Nanotechnology*, 11(5):444–448, 2016.

[75] S. Mühlbauer, B. Binz, F. Jonietz, C. Pfleiderer, A. Rosch, A. Neubauer, R. Georgii, and P. Böni. Skyrmion lattice in a chiral magnet. *Science*, 323(5916):915–919, 2009.

[76] Naoto Nagaosa, Jairo Sinova, Shigeki Onoda, A. H. MacDonald, and N. P. Ong. Anomalous hall effect. *Rev. Mod. Phys.*, 82:1539–1592, May 2010.

[77] Ryan Nakamoto, Bin Xu, Changsong Xu, Hu Xu, and L. Bellaiche. Properties of rare-earth iron garnets from first principles. *Phys. Rev. B*, 95:024434, Jan 2017.

[78] Kouki Nakata, Jelena Klinovaja, and Daniel Loss. Magnonic quantum hall effect and wiedemann-franz law. *Phys. Rev. B*, 95:125429, Mar 2017.

[79] H. Nakayama, M. Althammer, Y.-T. Chen, K. Uchida, Y. Kajiwara, D. Kikuchi, T. Ohtani, S. Geprägs, M. Opel, S. Takahashi, R. Gross, G. E. W. Bauer, S. T. B. Goennenwein, and E. Saitoh. Spin hall magnetoresistance induced by a nonequilibrium proximity effect. *Phys. Rev. Lett.*, 110:206601, May 2013.

[80] A. Neubauer, C. Pfleiderer, B. Binz, A. Rosch, R. Ritz, P. G. Niklowitz, and P. Böni. Topological hall effect in the *a* phase of mnsi. *Phys. Rev. Lett.*, 102:186602, May 2009.

[81] Junichi Nishitani, Kohei Kozuki, Takeshi Nagashima, and Masanori Hangyo. Terahertz radiation from coherent antiferromagnetic magnons excited by femtosecond laser pulses. *Applied Physics Letters*, 96(22):221906, 2010.

[82] J Nogués and Ivan K Schuller. Exchange bias. *Journal of Magnetism and Magnetic Materials*, 192(2):203 – 232, 1999.

[83] Héctor Ochoa, Se Kwon Kim, and Yaroslav Tserkovnyak. Topological spin-transfer drag driven by skyrmion diffusion. *Phys. Rev. B*, 94:024431, Jul 2016.

[84] K. Olejník, V. Schuler, X. Marti, V. Novák, Z. Kaspar, P. Wadley, R. P. Campion, K. W. Edmonds, B. L. Gallagher, J. Garces, M. Baumgartner, P. Gambardella, and T. Jungwirth. Antiferromagnetic cumnas multi-level memory cell with microelectronic compatibility. *Nature Communications*, 8(1):15434, 2017.

[85] Y. Onose, Y. Okamura, S. Seki, S. Ishiwata, and Y. Tokura. Observation of magnetic excitations of skyrmion crystal in a helimagnetic insulator cu_2oseo_3. *Phys. Rev. Lett.*, 109:037603, Jul 2012.

[86] Victor H. Ortiz, Mohammed Aldosary, Junxue Li, Yadong Xu, Mark I. Lohmann, Pathikumar Sellappan, Yasuhiro Kodera, Javier E. Garay, and Jing Shi. Systematic control of strain-induced perpendicular magnetic anisotropy in epitaxial europium and terbium iron garnet thin films. *APL Materials*, 6(12):121113, 2018.

[87] Chi-Feng Pai, Maxwell Mann, Aik Jun Tan, and Geoffrey S. D. Beach. Determination of spin torque efficiencies in heterostructures with perpendicular magnetic anisotropy. *Phys. Rev. B*, 93:144409, Apr 2016.

[88] John P. Perdew, Kieron Burke, and Matthias Ernzerhof. Generalized gradient approximation made simple. *Phys. Rev. Lett.*, 77:3865–3868, Oct 1996.

[89] S. Pöllath, J. Wild, L. Heinen, T. N. G. Meier, M. Kronseder, L. Tutsch, A. Bauer, H. Berger, C. Pfleiderer, J. Zweck, A. Rosch, and C. H. Back. Dynamical defects in rotating magnetic skyrmion lattices. *Phys. Rev. Lett.*, 118:207205, May 2017.

[90] Xiao-Liang Qi, Taylor L. Hughes, and Shou-Cheng Zhang. Topological field theory of time-reversal invariant insulators. *Physical Review B*, 78(19), 2008.

[91] Zhenhua Qiao, Wei Ren, Hua Chen, L. Bellaiche, Zhenyu Zhang, A. H. Macdonald, and Qian Niu. Quantum anomalous hall effect in graphene proximity coupled to an antiferromagnetic insulator. *Physical Review Letters*, 112(11), 2014.

[92] Zhenhua Qiao, Shengyuan A. Yang, Wanxiang Feng, Wang-Kong Tse, Jun Ding, Yugui Yao, Jian Wang, and Qian Niu. Quantum anomalous hall effect in graphene from rashba and exchange effects. *Physical Review B*, 82(16), 2010.

[93] Zhiyong Qiu, Dazhi Hou, Joseph Barker, Kei Yamamoto, Olena Gomonay, and Eiji Saitoh. Spin colossal magnetoresistance in an antiferromagnetic insulator. *Nature Materials*, 17(7):577–580, 2018.

[94] D. Qu, S. Y. Huang, Jun Hu, Ruqian Wu, and C. L. Chien. Intrinsic spin seebeck effect in Au/YIG. *Phys. Rev. Lett.*, 110:067206, Feb 2013.

[95] M. Raju, A. Yagil, Anjan Soumyanarayanan, Anthony K. C. Tan, A. Almoalem, Fusheng Ma, O. M. Auslaender, and C. Panagopoulos. The evolution of skyrmions in ir/fe/co/pt multilayers and their topological hall signature. *Nature Communications*, 10(1):696, 2019.

[96] Yafei Ren, Zhenhua Qiao, and Qian Niu. Topological phases in two-dimensional materials: a review. *Reports on Progress in Physics*, 79(6):066501, 2016.

[97] S. M. Rezende, R. L. Rodríguez-Suárez, and A. Azevedo. Theory of the spin seebeck effect in antiferromagnets. *Phys. Rev. B*, 93:014425, Jan 2016.

[98] Sergio M Rezende, Antonio Azevedo, and Roberto L Rodríguez-Suárez. Magnon diffusion theory for the spin seebeck effect in ferromagnetic and antiferromagnetic insulators. *Journal of Physics D: Applied Physics*, 51(17):174004, apr 2018.

[99] Niklas Romming, Christian Hanneken, Matthias Menzel, Jessica E. Bickel, Boris Wolter, Kirsten von Bergmann, André Kubetzka, and Roland Wiesendanger. Writing and deleting single magnetic skyrmions. *Science*, 341(6146):636–639, 2013.

[100] U. K. Rößler, A. N. Bogdanov, and C. Pfleiderer. Spontaneous skyrmion ground states in magnetic metals. *Nature*, 442(7104):797–801, 2006.

[101] Kwang-Su Ryu, Luc Thomas, See-Hun Yang, and Stuart Parkin. Chiral spin torque at magnetic domain walls. *Nature Nanotechnology*, 8:527 EP –, Jun 2013. Article.

[102] E. Saitoh, M. Ueda, H. Miyajima, and G. Tatara. Conversion of spin current into charge current at room temperature: Inverse spin-hall effect. *Applied Physics Letters*, 88(18):182509, 2006.

[103] Christoph Schütte and Markus Garst. Magnon-skyrmion scattering in chiral magnets. *Phys. Rev. B*, 90:094423, Sep 2014.

[104] S. Seki, T. Ideue, M. Kubota, Y. Kozuka, R. Takagi, M. Nakamura, Y. Kaneko, M. Kawasaki, and Y. Tokura. Thermal generation of spin current in an antiferromagnet. *Phys. Rev. Lett.*, 115:266601, Dec 2015.

[105] S. Seki, X. Z. Yu, S. Ishiwata, and Y. Tokura. Observation of skyrmions in a multiferroic material. *Science*, 336(6078):198–201, 2012.

[106] Pathikumar Sellappan, Chi Tang, Jing Shi, and Javier E. Garay. An integrated approach to doped thin films with strain-tunable magnetic anisotropy: powder synthesis, target preparation and pulsed laser deposition of bi:yig. *Materials Research Letters*, 5(1):41–47, 2017.

[107] Qiming Shao, Alexander Grutter, Yawen Liu, Guoqiang Yu, Chao-Yao Yang, Dustin A. Gilbert, Elke Arenholz, Padraic Shafer, Xiaoyu Che, Chi Tang, Mohammed Aldosary, Aryan Navabi, Qing Lin He, Brian J. Kirby, Jing Shi, and Kang L. Wang. Exploring interfacial exchange coupling and sublattice effect in heavy metal/ferrimagnetic insulator heterostructures using hall measurements, x-ray magnetic circular dichroism, and neutron reflectometry. *Phys. Rev. B*, 99:104401, Mar 2019.

[108] Qiming Shao, Yawen Liu, Guoqiang Yu, Se Kwon Kim, Xiaoyu Che, Chi Tang, Qing Lin He, Yaroslav Tserkovnyak, Jing Shi, and Kang L. Wang. Topological hall effect at above room temperature in heterostructures composed of a magnetic insulator and a heavy metal. *Nature Electronics*, 2(5):182–186, 2019.

[109] Qiming Shao, Chi Tang, Guoqiang Yu, Aryan Navabi, Hao Wu, Congli He, Junxue Li, Pramey Upadhyaya, Peng Zhang, Seyed Armin Razavi, and et al. Role of dimensional crossover on spin-orbit torque efficiency in magnetic insulator thin films. *Nature Communications*, 9(1), June 2018.

[110] Qiming Shao, Chi Tang, Guoqiang Yu, Aryan Navabi, Hao Wu, Congli He, Junxue Li, Pramey Upadhyaya, Peng Zhang, Seyed Armin Razavi, Qing Lin He, Yawen Liu, Pei Yang, Se Kwon Kim, Cheng Zheng, Yizhou Liu, Lei Pan, Roger K. Lake, Xiufeng Han, Yaroslav Tserkovnyak, Jing Shi, and Kang L. Wang. Role of dimensional crossover on spin-orbit torque efficiency in magnetic insulator thin films. *Nature Communications*, 9(1):3612, 2018.

[111] Jairo Sinova, Sergio O. Valenzuela, J. Wunderlich, C. H. Back, and T. Jungwirth. Spin hall effects. *Rev. Mod. Phys.*, 87:1213–1260, Oct 2015.

[112] A. Sola, P. Bougiatioti, M. Kuepferling, D. Meier, G. Reiss, M. Pasquale, T. Kuschel, and V. Basso. Longitudinal spin seebeck coefficient: heat flux vs. temperature difference method. *Scientific Reports*, 7(1):46752, 2017.

[113] S. L. Sondhi, A. Karlhede, S. A. Kivelson, and E. H. Rezayi. Skyrmions and the crossover from the integer to fractional quantum hall effect at small zeeman energies. *Phys. Rev. B*, 47:16419–16426, Jun 1993.

[114] Chikazumi Soshin. *Physics of ferromagnetism*. Oxford Univ. Press, 2010.

[115] Anjan Soumyanarayanan, M. Raju, A. L. Gonzalez Oyarce, Anthony K. C. Tan, Mi-Young Im, A. ?. P. Petrovic, Pin Ho, K. H. Khoo, M. Tran, C. K. Gan, F. Ernult, and C. Panagopoulos. Tunable room-temperature magnetic skyrmions in ir/fe/co/pt multilayers. *Nature Materials*, 16(9):898–904, 2017.

[116] T. Suzuki, R. Chisnell, A. Devarakonda, Y.-T. Liu, W. Feng, D. Xiao, J. ?. W. Lynn, and J. ?. G. Checkelsky. Large anomalous hall effect in a half-heusler antiferromagnet. *Nature Physics*, 12(12):1119–1123, 2016.

[117] Kei S. Takahashi, Hiroaki Ishizuka, Tomoki Murata, Qing Y. Wang, Yoshinori Tokura, Naoto Nagaosa, and Masashi Kawasaki. Anomalous hall effect derived from multiple weyl nodes in high-mobility eutio3 films. *Science Advances*, 4(7), 2018.

[118] Chi Tang. PhD thesis, UC Riverside, 2017.

[119] Chi Tang, Mohammed Aldosary, Zilong Jiang, Houchen Chang, Benjamin Madon, Kyle Chan, Mingzhong Wu, Javier E. Garay, and Jing Shi. Exquisite growth control and magnetic properties of yttrium iron garnet thin films. *Applied Physics Letters*, 108(10):102403, Jul 2016.

[120] Chi Tang, Cui-Zu Chang, Gejian Zhao, Yawen Liu, Zilong Jiang, Chao-Xing Liu, Martha R. Mccartney, David J. Smith, Tingyong Chen, Jagadeesh S. Moodera, and et al. Above 400-k robust perpendicular ferromagnetic phase in a topological insulator. *Science Advances*, 3(6), 2017.

[121] Chi Tang, Pathikumar Sellappan, Yawen Liu, Yadong Xu, Javier E. Garay, and Jing Shi. Anomalous hall hysteresis intm3fe5o12/ptwith strain-induced perpendicular magnetic anisotropy. *Physical Review B*, 94(14), July 2016.

[122] K. Uchida, S. Takahashi, K. Harii, J. Ieda, W. Koshibae, K. Ando, S. Maekawa, and E. Saitoh. Observation of the spin seebeck effect. *Nature*, 455(7214):778–781, 2008.

[123] K. Uchida, J. Xiao, H. Adachi, J. Ohe, S. Takahashi, J. Ieda, T. Ota, Y. Kajiwara, H. Umezawa, H. Kawai, G. E. W. Bauer, S. Maekawa, and E. Saitoh. Spin seebeck insulator. *Nature Materials*, 9(11):894–897, 2010.

[124] Ken-ichi Uchida, Hiroto Adachi, Takeru Ota, Hiroyasu Nakayama, Sadamichi Maekawa, and Eiji Saitoh. Observation of longitudinal spin-seebeck effect in magnetic insulators. *Applied Physics Letters*, 97(17):172505, 2010.

[125] Pramey Upadhyaya, Guoqiang Yu, Pedram Khalili Amiri, and Kang L. Wang. Electric-field guiding of magnetic skyrmions. *Phys. Rev. B*, 92:134411, Oct 2015.

[126] S. O. Valenzuela and M. Tinkham. Direct electronic measurement of the spin hall effect. *Nature*, 442(7099):176–179, 2006.

[127] Hailong Wang, Chunhui Du, P. Chris Hammel, and Fengyuan Yang. Antiferromagnonic spin transport from $y_3fe_5o_{12}$ into nio. *Phys. Rev. Lett.*, 113:097202, Aug 2014.

[128] Zhiyong Wang, Chi Tang, Raymond Sachs, Yafis Barlas, and Jing Shi. Proximity-induced ferromagnetism in graphene revealed by the anomalous hall effect. *Physical Review Letters*, 114(1), July 2015.

[129] R. Watanabe, R. Yoshimi, M. Kawamura, M. Mogi, A. Tsukazaki, X. Z. Yu, K. Nakajima, K. S. Takahashi, M. Kawasaki, Y. Tokura, and et al. Quantum anomalous hall effect driven by magnetic proximity coupling in all-telluride based heterostructure. *Applied Physics Letters*, 115(10):102403, Feb 2019.

[130] Hongming Weng, Rui Yu, Xiao Hu, Xi Dai, and Zhong Fang. Quantum anomalous hall effect and related topological electronic states. *Advances in Physics*, 64(3):227–282, Apr 2015.

[131] Seonghoon Woo, Kai Litzius, Benjamin Krüger, Mi-Young Im, Lucas Caretta, Kornel Richter, Maxwell Mann, Andrea Krone, Robert M. Reeve, Markus Weigand, Parnika Agrawal, Ivan Lemesh, Mohamad-Assaad Mawass, Peter Fischer, Mathias Kläui, and Geoffrey S. D. Beach. Observation of room-temperature magnetic skyrmions and their current-driven dynamics in ultrathin metallic ferromagnets. *Nature Materials*, 15(5):501–506, 2016.

[132] Stephen M. Wu, Wei Zhang, Amit KC, Pavel Borisov, John E. Pearson, J. Samuel Jiang, David Lederman, Axel Hoffmann, and Anand Bhattacharya. Antiferromagnetic spin seebeck effect. *Phys. Rev. Lett.*, 116:097204, Mar 2016.

[133] Bowen Yang, Mark Lohmann, David Barroso, Ingrid Liao, Zhisheng Lin, Yawen Liu, Ludwig Bartels, Kenji Watanabe, Takashi Taniguchi, Jing Shi, and et al. Strong electron-hole symmetric rashba spin-orbit coupling in graphene/monolayer transition metal dichalcogenide heterostructures. *Physical Review B*, 96(4), 2017.

[134] Bowen Yang, Everardo Molina, Jeongwoo Kim, David Barroso, Mark Lohmann, Yawen Liu, Yadong Xu, Ruqian Wu, Ludwig Bartels, Kenji Watanabe, and et al. Effect of distance on photoluminescence quenching and proximity-induced spin–orbit coupling in graphene/wse2 heterostructures. *Nano Letters*, 18(6):3580–3585, 2018.

[135] Bowen Yang, Min-Feng Tu, Jeongwoo Kim, Yong Wu, Hui Wang, Jason Alicea, Ruqian Wu, Marc Bockrath, and Jing Shi. Tunable spin–orbit coupling and symmetry-protected edge states in graphene/ws2. *2D Materials*, 3(3):031012, Dec 2016.

[136] Yugui Yao, Leonard Kleinman, A. H. MacDonald, Jairo Sinova, T. Jungwirth, Dingsheng Wang, Enge Wang, and Qian Niu. First principles calculation of anomalous hall conductivity in ferromagnetic bcc fe. *Phys. Rev. Lett.*, 92:037204, Jan 2004.

[137] K. Yasuda, R. Wakatsuki, T. Morimoto, R. Yoshimi, A. Tsukazaki, K. S. Takahashi, M. Ezawa, M. Kawasaki, N. Nagaosa, and Y. Tokura. Geometric hall effects in topological insulator?heterostructures. *Nature Physics*, 12(6):555–559, 2016.

[138] Guoqiang Yu, Pramey Upadhyaya, Qiming Shao, Hao Wu, Gen Yin, Xiang Li, Congli He, Wanjun Jiang, Xiufeng Han, Pedram Khalili Amiri, and Kang L. Wang. Room-temperature skyrmion shift device for memory application. *Nano Letters*, 17(1):261–268, Jan 2017.

[139] R. Yu, W. Zhang, H.-J. Zhang, S.-C. Zhang, X. Dai, and Z. Fang. Quantized anomalous hall effect in magnetic topological insulators. *Science*, 329(5987):61–64, Mar 2010.

[140] Jiadong Zang, Maxim Mostovoy, Jung Hoon Han, and Naoto Nagaosa. Dynamics of skyrmion crystals in metallic thin films. *Phys. Rev. Lett.*, 107:136804, Sep 2011.

[141] Shufeng Zhang. Spin hall effect in the presence of spin diffusion. *Phys. Rev. Lett.*, 85:393–396, Jul 2000.

[142] X. Zhou, L. Ma, Z. Shi, G. Y. Guo, J. Hu, R. Q. Wu, and S. M. Zhou. Tuning magnetotransport in pdpt/y3fe5o12: Effects of magnetic proximity and spin-orbit coupling. *Applied Physics Letters*, 105(1):012408, July 2014.

[143] Igor Žutić, Jaroslav Fabian, and S. Das Sarma. Spintronics: Fundamentals and applications. *Reviews of Modern Physics*, 76(2):323–410, 2004.